Surface Forces and Structure in Model Cytosol Solutions

A thesis submitted for the degree of

Doctor of Philosophy

Kieran James Agg

The Queen's College

Department of Chemistry

University of Oxford

Trinity Term 2025

Declaration

This thesis is submitted for the degree of Doctor of Philosophy in Physical and Theoretical Chemistry at the University of Oxford. No part of this thesis has been accepted or is currently being submitted for any degree, diploma, certificate or other qualification in this University or elsewhere. This thesis is my own work, except where indicated.

Some of the measurements presented in Chapter 4 were performed in collaboration with Dr James Hallett. The neutron and X-ray scattering results presented in Chapter 5 are based on measurements performed collaboratively with an experimental team at the ISIS Neutron and Muon Source.

Abstract

In the cellular environment, the cytosol - the aqueous fluid in which organelles are suspended - is of rich chemical diversity and fundamental importance in mediating biochemical processes. The composition of this liquid is carefully regulated to maintain order and function of macromolecular structures in addition to balancing external osmotic pressure. Yet, much is still unknown about the role that individual osmolytic components play in mediating cellular interactions. This thesis presents an investigation of the molecular interactions and structures within model cytosol solutions, aqueous solutions containing various osmolytic solutes found throughout nature, in order to determine how these ions and molecules can modulate interactions and contribute, or detract, from biochemical stability in the cellular environment.

The work begins by presenting measurements of surface forces across two simple electrolytes - ultrapure water and a dilute potassium chloride electrolyte - providing a benchmark to which to compare solutions of increasing complexity. These reference measurements allow for the introduction of the framework through which these and similar measurements can be interpreted by analysing the various contributions to the overall interaction. These include the far-field electric double layer repulsion and van der Waals surface interactions, in addition to short-range structural features. In the subsequent chapter, the role played by zwitterionic osmolytes in modulating the interactions in solutions is investigated, and we find a key role for these molecules in maintaining repulsive interactions across a wide concentration range, as well as tuning the interfacial structures in mixed zwitterion-salt aqueous solutions. This is followed by an investigation of the bulk solution structures in zwitterion-salt solutions using a combined neutron and X-ray total scattering approach, revealing molecular-level details pertaining to zwitterion-ion interactions and clustering, including the dependence on the ion identity. We continue with a study of surface forces across a pairing of a protein stabilising and destabilising osmolyte, in order

to investigate the colloidal contribution to the resulting stability. We find that the protein stabiliser, trimethylamine *N*-oxide, acts to disrupt hydration forces, unlike the destabiliser, urea, which does not. A solution containing a mixture of both osmolytes is shown to exhibit a compromise between the two individual cases. Finally, the thesis concludes with an investigation of surface forces across solutions containing glycine oligopeptides, a model for the protein backbone, where clear oligomer size effects are observed for surface adsorption and self-assembly.

Combined, the results presented in this thesis illustrate the complex behaviours exhibited by a range of osmolytic solutes in solution and their ability to modulate interactions between charged surfaces and solution structures. This work contributes to our understanding of the toolbox available in natural systems to maintain cellular functionality by altering the composition of the cytosolic fluid in response to various environmental stresses.

Acknowledgements

First of all, I wish to thank my supervisor Professor Susan Perkin for her support and guidance throughout this project. Her infectious curiosity and deep insight have been a constant source of motivation, and the scientific freedom she gave me has greatly contributed to my development as a scientist.

Next, I would like to express my gratitude to Dr Tim Groves, Dr Catherine Fung and Dr Shurui Miao for their wonderful support and friendship. Each has been an excellent mentor and the present form of this thesis owes much to them. I must also thank Dr James Hallett who helped inform many of the directions taken in this research. I have greatly appreciated our continued collaboration, particularly on the neutron scattering that formed an important chapter in this thesis. The success of this scattering project was also shaped hugely by the following scientists at the ISIS Neutron and Muon Source: Dr Oliver Alderman, Dr Thomas Headen, Dr Terri-Louise Hughes and Dr Tristan Youngs.

I would also like to thank all the past and current members of the Perkin Group who I have had the pleasure of interacting with over the years: Hannah, Astrid, Aurora, Josh, Ilaria, Rachel, Josie, Sofia, Amaar, Alex, Daria, Neave, Lauriane, Izzy, Tina, Toby and Ilan. Thank you also to the wider PTCL community, especially those I have shared many entertaining and stimulating lunch breaks with. The work of the PTCL mechanical and electronics workshops and the building management team must also be recognised, upon which much of the experimental science performed in this thesis has crucially relied.

Beyond the department, I have had the pleasure of meeting many inspiring individuals during these years in Oxford. A particular thanks must go to all those I have met through the Oxford University Triathlon Club, which has played a vital role in making my time here so enjoyable.

I am grateful to the Clarendon Fund and The Queen's College for the award of The Oxford-The Queen's College Graduate Scholarship which has enabled me to study for this DPhil. Additionally, the research in this thesis was supported by funding from the European Research Council and the Science and Technology Facilities Council.

Finally, I must thank my family for the boundless support and encouragement they have provided over the years, and to Anna for sharing life's adventures with me.

Publications

The following published journal articles are based on work presented in this thesis:

1. J. E. Hallett, K. J. Agg and S. Perkin; Zwitterions fine-tune interactions in electrolyte solutions; *Proceedings of the National Academy of Sciences of the United States of America*, 120 (8), 2023, e2215585120 (Chapters 3 and 4)[1]

2. K. J. Agg, J. E. Hallett and S. Perkin; The influence of proline on surface interactions in aqueous solutions; *Biophysical Journal*, 2025 (Chapters 3 and 4)[2]

3. K. J. Agg, T. S. Groves, S. Miao, Y. K. C. Fung, O. L. G. Alderman, T. F. Headen, T. L. Hughes, G. N. Smith, T. G. A. Youngs, J. P. Tellam, Y. Chen, S. Perkin and J. E. Hallett; Specific ion effects enhance local structure in zwitterionic osmolyte solutions; *Chemical Science*, 16 (16), 2025, 6770-6779 (Chapter 5)[3]

Contents

Declaration ii

Abstract iii

Acknowledgements v

Publications vii

Table of Contents viii

1 Introduction 1

1.1 The Cellular Environment, Osmolytes and Biomolecular Stability . . 1

1.2 The Liquid State and Liquids at Interfaces 6

1.2.1 Intermolecular Forces 6

1.2.2 Liquids at Interfaces 9

1.3 Experimental Measurements of Surface Interactions 14

1.4 Experimental Measurements of Bulk Structure 16

1.5 Overview 17

2 Experimental Methods 19

2.1 Surface Forces Measurements 19

2.1.1 Mica and Lens Preparation 19

2.1.2 Surface Force Balance Setup 21

2.1.3 Liquid Preparation 25

2.1.4 Optics and Image Analysis 26

2.1.5 Measuring Interaction Profiles 29

2.1.6 Experimental Error Analysis 35

2.2 Total Scattering Measurements 36

2.2.1 Diffraction Theory 37

2.2.2 Neutron Total Scattering 41
2.2.3 X-ray Total Scattering 45
2.2.4 Data Correction 46
2.2.5 Data Modelling 47
2.3 Additional Measurements 50
2.3.1 Refractive Index Measurements 51
2.3.2 Density Measurements 51

3 Surface Forces Measurements Across Simple Electrolytes 52
3.1 Background 52
3.2 DLVO Theory - Further Details 52
3.3 Experimental Details 58
3.3.1 Materials and Solution Preparation 58
3.3.2 Refractive Indices and Hamaker Constants 58
3.4 Pure Water 59
3.5 Dilute Potassium Chloride Electrolytes 60
3.6 Summary 64

4 The Role of Zwitterions in Model Cytosol Solutions 66
4.1 Background 66
4.1.1 Proline 67
4.1.2 Trimethylglycine 68
4.2 Experimental Details 69
4.2.1 Materials and Solution Preparation 69
4.2.2 Refractive Indices and Hamaker Constants 69
4.3 Surface Forces Measurements Across Proline Solutions 70
4.3.1 Proline-Only Solutions 70
4.3.2 Proline-KCl Mixtures 75
4.3.3 Influence of Solution Composition on Interfacial Structure . . 78
4.4 Surface Forces Measurements Across TMG Solutions 81

4.4.1 TMG-Only Solutions 81
4.4.2 TMG-KCl Mixtures 82
4.5 Proline and TMG Comparison 84
4.6 Summary 86

5 Bulk Structure and Ion Effects in Zwitterion Solutions 89
5.1 Background 89
5.2 Experimental and Simulation Details 90
5.2.1 Materials and Solution Preparation 90
5.2.2 Solution Densities 92
5.2.3 Simulation Details 92
5.3 Bulk Structure Measurements and Discussion 94
5.3.1 Bulk Water Structure 94
5.3.2 TMG Hydration Structure 100
5.3.3 Ion Hydration Structure 105
5.3.4 TMG-Ion Binding 108
5.3.5 Ion Total Coordination Environments 111
5.3.6 TMG-TMG Correlations and Ion-Mediated Clusters 112
5.4 Summary 118

6 Interactions Across Protein Stabilising and Destabilising Osmolyte Solutions 120
6.1 Background 120
6.2 Experimental Details 124
6.2.1 Materials and Solution Preparation 124
6.2.2 Refractive Indices and Hamaker Constants 124
6.3 Surface Forces Measurements Across TMAO or Urea Solutions 124
6.3.1 TMAO Solutions 125
6.3.2 Urea Solutions 127
6.3.3 Discussion 129

6.4 Surface Forces Measurements Across TMAO-Urea Mixtures 133
6.5 Summary 136

7 Glycine Oligopeptides at Charged Surfaces 138
7.1 Background 138
7.1.1 Interactions Between Glycine Oligomers 141
7.1.2 Surface Interactions Across Glycine Oligopeptide Solutions . . 142
7.2 Experimental Details 143
7.2.1 Materials and Solution Preparation 143
7.2.2 Refractive Indices and Hamaker Constants 143
7.3 Surface Forces Measurements and Discussion 145
7.3.1 Glycine Solutions 145
7.3.2 Diglycine Solutions 146
7.3.3 Triglycine Solutions 148
7.3.4 Oligoglycine Surface Structure 150
7.4 Summary 154

8 Conclusions and Outlook 156

Appendices 159

A The Role of Zwitterions in Model Cytosol Solutions - Supporting Data 160

B Bulk Structure and Ion Effects in Zwitterion Solutions - Supporting Data 163

C Interactions Across Protein Stabilising and Destabilising Osmolyte Solutions - Supporting Data 166

Bibliography 169

1 | Introduction

1.1 | The Cellular Environment, Osmolytes and Biomolecular Stability

Life on Earth can be found in all manner of environments. From ambient conditions to the extremities of the salinity of the Great Salt Lake, the pressures of the Mariana Trench and the temperatures of hydrothermal vents, there are living organisms to be found.[4] Through evolution, nature has developed a handle on biochemical processes across time and space within the cellular environment, enabling the barrier to survival to be overcome in these environments, and complex lifeforms have subsequently developed.

The cytosol is the aqueous substance in which organelles are suspended within the cell. This fluid is of rich chemical diversity and a fundamental component of the cellular environment. Whilst the study of biochemical evolution has concentrated on the role of large biological macromolecules such as proteins, DNA and RNA, as well as other cellular ensembles, the role of this fluid is often ignored. However, the specific makeup of the cytosol plays a vital role in facilitating various biochemical processes and cellular interactions, essential for the survival of life. Amongst other things, cytosolic composition is responsible for liquid-liquid phase separation within the cell, a process which has, in recent years, been found to be responsible for the compartmentalisation of biochemical species and increased efficiency of cellular processes.[5–7]

Across the living world, various selective pressures act to influence the makeup of the cellular fluid, and the interplay between the interior and exterior of a cell is vital for this. A strong selective pressure is that of environmental water stress, and the balancing of osmotic pressure - or the chemical potential of water - between the intra- and extracellular fluids. Such balance must be achieved by all organisms, else there may be an unsustainable influx or efflux of water across the cell

membrane, depending on the direction of the osmotic gradient, resulting in cell lysis or dehydration, and subsequently cell death. All unicellular environments are prone to experiencing fluctuating external osmotic pressures, and various strategies exist across the biosphere for managing these osmotic shocks. The strategies employed also vary in their sophistication depending on the complexity and evolutionary history of the organisms. For example, many single-celled organisms rely on the accumulation or loss of solutes in order to tune the internal osmotic pressure. In some cases it is possible for certain organisms to sustainably manage a hydrostatic, or turgor, pressure resulting from a difference between the internal and external osmotic pressures through the enhanced mechanical stiffness of the barrier separating the cell from the external environment. A notable case is that of the gram-positive bacteria, which have been found to manage turgor pressures of up to 7 bar through the presence of a cell wall in addition to the usual membrane.[8] In higher organisms, more sophisticated mechanisms of osmoprotection and osmoregulation have developed, such as the presence of skin to sustain osmotic imbalance and the ability to vary urine concentration. Nonetheless, tissues in such organisms exposed to locally high osmotic pressure, such as the renal medullary cells in the kidney, must still employ mechanisms to tune the cellular osmotic pressure.[9,10]

In most cases, the mechanism of osmoregulation within the cytosol involves the accumulation of osmolytes within the cellular environment, which can be defined as a solute that binds or interacts favourably with water, thus lowering the cellular water chemical potential.[8] Simplistically, osmolytes can be divided into ionic and nonionic osmolytes: ionic osmolytes include small inorganic ions (Na^+, K^+, Mg^{2+}, Ca^{2+}, Cl^-, $HCO_2{}^-$, $SO_4{}^{2-}$, $PO_4{}^{2-}$) as well as larger macromolecules with non-zero net charge, such the glutamate anion.[11] Nonionic osmolytes include zwitterions - net neutral molecules containing both a localised positive and negative charge - and other molecules with zero net charge.

Different classes of organisms favour the accumulation of the two types of os-

molytes to greater or lesser extents, employing strategies dependent on environmental, such as osmolyte bioavailability, and genetic factors. Halophilic microorganisms provide an excellent case study through which to explore these variations, where the osmoregulatory strategies have been tested to the extreme. These extremophiles have all evolved to survive and thrive in high salinity environments, such as the Great Salt Lake in Utah and the Dead Sea in West Asia where salt concentrations can reach $\sim$ 5 M,[12,13] yet divergent strategies to cope with the osmotic pressures have evolved in halophiles across the different domains of life.[14] For instance, extremely halophilic organisms, particularly archaea such as *Halobacterium cutirubrum* or *Methanosarcina barkeri*, maintain a high salt concentration within the cell itself.[15] In contrast, most halophilic bacteria such as *Actinopolyspora halophila* and eukarya such as the algae *Dunaliella*, tend to accumulate small organic molecules in order to tune the osmotic balance without perturbing intracellular functionality. These nonionic osmolytes frequently include the zwitterions trimethylglycine (TMG),[16] proline (Pro)[17] or trimethylamine *N*-oxide (TMAO),[18] and can also include polyalcohols such as sorbitol in fungi and algae, or ectoine in bacteria.[19] The molecular structures of these common osmolytes is shown in Figure 1.1.

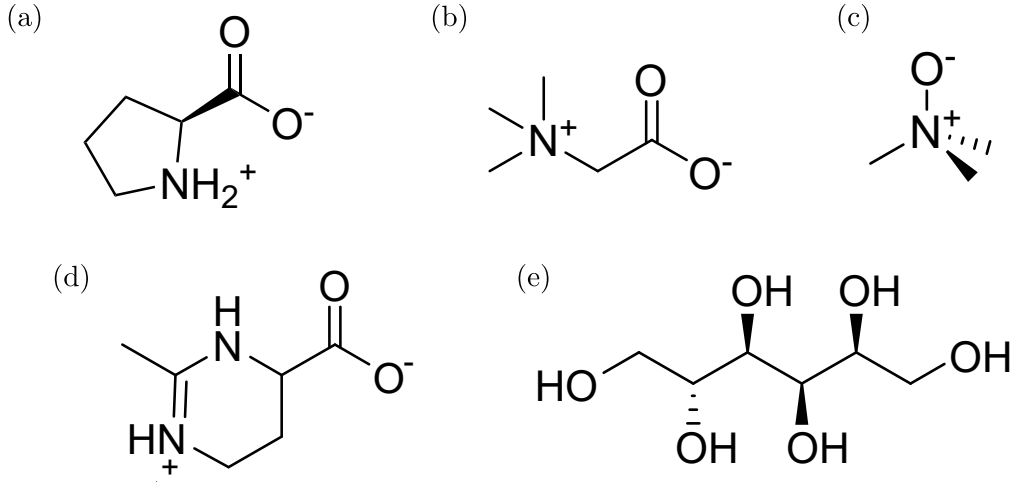

Figure 1.1: Molecular structures of some common osmolytes: (a) L-proline, (b) trimethylglycine, (c) trimethylamine *N*-oxide, (d) ectoine, (e) sorbitol.

The accumulation of ionic and nonionic solutes, also called 'salt-in'and 'osmolyte-in' mechanisms, respectively, present different biochemical challenges.[13] The former

requires adaptation of the genome to maintain resilient protein structures in high ionic strength conditions, frequently comprising an increase in the proportion of acidic amino acid residues expressed across the organism's proteome - namely, aspartic and glutamic acids - in preference to basic residues such as arginine or lysine.[15] This adaptation results in an increased negative charge on the protein surface, enhancing the magnitude of the electrostatic repulsion which contributes to protein stability. The latter mechanism does not necessarily require such widespread genomic adaptations but can instead require a significant expenditure of energy in order to perform biosynthesis or selective transport from the environment of the desired solutes.

Though the separation of these mechanisms is common in the literature, this divide is a simplification and real cytosolic fluids contain a complex mixture of both nonionic and ionic solutes. Examples even exist in the literature of organisms that possess the versatility to switch between the two mechanisms depending on the ionic strength of the surrounding environment, such as the extreme halophile *Halorhodospira halophila*.[20] These mechanisms to accumulate either, or a combination of, ionic and nonionc osmolytes to tune the overall osmotic balance are depicted in Figure 1.2.

The discussion so far has brought us to a central theme of this thesis: through evolution, nature has designed a cellular environment that simultaneously optimises for delicate interparticle forces and osmotic pressure, relying on a complex, multicomponent osmolytic environment. There is a long history of studying the influence of ions on biochemical stability, most notably the Hofmeister series first proposed in 1888, which orders different ions based on their ability to salt-out proteins from aqueous solutions.[24] This series has garnered much attention owing to its observed relevance in a range of biochemical contexts, including protein folding and enzyme activity, and much work has been performed with the aim of uncovering a molecular level description for these empirical observations.[25–27] However, the roles of

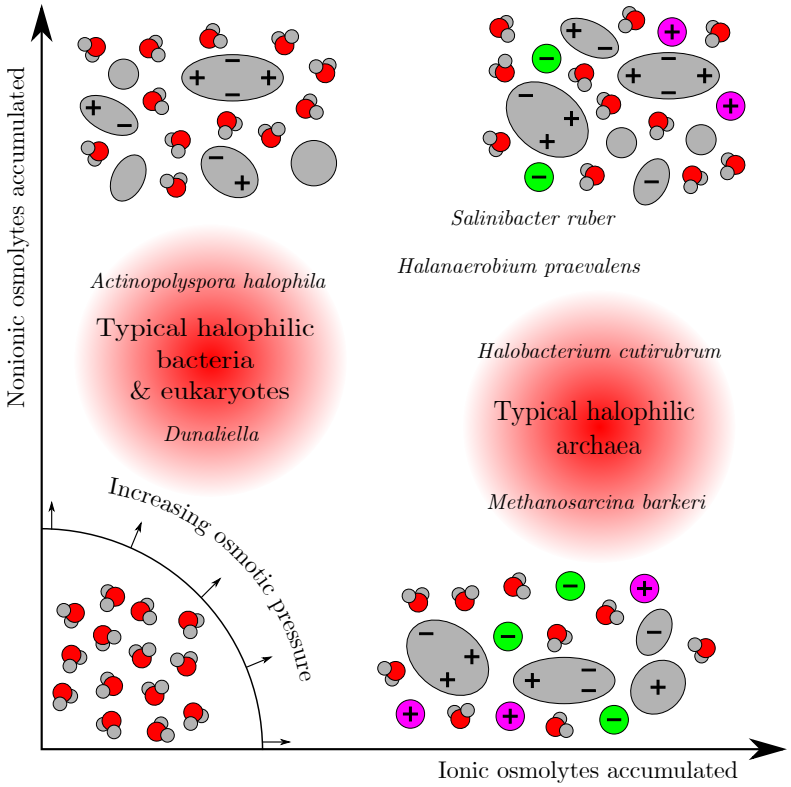

Figure 1.2: Schematic view of the osmoprotective strategies exhibited by halophilic organisms. Osmotic pressure can be adjusted by accumulation of ionic solutes (*e.g.*, inorganic salts) and/or nonionic species (*e.g.*, amino acids, and polyalcohols). Examples are shown of classes and species which are known to adopt particular strategies. Halophilic archaea such as *Halobacterium cutirubrum* and *Methanosarcina barkeri*[15] tend to accumulate ionic solutes, although there are examples of bacteria which also adopt this method, such as the extremely halophilic bacteria *Salinibacter ruber*[21] and *Halanaerobium praevalens*,[14,22] which exhibit intracellular salt concentrations similar to the growth medium. Moderately halophilic bacteria, *e.g.*, *Actinopolyspora halophila*,[18,23] fungi, and algae, *e.g.*, *Dunaliella*[13,17] instead accumulate nonionic, and often zwitterionic, osmolytes such as TMG and TMAO.

individual nonionic osmolytes and the synergies between different osmolytes have only begun to be studied recently. In particular, many of the common osmolytes introduced in this chapter possess molecular structures which combine a large dipole moment (the molecules are often zwitterionic in ambient conditions) and a hydrophobic residue. Such molecules are often termed dipolar/hydrophobic osmolytes,[28] and these properties will be valuable in rationalising their role in the model cytosolic fluids studied in this work.

As such, there are plenty of questions yet to be answered, particularly concerning the influence of osmolytes on interactions and structures within complex osmolytic

fluids. This thesis aims to unravel some of these complexities; in order to do so, one must first have an understanding of the forces and interactions that govern behaviours in liquids more generally. An overview of this framework is discussed in the next section.

1.2 | The Liquid State and Liquids at Interfaces

Interactions within liquids are complex, and for much of scientific history developing a full understanding of the liquid state of matter has presented a particular challenge. Yet liquids play a vital role in the natural and technological worlds, underpinning myriad technologies including in medicine and energy storage applications, and continued advancement hinges on having a firm grasp of the interactions within liquids.

Intermolecular forces arise from one of the fundamental forces, electrostatics, but due to molecular complexity and interactions on different length scales it is often useful to separate molecular interactions into various contributions to an overall interaction potential. A few such contributions will be discussed in the following section.

1.2.1 | Intermolecular Forces

In a simple case of two uncharged atoms or small molecules i and j in a vacuum, at most separations - excepting any steric repulsion due to overlapping electron clouds at very small separations - the dominant interaction acting between the atoms is the van der Waals (vdW) interaction. This arises due to favourable interactions between permanent or induced dipoles and is attractive at all distances, and takes the form for the pair potential $w_{ij}(r)$ given in Equation 1.1 if the dipoles are free to rotate.

$$w_{ij}(r) \propto -\frac{1}{r^6} \tag{1.1}$$

The total interaction energy U can also be calculated between macroscopic objects by summing over all interaction contributions. For example, the vdW interaction can be calculated for an atom or small molecule interacting with a macroscopic surface, which results in a $U \propto -r^{-3}$ scaling law, *i.e.*, longer range than the pure pair potential. Further analysis can be used to determine the scaling of the vdW interaction between two macroscopic surfaces or a sphere and a flat surface, which can be shown to be $U \propto -r^{-2}$ and $U \propto -r^{-1}$, respectively, and this approach will be essential when we consider interactions between surfaces in future sections. A schematic of these different geometries is shown in Figure 1.3.

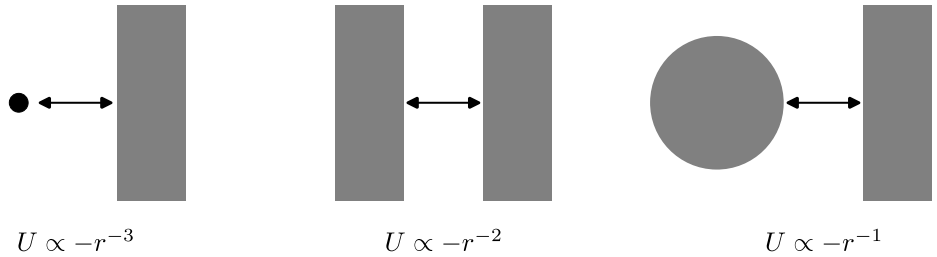

Figure 1.3: Van der Waals interaction energy U between macroscopic bodies of different geometries separated by distance r. Left: an atom or small molecule interacting with a flat surface. Centre: two interacting flat surfaces. Right: a sphere interacting with a flat surface.

If, instead of uncharged atoms, we now consider the interaction between full ionic charges, the contribution due to Coulombic interaction must also be considered. This Coulombic contribution to the pair potential for two charges q_i and q_j interacting across a dielectric medium takes the form shown in Equation 1.2:

$$w_{ij}(r) = \frac{q_i q_j}{4\pi\epsilon_{\mathrm{r}}\epsilon_0 r} \tag{1.2}$$

where q is the charge of each ion, ϵ_{r} is the relative permittivity of the medium, and ϵ_0 is the permittivity of free space.

This interaction is of great relevance to electrolytes, fluids that contain mobile charge carriers such as ions, and the class of liquids that are studied in this work. The Debye-Hückel theory provides a framework for understanding electrostatic interactions in dilute electrolytes, which are more complex than the simple pairwise

interactions due to the many ions present, allowing the electric potential to decay more rapidly away from a reference ion than would be predicted by a pairwise Coulombic interaction. This more rapid decay of the potential is due to the 'ionic atmosphere' arising from surrounding counterions more effectively screening the potential. In a 1:1 electrolyte, the electric potential $\psi_j(r)$ arising from a point charge q_j is described by Equation 1.3:

$$\psi_j(r) = \frac{q}{4\pi\epsilon_\mathrm{r}\epsilon_0 r}\mathrm{e}^{-\kappa_\mathrm{D} r} \tag{1.3}$$

where κ_D^{-1} is the Debye length, the length scale over which the central charge is screened. The Debye length can be expressed as Equation 1.4:

$$\kappa_\mathrm{D}^{-1} = \sqrt{\frac{\epsilon_\mathrm{r}\epsilon_0 k_\mathrm{B} T}{2e^2 n_0}} \tag{1.4}$$

where k_B is the Boltzmann constant, T is the temperature, and n_0 is the number density of ions in the solution. A comparison between the radial decay of the electric potential according to Coulomb's law and Debye-Hückel theory is shown in Figure 1.4, illustrating the more rapid decay of the electric potential in the Debye-Hückel picture. Equation 1.3 is related to the pair potential between two charges q_i and q_j by Equation 1.5.

$$w_{ij}(r) = q_i\psi_j(r) \tag{1.5}$$

In its linearised form, the Debye-Hückel theory outlined here is exact at infinite dilution, but begins to fail at concentrations greater than 1 mM. In its non-linearised form, the theory can account for properties of electrolyte solutions at higher concentrations, up to around 1 M.[29] At concentrations greater than this, experimental measurements on electrolytes become increasingly divergent from this theoretical framework, for example in the observation of a non-monotonic screening length.[30] Such divergent behaviour arises from greater electrolyte complexity, with ions oc-

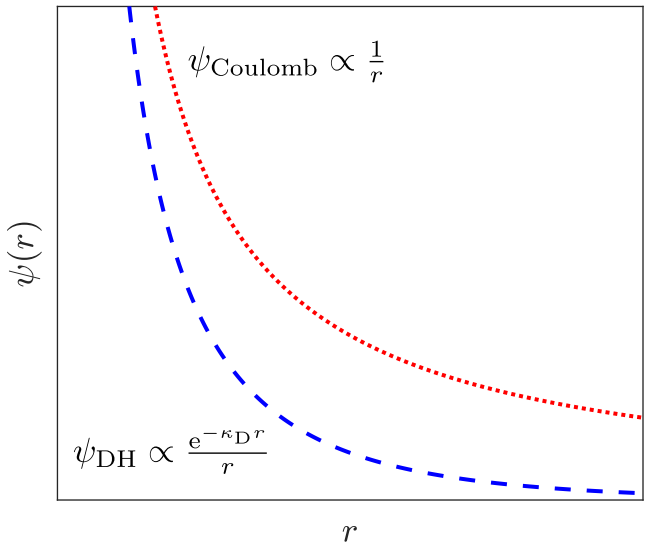

Figure 1.4: Electric potential ψ as a function of radial distance r away from a positive point charge. In a dielectric medium, the potential is purely Coloumbic and decays as r^{-1} (ψ_{Coloumb}, dotted red line). In a dilute electrolyte, according to Debye-Hückel theory the potential decays more rapidly (ψ_{DH}, dashed blue line).

cupying a significant volume fraction of the solution, and exploring the properties of these fluids - both with experimental measurements and developing theoretical frameworks - continues to be an active area of research.[30–33]

1.2.2 | Liquids at Interfaces

Liquids can be found in contact with or confined between interfaces in many natural processes.[34] Examples range from geological (*e.g.*, mineral weathering[35] and soil stability[36]), atmospheric (*e.g.*, aerosols[37] and ice nucleation[38]) and biological processes (*e.g.*, protein folding[39] and cell membrane dynamics[40]). Solid-liquid interfaces are also of paramount importance in technological applications, such as the electrode-electrolyte interface in energy storage devices,[41] membranes in desalination technologies,[42] or drug delivery agents.[43]

The Electrical Double Layer

When exposed to a liquid, many interfaces - including physiological ones - gain a net charge, arising from mechanisms including the ionisation of surface groups, such as the proton dissociation from carboxylate functional groups, or the adsorption of ions onto a surface, such as the binding of Ca^{2+} to zwitterionic head groups of lipid bilayers.[29] Such charge can influence the arrangement of species, particularly when they also possess charge, in proximity to the surface. Helmholtz was the first to theorise about the structure of the interface between a charged surface and an electrolyte, proposing the presence of an electrical double layer (EDL).[44] The Helmholtz model describes a situation in which the interfacial charge is balanced by a plane of hydrated counterions, treating this interface as two capacitor plates with a linearly changing potential moving away from the surface.

In the early twentieth century, Gouy and Chapman expanded on the Helmholtz model by incorporating the thermal motion of ions in an electrolyte solution.[45,46] The Gouy-Chapman model challenges the idea that the counterions are tightly bound at the surface, instead suggesting that they are present in a diffuse layer near the surface. The model combines the Poisson equation for describing the variation of a potential field around a charge distribution, and the Boltzmann distribution which describes the statistical distribution of particles in thermal equilibrium. The framework provided by the Poisson-Boltzmann (PB) equation developed by Gouy and Chapman allows for the prediction of properties in this updated model of the EDL, including the variation of electric potential away from the charged interface. The general (nonlinear) form of the PB equation is shown in Equation 1.6:

$$-\nabla^2\psi(r) = \frac{e}{\epsilon_0\epsilon}\sum_i z_i\rho_{0,i}\mathrm{e}^{-z_i e\psi(r)/k_\mathrm{B}T} \tag{1.6}$$

where the sum is over all ionic species i, z_i is the ion valency and $\rho_{0,i}$ is the bulk ion density.[29]

In the 1920s, Otto Stern proposed a new model, addressing the limitations of both the Helmholtz and Gouy-Chapman models.[47] The Stern model invokes a hybrid of the two previous models, proposing that the double layer comprises two regions: the compact (Stern) layer, consisting of ions adsorbed to the surface; and a diffuse layer of ions permeating into the bulk solution, as described by Gouy and Chapman. The combined model allows for the finite size of ions and the adsorption of ions to the interface.

A final valuable advancement of the EDL model was made by Graheme in the mid-twentieth century. Graheme further refined the Stern layer, separating the inner and outer Helmholtz planes (IHP and OHP) in order to differentiate between specifically adsorbed ions and hydrated ions at the interface, respectively.[48] Further advancements have been made since, including the incorporation of a variable relative permittivity as a function of distance from the interface,[49] and quantum mechanical concepts at metallic surfaces.[50] A schematic of the EDL in the Graheme model and a plot of the electrical potential as a function of distance from the surface is shown in Figure 1.5.

DLVO Theory

It is useful to consider the interactions between two charged surfaces. These interactions can often be described using the DLVO theory, named after the four scientists - Derjaguin, Landau, Verwey and Overbeek[51,52] - to whom the theory can be credited. This theory considers the sum of the two major interactions that act between the two equivalent, charged surfaces: the attractive van der Waals interaction that we considered in the previous section, and the repulsive double layer force to which we shall now turn.

As two surfaces approach each other, their diffuse layers of counterions overlap, thus elevating the counterion concentration in this region. This results in an excess osmotic pressure relative to the bulk fluid, which generates an entropic driving

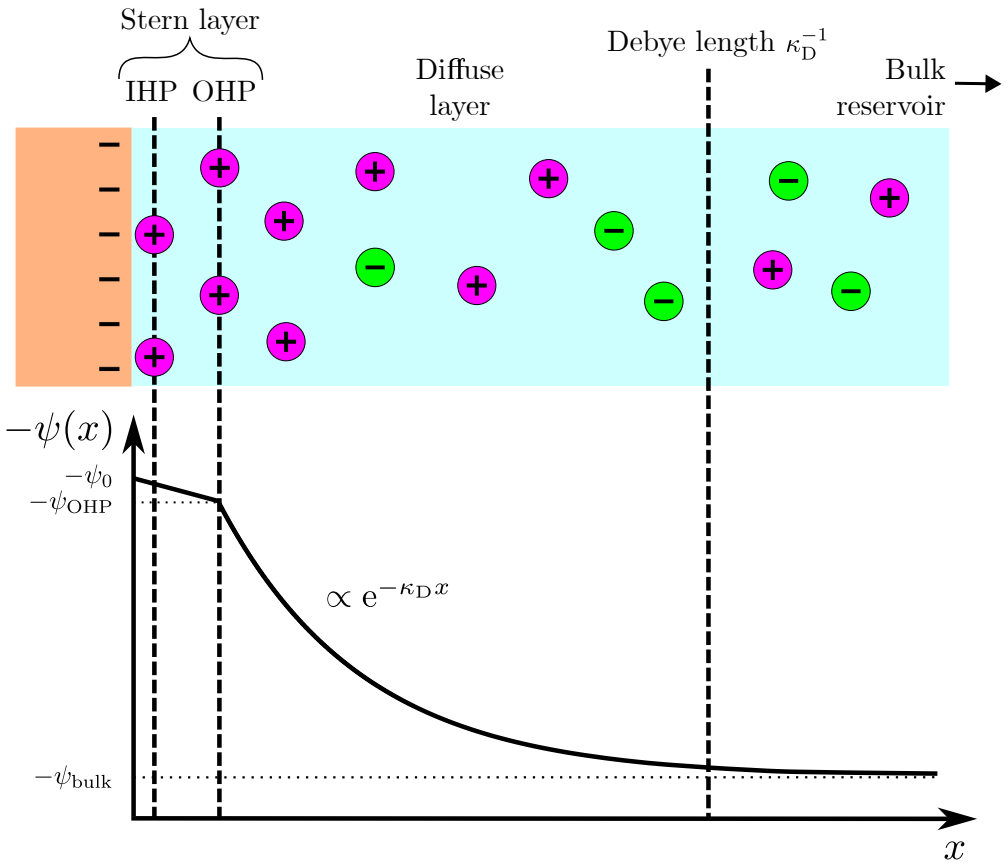

Figure 1.5: Top: schematic of the EDL formed between an electrolyte and a charged surface. Bottom: variation in the electric potential $\psi(x)$ as a function of distance from the surface x. The Stern layer can be comprised of a mixture of hydrated or dehydrated counterions adsorbed onto the negatively charged surface. In the diffuse layer, at distances beyond the OHP (for clarity, the IHP is not shown), the ions obey the Poisson-Boltzmann equation and the potential decays exponentially into the bulk reservoir.

force, or disjoining pressure, to repel the surfaces apart. At the midpoint of the two surfaces separated by a distance D, the disjoining pressure $\Pi(D)$ can be described by Equation 1.7:

$$\Pi(D) = \frac{2\sigma^2 e^{-\kappa_D D}}{\epsilon_r \epsilon_0} \tag{1.7}$$

where σ is the surface charge density.

By noting the dependence of the double layer repulsion on $e^{-\kappa_D D}$ and recalling the D^{-n} dependence of the van der Waals interaction, it is clear that the van der Waals attraction should dominate as the surface separation D approaches zero, resulting in the adhesion of the surfaces. Depending on the ion concentration and

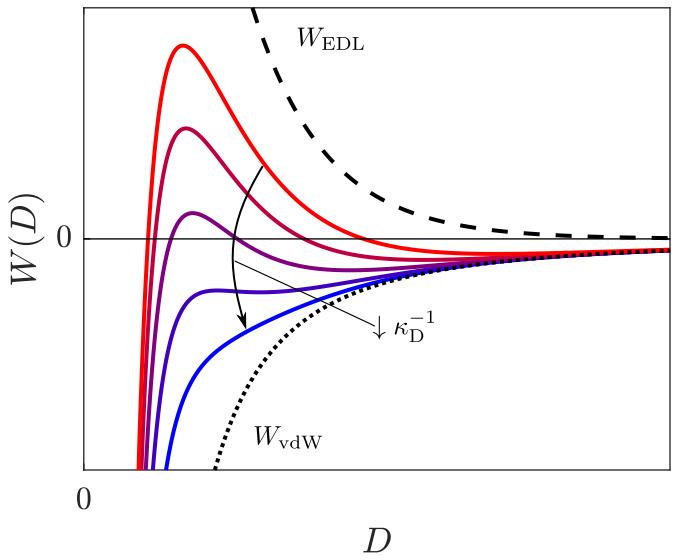

Figure 1.6: Interaction energy W as a function of surface separation D profiles of the DLVO interaction between two surfaces arising from the combined double layer repulsion (W_{EDL}, dashed line) and van der Waals attraction (W_{vdW}, dotted line). The trend from long (red) to short (blue) Debye lengths κ_{D}^{-1} arising from increasing ion concentration is shown.

surface charge, however, the double layer repulsion or van der Waals attraction may dominate at intermediate separations, resulting in condition-dependent energy barriers to adhesion and secondary (flocculation) minima. These different types of interaction potential are displayed in Figure 1.6.

Non-DLVO Interactions

The DLVO theory is a continuum model: it relies on a mean field approach to describe the interactions across fluids. These theories rely on the bulk properties of the confined medium, such as the density, refractive index and dielectric permittivity, yet it has been observed that these values deviate from the bulk value when the surface separation decreases to below a few molecular diameters.[53] Therefore, at small surface separations - at molecular length scales - such a model on its own should not be expected to accurately predict the real, measured interaction.

Between two hard, smooth surfaces, additional non-DLVO interactions can be seen to arise from considerations of molecular structure, owing to the packing con-

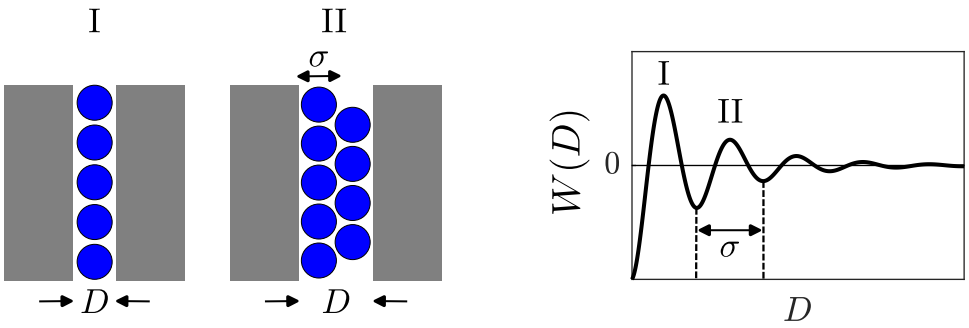

Figure 1.7: Left: cartoons illustrating the ordering that takes place when hard spheres of size σ are confined between two surfaces. Right: schematic of the structural contribution to the interaction energy W between two surfaces confining a liquid. Cartoons I and II refer to the equivalently labelled positions on the interaction energy plot.

straints of molecules in the finite gap between the two surfaces. In such a scenario, molecules can form ordered layers of thickness dependent on the size and interactions of the liquid constituents. This layering gives rise to a decaying oscillatory density profile - akin to the radial density oscillations around a central molecule in the bulk fluid - reflected in the additional contribution to the interaction energy between two surfaces. These short-range interactions are often referred to as 'structural' or 'solvation' forces, or 'hydration' forces when discussing systems with water as the solvent.

In Figure 1.7, the oscillatory interaction energy contribution is illustrated with simple steric arguments using hard spheres, where the oscillation period corresponds to the molecular diameter σ of the confined molecules. However, measurements across real liquids can give rise to more complex behaviours, depending on the type being studied. In high concentration electrolytes, for example, the measured oscillatory wavelength can be either dominated by density fluctuations (molecular structure), as previously discussed, or can instead arise from charge-charge interactions.[54,55]

1.3 | Experimental Measurements of Surface Interactions

Various techniques have been developed in order to measure the interaction profiles between two surfaces confining a liquid; that is, the interaction as a function

of surface separation. In this work we use the Surface Force Balance (SFB) or as sometimes called, the Surface Force Apparatus (SFA), to measure surface interactions. This apparatus allows for the measurement of forces between two macroscopic surfaces confining a liquid, and has been used to reveal a range of phenomena in soft and biological matter over the past half-century.[56]

Developing on the work of Bailey and Courtney-Pratt,[57] the SFA was first used to study vdW interactions between macroscopic muscovite mica surfaces at small separations by Tabor and Winterton.[58] Subsequent extensions by Israelachvili, Tabor and Adams[59,60] extended the range of distances over which interactions could be measured and allowed for the study of forces across thin films of liquids. In this thesis, the version of the SFB described by Jacob Klein is used to perform measurements of surface interactions.[61] With one of the surfaces mounted on a spring of known stiffness, the surface interaction force can be determined as the two surfaces are moved together by monitoring the deflection of the spring. The absolute distance between the two surfaces - prepared with silver mirrors on their back sides - is determined using interferometry.

Different adaptations of the SFB exist, allowing for specialist study of different interfacial phenomena across various systems, including non-polar liquids,[62,63] dilute[64] and concentrated electrolyte solutions,[30] ionic liquids,[65] polymers,[66] liquid crystals[67] and amphiphiles.[68] As we will discuss in Chapter 2, muscovite mica is the most common surface employed in surface forces measurements, but the use of other surfaces has been explored, including gold,[69,70] graphene,[71,72] liquid mercury[73] and hydrophobic surfaces.[74] Further adaptations include the ability to measure dynamic processes, such as lateral, shear forces across confined liquid films,[75] and structural determination of a confined liquid with an X-ray scattering approach coupled with the SFA.[76]

As the names of these techniques suggest, experimentally it is often most practical to measure the force acting between the surfaces. Depending on the experimental

geometry, it is possible to relate this to an interaction energy which is the measure through which we have been discussing the various contributions to the overall surface interaction in this chapter. Determining the interaction energy therefore allows for better comparison to models and theoretical predictions, and the relation that allows for this interconversion will be outlined in Chapter 2.

1.4 | Experimental Measurements of Bulk Structure

The measurement techniques described in the previous section employed the presence of a surface in order to measure an interaction profile across the intervening liquid. However, many features of the interaction profiles discussed in the preceding sections are intrinsically related to the bulk properties and structure of a liquid. For example, the structural contribution to the interaction energy, illustrated previously in Figure 1.7, arise from the short-range correlations of molecules around one another. Furthermore, the decay length of the double layer repulsion is related to the bulk ion concentration in the fluid which, in turn, is related to the average distance between these ions. Accordingly, these techniques can be complimentary to direct experimental measurements of the bulk structure of a liquid, which we will introduce in this section.

The scattering of radiation by matter can be used to extract information about atomic and molecular arrangement in that matter when the wavelength of the radiation is of similar magnitude to the spacing between atoms. In this thesis, we will specifically use neutron and X-ray scattering in order to perform structural determination of electrolyte solutions. Other forms of electromagnetic radiation or subatomic particles such as electrons can be used for structural determination in different contexts and for different sample types.

Owing to fundamental experimental limitations, these techniques on their own do not necessarily yield the fullest amount of detail in regard to the structural arrangement of disordered matter. Instead, these techniques can be even more pow-

erful when coupled with computer simulations; a synergy between experiment and simulation can be even more informative than either of the two approaches on their own. Since the mid-twentieth century when the first simulations were carried out for a hard sphere liquid,[77] the development of computing power and availability has enabled the increased sophistication of simulation techniques. Monte Carlo (MC) and Molecular Dynamics (MD) are two of the most widely used techniques in modelling matter at the atomic scale.[78] The former explores a range of system configurations stochastically and considers the probability of the resulting configuration using the Boltzmann distribution.[79] The latter determines the time-evolved dynamics of the system by solving the motion of particles classically with Newton's equations. In this work, we use the Dissolve package to perform structural determination from our scattering data, which employs a combined MC-MD approach to drive a simulated structure towards experimentally-determined datasets.[80]

1.5 | Overview

This thesis will present the results of studies on model cytosol solutions, using surface forces measurements in addition to bulk, structural determination methods. The overall aim of this thesis is to investigate the role of different cytosolic components - from ions to molecular osmolytes, both individually and in more complex mixtures - in modulating interactions and structures of such fluids, and relating these results to biological function and the evolutionary choice to accumulate such components.

After discussing the techniques employed in this thesis in the following chapter, experimental results are first presented in Chapter 3. Here, through the lens of surface forces measurements across simple, dilute electrolytes, we will further extend the discussion surrounding properties of these fluids introduced in this chapter. These measurements will provide a framework through which to understand the important features that can be observed using the SFB technique, upon which subsequent chapters build as the complexity of the fluids is increased.

Chapter 4 investigates the role of zwitterions in modulating interactions between charged surfaces using the surface force balance. The amino acid proline is used as the primary osmolyte of interest, but the results are also compared to another common zwitterionic osmolyte, trimethylglycine. This chapter also considers the role of added salt in zwitterion-salt mixtures in altering interactions and surface structure relative to the zwitterion-only measurements.

Zwitterion-ion mixtures are further studied in Chapter 5 using structural determination methods, employing a combined neutron and X-ray scattering approach. Various features of the solution structure in two mixtures containing trimethylglycine with either potassium or sodium chloride are investigated, with a particular focus on the nature of TMG-ion interactions and the effect of ion identity on the presence and structure of TMG clusters in the solutions.

In Chapter 6, a pairing of osmolytes commonly found in nature, protein-stabilising TMAO and protein-destabilising urea, is investigated. Through the measurement of surface forces across fluids containing the osmolytes, both individually and in a mixture, we present a novel insight into the separate and combined contribution of the osmolytes to colloidal stability. Their role in modulating interactions between charged surfaces is investigated, particularly at small surface separations, revealing a molecular insight into the evolutionary choice to accumulate this specific mixture.

A final series of measurements of surface interactions are presented in Chapter 7 across aqueous solutions containing glycine oligopeptides, a model peptide backbone. The oligopeptide length and concentration dependence on the measured interactions is investigated, revealing oligomer dependent effects on the measured interfacial structures.

Finally, an overview of this thesis is presented in Chapter 8. The results contained in this work reveal a range of interactions and structures that can be exhibited upon tuning the composition of aqueous solutions which can be drawn upon to build evolutionary strategies, allowing survival across a wide range of environments.

2 | Experimental Methods

2.1 | Surface Forces Measurements

The surface force balance (SFB) has been used in this work to measure interactions across liquids of interest, confined between charged surfaces. This section details the technique and relevant experimental procedures.

The key feature of the SFB is a pair of muscovite mica surfaces which have been back-silvered and glued onto cylindrical glass lenses, arranged in a crossed-cylinder orientation. Through white light interferometry, the separation between the surfaces D can be determined with sub-nanometre resolution. Moving the surfaces towards or away from one another with the aid of a mechanical drive allows for the measurement of normal forces acting across a fluid of interest, determined through the deflection of a Hookean spring upon which the lower lens is mounted. A schematic illustrating these key features is shown in Figure 2.1.

2.1.1 | Mica and Lens Preparation

Muscovite mica is an ideal candidate for use as the surface material in a surface forces measurement. A naturally occurring mineral, it can be easily cleaved along its cleavage plane in order to generate atomically smooth facets of centimetric areas and micrometric thicknesses, which are also transparent to visible light, necessary for performing white-light interferometry.

Freshly cleaved mica will readily adsorb contaminants from the surroundings in order to lower its surface energy. Therefore, preparation of the mica surfaces must be performed in a way that minimises the risk of contamination during both the initial cleaving of the mica and the preparation of the surface for the experiment. All work to cleave and prepare the mica surfaces is performed in a laminar flow hood (LFH), which draws air through a high-efficiency particulate air (HEPA) filter and passes

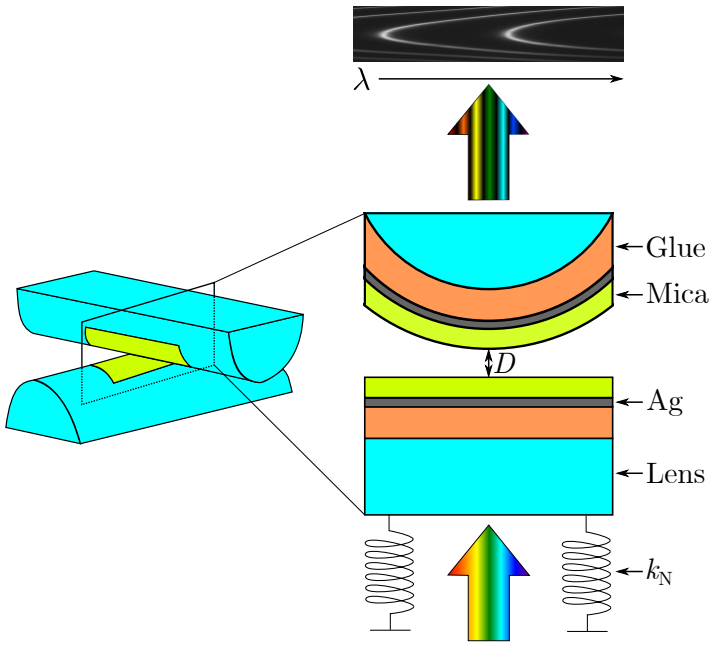

Figure 2.1: Summary of the SFB. Back-silvered mica surfaces are glued onto cylindrical glass lenses of radius $\sim$ 1 cm. Mounted in a crossed-cylinder orientation, the surfaces can be moved towards or apart from one another using a mechanical or piezoelectric drive. The lower lens is mounted onto a spring of known spring constant k_N. White light passes through the interferometric cavity created by the silver-mica-medium-mica-silver stack, and the emergent light is passed into a spectrometer and then a camera. The resulting fringes of equal chromatic order (FECO) are used to determine mica thickness, surface separation D, and the radius of curvature of the lenses R.

the air in a laminar flow in the direction of the user, thus creating a environment in which areas upstream are not contaminated by any particle generation downstream. In addition, all glassware and tools used in these processes are cleaned in acid before use. For glassware, this involves cleaning in piranha solution, a 1:3 mixture of hydrogen peroxide and sulfuric acid, which acts as a strong oxidiser. All stainless steel tools are cleaned in nitric acid. Once cleaned in acid, all tools are rinsed in ultrapure water (Milli-Q® IQ 7003, 18.2 MΩ cm, TOC $<$ 3 ppb) and stored either dry or in absolute ethanol.

Mica (optical-grade ruby muscovite mica, S & J Trading Inc.) is cleaved by hand to yield step free facets of centimetric area and thickness of size 2 - 5 µm. During cleaving, the thickness of the facets can be estimated from the colour and intensity of interference patterns; abrupt colour changes correspond to steps in the crystal

plane. Facets of appropriate thickness are then cut out using a hot platinum wire, producing a burnt edge of the mica, ensuring that where possible the cleaved piece is upstream of the platinum wire in order to minimise surface contamination by platinum nanoparticles.[81] After being cut, the facet is adhered to a freshly cleaved, thick mica sheet (the base sheet), upon which multiple facets can be collected until the base sheet is full or until it has been exposed to air for 1 - 2 hours. A semi-transparent silver layer of thickness $\sim$ 45 nm is deposited onto the base sheet via thermal evaporation of silver shot (Alfa Aesar, 99.999%) in a high vacuum ($\sim$ 10^{-6} mbar) using an Auto 306 thermal evaporator (HHV Ltd.). The deposition is performed at a rate of $\sim$ 0.1 nm s^{-1} whilst being monitored by a quartz crystal microbalance (6 MHz gold quartz monitor crystals, INFICON) and controlled by adjusting the heater current and the position of a mechanical shutter. The target thickness is chosen as a compromise between reflection and transmission of light at the mica-silver interface. After silver deposition, the base sheet is stored under vacuum in a desiccator until required. An example silvered base sheet is shown in Figure 2.2.

To prepare the back-silvered mica for use in an experiment, a scalpel is used to cut the mica into pieces with size of magnitude $\sim$ 1 cm^2, which can then levered up by inserting a clean needle between the base sheet and the burnt edge of the mica. Clean tweezers are used to lift up the mica pieces, which are then glued using an epoxy glue (EPON^{TM} Resin 1004F, Miller-Stephenson Chemical Co., Inc.) to a cylindrical glass lens, such that the freshly exposed mica faces upwards. Two lenses are prepared from a single facet of mica in order that both lenses are made from mica of the same thickness. An image of two prepared lenses is shown in Figure 2.3.

2.1.2 | Surface Force Balance Setup

The pair of prepared lenses are mounted within two removable sections of the SFB: the lower lens in the boat and the upper lens in a lens holder which is attached

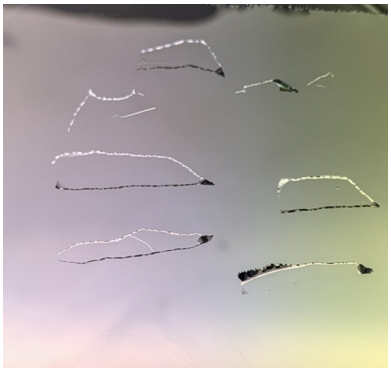

Figure 2.2: A silvered mica base sheet, upon which mica facets are stored after being cleaved and cut.

Figure 2.3: The lenses used in an SFB experiment, after the silvered mica has been cut to size, removed from the base sheet and then glued onto the glass lens, silver side down.

to the top part. Within the SFB, the lenses are mounted such that their axes are oriented perpendicular to one another. The inside of the SFB chamber, along with the boat and top part used in this work, are shown in Figure 2.4.

Within the boat, the lower lens is secured into a lens mount which in turn is mounted to a pair of normal leaf springs. These are Hookean springs of known spring constant k_{N}, as calculated from a calibration procedure prior to measurement involving applying a series of weights of known mass and measuring the deflection of the springs. Below the lens is a quartz window which allows transmission of white light to the lens.

The upper lens is secured into a lens mount attached to a sectored piezoelectric tube, suspended from the top part by a pair of vertical leaf springs. The piezoelectric tube allows the lens to be translated both vertically and horizontally, for measurement of normal and lateral forces, respectively. Deflection of the vertical leaf

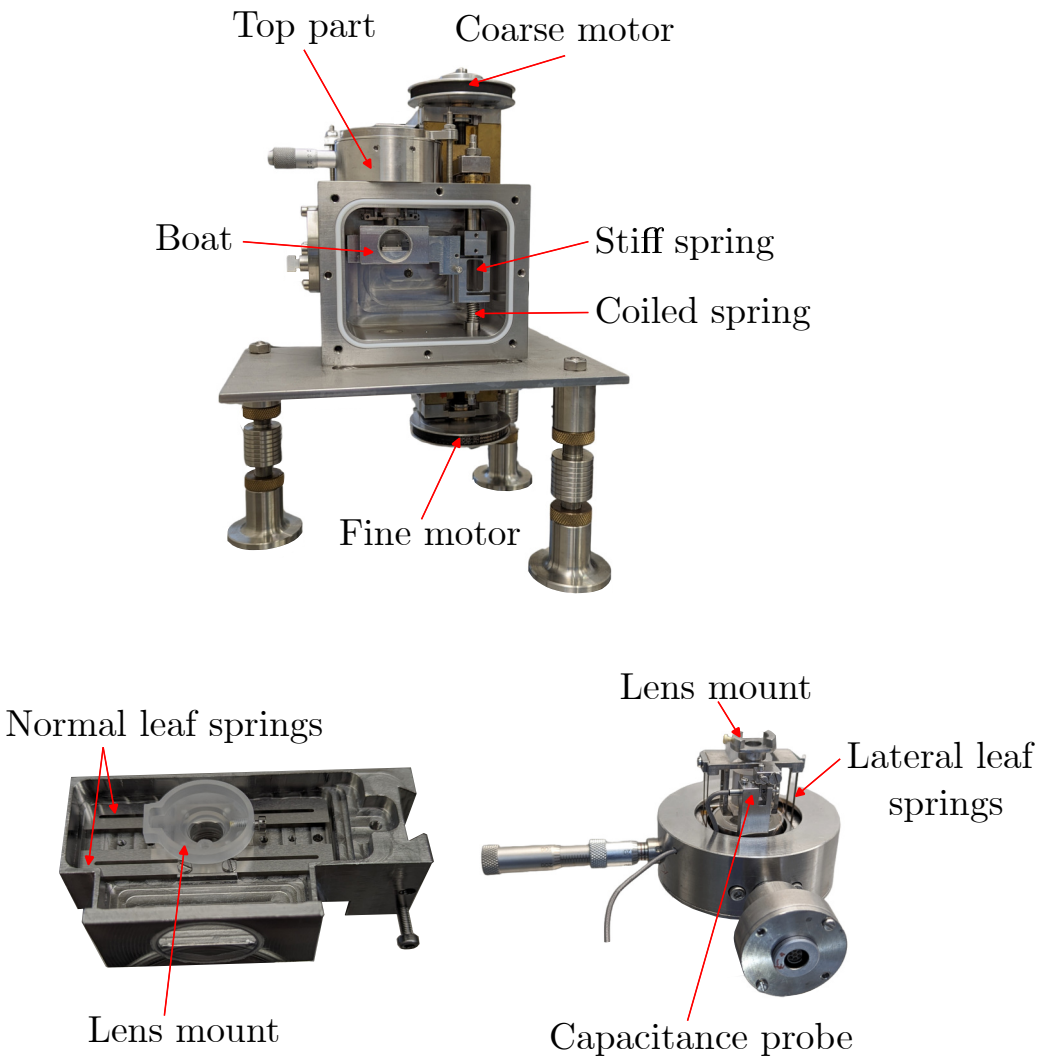

Figure 2.4: Top: the inside of the SFB chamber. Bottom: the boat (left) and top part (right) in which the two lenses are mounted, and which are then loaded inside the SFB chamber.

springs can be measured using an air gap capacitor, comprising a small steel plate and a capacitance probe. Light emergent from the upper lens can be transmitted to the spectrometer through a second quartz window in the top part.

After the lenses are mounted and the removable sections of the SFB are returned, the chamber is sealed and the apparatus can be moved to the temperature-controlled measurement room (294 K), within which the chamber is placed on an isolation table. This table sits on the ground floor of the laboratory on a stack of rubber, marble, rubber and concrete. This setup, in addition to a box that surrounds the instrument during usage is designed to minimise the effect of external vibrations. The position

of the SFB on the isolation table is set to allow reflected white light through the bottom window of the apparatus with maximum intensity, and the apparatus is set level by adjustment of the tripod legs.

There is a direct connection between the boat and an electric stepper motor drive, referred to as the 'coarse' motor, which can be used to alter the separation between the two lenses. This drive allows for motion on the order of a centimetre with a precision on the order of a micrometre. This drive is used to position the lens prior to making measurements, and owing to the large vibrations generated by its use, is always disabled before a measurement is made.

The position of the boat in the chamber can be adjusted by a second, identical electric stepper motor drive referred to as the 'fine' motor, separated from the boat by a differential spring mechanism. This mechanism comprises a linear combination of a stiff spring and a coiled spring, and allows for motion on the order of a millimetre with precision on the order of a nanometre. As well as the finer control over the separation between the lenses, the fine motor confers the additional benefit of damping the mechanical noise from the motor, thus is suitable for use in performing the surface forces measurements.

Finally, the position of the upper lens can be controlled by application of an external voltage to the piezoelectric tube to which it is attached, referred to as the 'piezo'. The piezo has five sectors: four on the outside face of the tube, and one on the inside. Voltages can be applied independently to the individual sectors, allowing for a controlled expansion or contraction of the piezo, and a linear vertical motion can be induced by applying equal voltages to the four outer sectors, the inner sector only or to all five sectors. If one wishes to investigate frictional forces in addition to normal forces, lateral motion of the piezo can also be generated by applying an equal but opposite voltage to opposite sectors on the outside face.

A schematic illustrating the features of the SFB discussed in this section is shown in Figure 2.5.

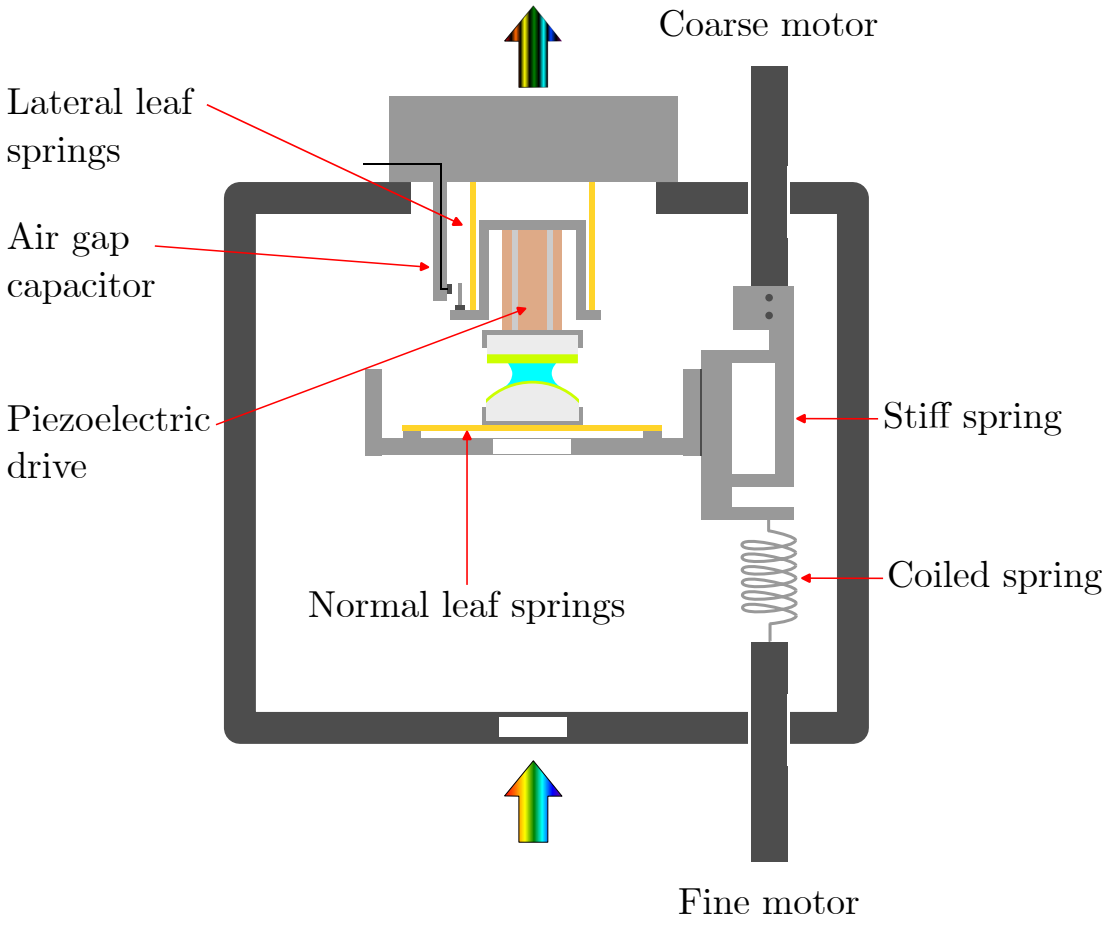

Figure 2.5: Schematic of the interior of the surface force balance. The lower lens mounted within the boat on a set of two normal leaf springs. The position of the boat within the SFB interior is controlled by the use of the coarse and fine motors, where the coarse motor shaft is coupled directly to the boat and the fine motor shaft is coupled via a differential spring mechanism comprising a series combination of a stiff and coiled spring. The upper lens is mounted to a sectored piezoelectric drive, which can produce both normal and lateral motions between the lenses. Lateral motion of the upper lens is enabled through the deflection of a pair of lateral leaf springs, which separate the lens from the main body of the SFB. Deflection of these springs can be measured using an air gap capacitor.

2.1.3 | Liquid Preparation

The liquid of interest is prepared on the same day of use and injected between the two lenses with a clean Hamilton glass syringe. Solutions are made by weighing a known mass of solute (used as received) and ultrapure water (Milli-Q® IQ 7003, 18.2 MΩ.cm, TOC $<$ 3 ppb) into an acid cleaned glass flask. The solution is then mixed using a magnetic stirrer bar.

The liquid of interest can be injected between the lenses using a clean Hamilton® glass syringe. In the first instance, $\sim$ 0.3 mL of fluid is injected to form both a bridging droplet between the two mica-coated lenses and to provide an reservoir of liquid to be held in the surrounding cup. The temperature of the fluid is allowed to equilibrate with the surroundings before commencing force measurements.

Throughout this work, concentrations of the investigated solutions are reported with the units, molal (m), the moles of solute per kilogram of water.

2.1.4 | Optics and Image Analysis

Multiple beam interferometry is used to measure the separation between the lenses. Collimated white light, generated by an Ar-Xe lamp, is directed through a window at the bottom of the SFB chamber. Multiple reflections take place within the silver-mica-medium-mica-silver interferometric cavity, and only certain wavelengths of light emerge; this emergent light is passed through a microscope and focussed onto a grating spectrometer using a prism. The resulting interference pattern, as monitored and recorded using a QImaging Retiga R6 charged-coupled device (CCD) camera, takes the form of a series of Fringes of Equal Chromatic Order (FECO), where the characteristic pattern of the fringes, shown in Figure 2.6, arises due to the geometry of the cavity. The FECO are observed as doublets due to the birefringent nature of mica. During an experiment, FECO are monitored using a LabVIEW™ program and can be used to determine the surface separation D, the radius of curvature of the lenses R, and the mica thickness. Here we reproduce the formal mathematical treatment for FECO developed by Tolansky[82] and adapted for use in the surface force balance by Israelachvili.[83]

Before any liquid is introduced between the surfaces, they are brought gently into contact in air. Strong adhesion between the mica surfaces results in a large region of surface contact, strongly deforming the glue layer, as seen in the flattening of the fringes. A fringe of odd order is chosen and labelled as the p fringe, with fringes

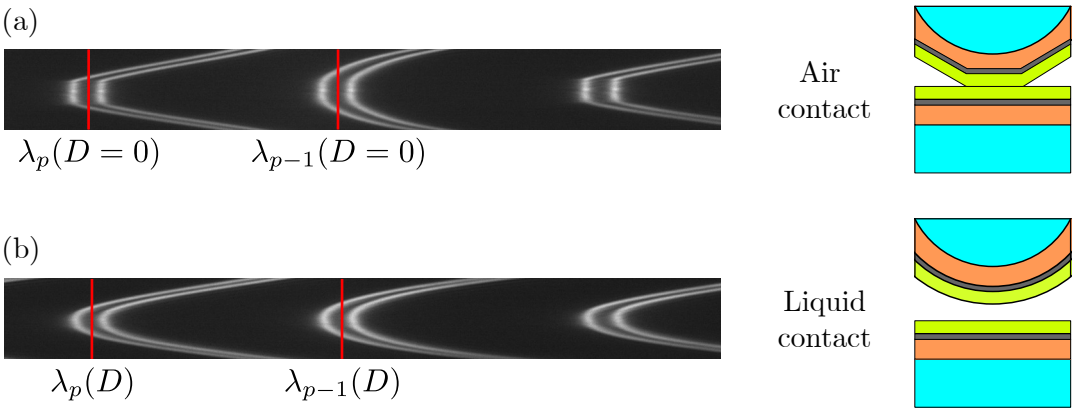

Figure 2.6: Example fringes of equal chromatic order (FECO) recorded during the calibration process, where the surfaces have been brought into contact in (a) air and (b) liquid. The fringe positions for the p and p-1 fringes, λ_p and λ_{p-1} are indicated by red lines. The surface contact geometries are illustrated in both cases. (a) The recorded FECO during air calibration, where the mica surfaces have been brought into contact in air. Strong adhesive forces result in the flattening of the fringes, enabled by the deformation of the glue layers. In air, there is a clear difference between the odd and even fringes: the even fringes are those with greater curvature. The left-most odd fringe is termed the p-fringe. (b) The recorded FECO during liquid contact.

at larger wavelengths being labelled as $p-1$, $p-2$, and so on. In contact, the wavelengths of the p and $p-1$ fringes, $\lambda_p(D=0)$ and $\lambda_{p-1}(D=0)$, are calculated from the recorded pixel position relative to the mercury green (546.1 nm) and yellow (579.1 nm) emission line, obtained by passing light from a mercury-vapour lamp into the spectrometer.[84] This allows the precise mica thickness to be calculated.

During a measurement, a CCD camera is used to record a series of images of 140 vertical by 2688 horizontal pixels at a rate of approximately 5 Hz. Image processing is performed in MATLAB® by tracking the centre of mass of a specified fringe at every vertical pixel position. This centre of mass profile can be fitted with a parabola, the peak of which gives the pixel position of the fringe; a summary of this image analysis process is shown in Figure 2.7. The wavelength of the fringe can then be determined with knowledge of the applied optical magnification and the refractive index of the medium. Finally, the absolute surface separation D can be calculated from the wavelength of the p fringe $\lambda_p(D)$ relative to the calibration values, by applying Equation 2.1:

$$\tan\left(k\mu_{\text{medium}}D\right) = \frac{2\bar{\mu}\sin\theta}{(1+\bar{\mu}^2)\cos\theta \pm (\bar{\mu}^2-1)} \tag{2.1}$$

where k is the wavenumber of the light ($k = 2\pi/\lambda$),

$$\bar{\mu} = \frac{\mu_{\text{mica}}}{\mu_{\text{medium}}}, \quad \theta = \frac{p\pi(\lambda_p(D) - \lambda_p(D=0))}{\lambda_p(D=0)}, \quad p = \frac{\lambda_{p-1}(D=0)}{\lambda_{p-1}(D=0) - \lambda_p(D=0)},$$

μ_i is the refractive index of layer i and $\pm$ refers to the odd and even order fringes, respectively. Equation 2.1 is accurate at surface separations smaller than 400 nm.[85]

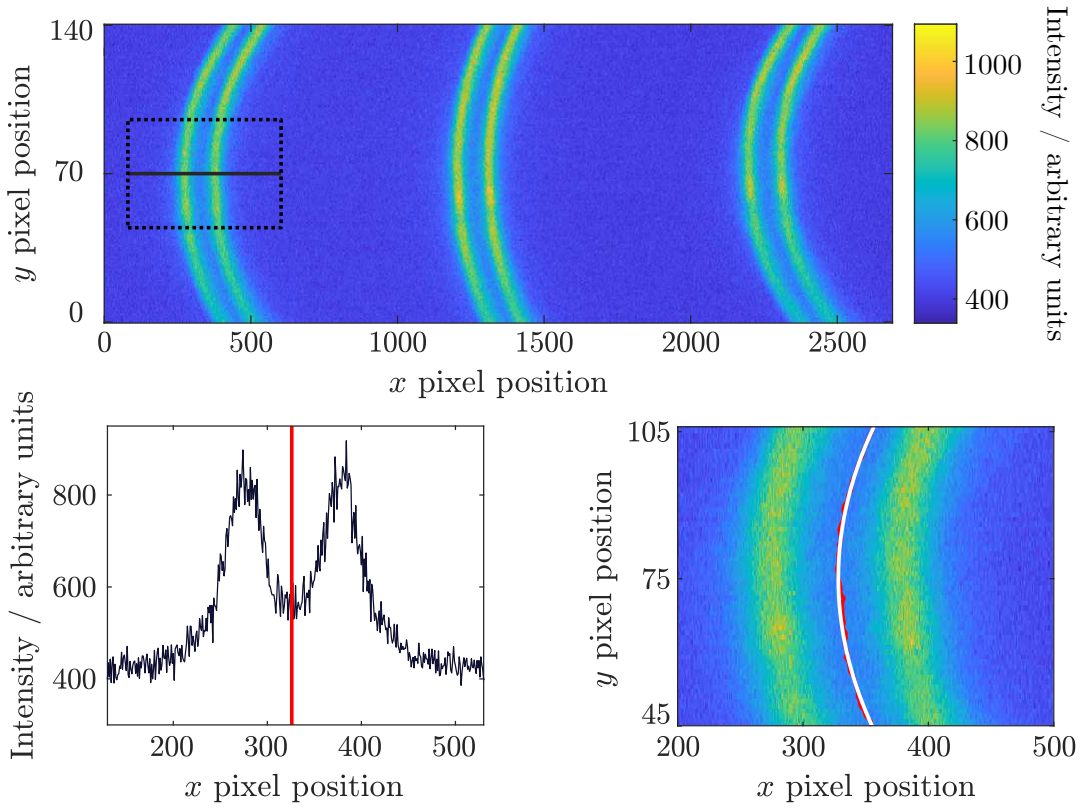

Figure 2.7: Summary of image analysis. Top: the FECO recorded during a measurement. The dotted black box shows the region in which the p fringe is tracked, and the solid black line shows that across which the intensity of the fringes is monitored in the bottom left panel. Bottom left: the black plot shows the intensity of the FECO along the black line described in the top panel. The vertical red line shows the x pixel position calculated to be the centre-of-mass of the doublet. Bottom right: the calculated centre-of-mass as a function of y pixel position is plotted in red, which is fitted to a parabola shown in the white line and the apex of which is $\lambda_p(D)$.

2.1.5 | Measuring Interaction Profiles

Before commencing a measurement of an interaction profile, the surface separation is adjusted to an initial distance D_0 of several hundreds of nanometres, typically $\sim$ 300 nm, where it is assumed that no forces are acting between the surfaces. Starting at a time t_0, the surfaces are then approached at a constant velocity v using either the fine motor or piezo, causing the surface separation to decrease at a linear rate $D(t) = D_0 - vt$ whilst no forces act between the surfaces. In most measurements in this work, the velocities used have an order of magnitude $\sim$ 1 nm s^{-1}.

At distances where the surfaces exert a force on one another, there is an additional contribution to the surface separation owing to the deflection of the leaf spring upon which the lower lens is mounted $\delta(t)$. This term is the difference between the measured surface separation $D(t)$ and that predicted from an extrapolated, pure linear approach, as shown in Equation 2.2.

$$\delta(t) = D(t) - [D_0 - vt]. \tag{2.2}$$

The normal force acting between the surfaces F_N is therefore given by Equation 2.3:

$$F_N(t) = k_N\delta(t) = k_N[D(t) - D_0 + vt]. \tag{2.3}$$

where k_N is the known spring constant of the leaf springs.

Derjaguin Approximation

Finally, as we discussed in Chapter 1, whilst it is most practical to measure the interaction forces between macroscopic surfaces, it is energies that are most useful when considering interactions between molecules and small particles, and for theoretically predicting the interaction between parallel plates. The Derjaguin approximation allows for the conversion from the measured force F_N between two curved surfaces

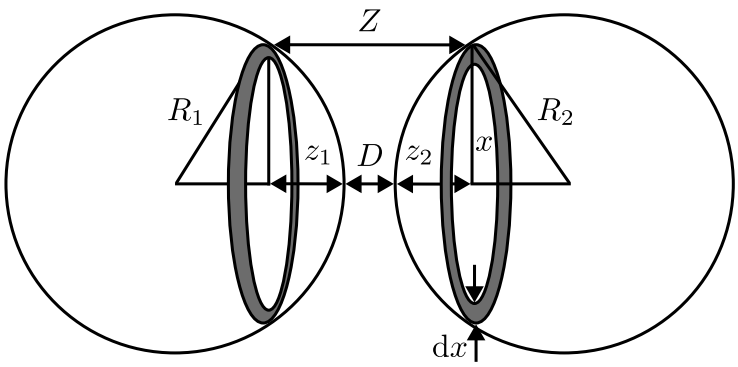

Figure 2.8: Geometry of two spheres of radius R_1 and R_2 interacting, separated by distance D. The Derjaguin approximation applies when $R_1, R_2 \gg D$.

to the interaction free energy per unit area between two parallel plates $W^{||}$.[86]

The geometry for the general case of two large spheres of radii R_1 and R_2 at a small distance D apart is depicted in Figure 2.8. Providing that $R_1, R_2 \gg D$, the force between the spheres can be obtained by integrating the force over small concentric circular regions of area $2\pi x\,\mathrm{d}x$ on either surface. These regions are assumed to be locally flat and at a separation Z given by Equation 2.4.

$$Z = D + z_1 + z_2 \tag{2.4}$$

In the z direction, the total force acting between the two spheres is given by Equation 2.5:

$$F_{\mathrm{N}}(D) = \int_{Z=D}^{Z=\infty} 2\pi x\,\mathrm{d}x\, f_{\mathrm{N}}(Z) \tag{2.5}$$

where $f_{\mathrm{N}}(Z)$ is the normal force per unit area between two flat surfaces. The Chord Theorem yields the relation shown in Equation 2.6.

$$x^2 \approx 2R_1 z_1 = 2R_2 z_2 \tag{2.6}$$

Substituting this relation into Equation 2.4 yields Equation 2.7, and considering the derivative of this gives Equation 2.8.

$$Z = D + \frac{x^2}{2}\left(\frac{1}{R_1} + \frac{1}{R_2}\right) \tag{2.7}$$

$$\mathrm{d}Z = \left(\frac{1}{R_1} + \frac{1}{R_2}\right) x\,\mathrm{d}x \tag{2.8}$$

Finally, substituting Equation 2.8 into Equation 2.5 yields Equation 2.9.

$$F_{\mathrm{N}}(D) = \int_D^\infty 2\pi\left(\frac{R_1 R_2}{R_1 + R_2}\right) f(Z)\,\mathrm{d}Z = 2\pi\left(\frac{R_1 R_2}{R_1 + R_2}\right) W^{\mathrm{II}}(D) \tag{2.9}$$

In the limiting case of a sphere of radius R in contact with a flat surface ($R_1 \gg R_2$), the free energy of interaction becomes the result shown in Equation 2.10. It can be shown that this result is equivalent for that of two cylinders of equal radii crossed at right angles - the geometry used in our force measurements - and thus this result will be used throughout this thesis.

$$W^{\mathrm{II}}(D) = \frac{F_{\mathrm{N}}(D)}{2\pi R} \tag{2.10}$$

Radius of Curvature Calculation

As evident from Equation 2.10, we require a value for the radius of curvature of the surface R in order to calculate $W^{\mathrm{II}}(D)$. Whilst the glass lenses used in these measurements are manufactured with a radius of curvature $R \sim 1$ cm, local deviations can occur due to variations in the thickness of glue at different points of contact between the two lenses, and therefore the radius must be calculated by other means. The FECO recorded during a measurement (Figure 2.6) provide a method for calculating this value, since the parabola that is fitted to the p fringe is an approximation to a circle of radius R. This can be seen in the binomial expansion of the equation of a circle at small displacements around $x = 0$, as shown in Equation 2.11. Such an approximation is valid since the displacement away from the apex of the fringe at which we perform this calculation ($\sim$ µm) are much smaller than the radius of

curvature of the lens ($\sim$ cm).

$$y = \pm\sqrt{R^2 - x^2} \approx \pm\left(R - \frac{x^2}{2R}\right) \tag{2.11}$$

The Final Interaction Profile

The measurement of interaction free energy from the approach of the surfaces until contact yields a partial contribution to the overall profile. Additional features, including adhesive forces, can be measured by retracting the surfaces away from contact and analysing the response in a similar manner. If an oscillatory structural force is present and the approach free energy versus distance profile exhibits a series of repulsive steps during the approach, the retraction of the surfaces and measurement of their associated minima can be repeated for each of the steps, thus building a more complete picture of the total interaction profile from these partial measurements. This method of measuring the deflection of the leaf springs and determining the normal interactions from both the approach and retraction of the surfaces is illustrated through an example measurement in Figure 2.9.

Within this experiment, it is impossible to fully measure the interaction free energy profile of a liquid. This is owing to an important feature of the measurement technique: the mechanical spring instability.[64] As the surfaces approach one another, the interaction is balanced by the restoring force of the spring whilst the condition that the gradient of the energy with distance $\partial W^{\parallel}/\partial D < k_{\mathrm{N}}$ holds. If instead the opposing condition $\partial W^{\parallel}/\partial D \geq k_{\mathrm{N}}$ is satisfied, there is a spring instability and the surfaces will jump together or apart until the initial condition is satisfied, yielding those regions inaccessible to measurement. A schematic illustrating this phenomenon is shown in Figure 2.10.

Since this measurement technique involves the dynamic motion of surfaces confining a fluid, it is worth briefly considering the magnitude of hydrodynamic forces during measurements. Between an approaching sphere and a flat surface (equivalent

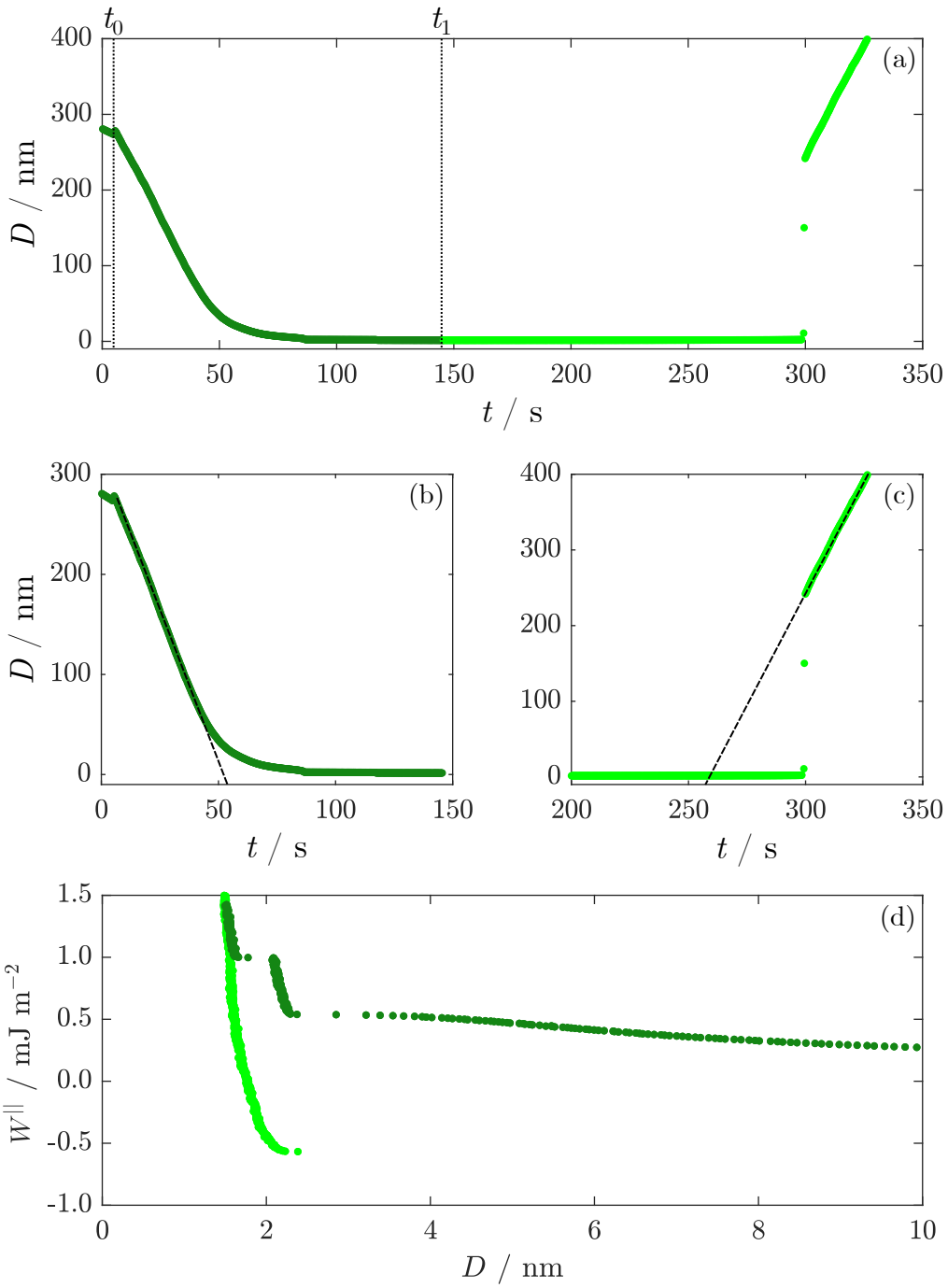

Figure 2.9: Summary of the analysis required to calculate the free energy of interaction $W^{\parallel}$ as a function of distance D. (a) Surface separation D as a function of the time elapsed since the start of the run t. The motors are switched on at time t_0, approaching the surfaces. The direction of the motors is reversed at time t_1, retracting the surfaces. (b) The approach is fitted with a baseline in the region of linear approach, where it is assumed that no forces are acting. In this example, the baseline is fitted between 200 nm and 100 nm; the approach velocity is 6.23 nm s^{-1}. (c) The retraction is fitted with a baseline in the region of linear retraction, after the surfaces have jumped apart. In this example, the baseline is fitted between 260 and 400 nm; the retraction velocity is 5.84 nm s^{-1}. (d) The completed interaction potential profile as a function of distance is calculated using Equations 2.3 and 2.10.

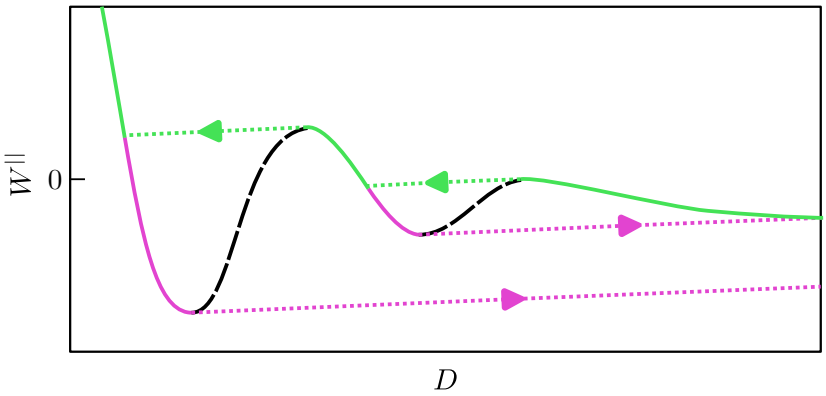

Figure 2.10: Schematic for the free energy of interaction between parallel plates $W^{||}$ versus surface separation D, illustrating the components of the full oscillatory interaction that are measured due to the mechanical spring instability. On approach of the surfaces (green), the surfaces 'jump in' when they reach an unstable region at the point where the condition $\partial W^{||}/\partial D \geq k_{\mathrm{N}}$ is satisfied. On retraction of the surfaces, they remain in the adhesive minimum until they 'jump out' to larger distances. Data recorded during these jumps do not represent system equilibrium, and are shown here as dotted lines. Only one minimum can be explored during a single, combined approach and retraction; multiple approaches and retractions are required to explore as much of the interaction profile as possible. The black dashed lines indicate the regions of the interaction profile that cannot be measured with the surface force balance.

to the crossed-cylinder geometry), the contribution to the measured interaction due to hydrodynamic forces $W_{\mathrm{H}}^{||}$, *i.e.* the energy dissipated during the motion due to viscous interactions, can be estimated by Equation 2.12:[87]

$$W_{\mathrm{H}}^{||} = \frac{3\eta R v}{D} \tag{2.12}$$

where η is the viscosity of the fluid, R is the radius of the sphere, v is the approach velocity and D is the film thickness. Considering appropriate values for these parameters ($\eta \approx 1$ mPa s, $R \approx 10^{-2}$ m, $v \approx 1$ nm s^{-1}, $D \approx 10$ nm), the contribution to the interaction free energy, $W_{\mathrm{H}}^{||} \approx 10^{-3}$ mJ m^{-2}; *i.e.*, is significantly smaller than energies measured in this work and can therefore be safely ignored in the analysis of interaction energy profiles.

2.1.6 | Experimental Error Analysis

For each data point in an interaction profile, there is a random error associated with the measured surface separation D. This error arises as a result of uncertainty in the fringe tracking procedure discussed in Section 2.1.4. The magnitude of this uncertainty depends on the mica thickness, with thicker mica resulting in a larger uncertainty since more fringes occur in the wavelength region of interest, but is usually small, typically ~ 0.1 nm - 0.2 nm. This source of random error also contributes to an error in the interaction energy $W^{||}$, since it is calculated from the deflection of the normal spring. This uncertainty has a magnitude ~ 0.01 mJ m^{-2}. Additionally, there is a contribution to a systematic error in the reported interaction energies arising from uncertainty in the values of the spring constant k_{N} and the radius of curvature R, both of which are used to calculate the interaction energy. The error in each is $\sim 5\%$ and is constant throughout an individual measurement.

There is also variation between individual measurements runs in an SFB experiment, as illustrated in Figure 2.11. Error in the absolute surface separation arises due to shifts in optical alignment. Where runs are performed on the same measurement spot, as is the case in Figure 2.11, these shifts are relatively small and variation in the absolute distance is typically ~ 0.2 - 0.4 nm. When comparing between measurement runs on different measurement spots, these shifts can be greater and can result in a larger distance variation of around ~ 0.5 nm.

A source of variation between measurements in the interaction energies arises from the procedure for fitting the zero-interaction baseline. These baselines are fitted in the region where the interaction between the surfaces are negligible, but factors such as external vibrations or thermal fluctuations, though they are minimised, can result in an offset to the reported interaction energy. Between measurements, variation in $W^{||}$ is ~ 0.1 mJ m^{-2}, though this value can be greater in the high $W^{||}$ regions at smaller surface separations.

Overall, unless specifically mentioned, no significant differences appear between

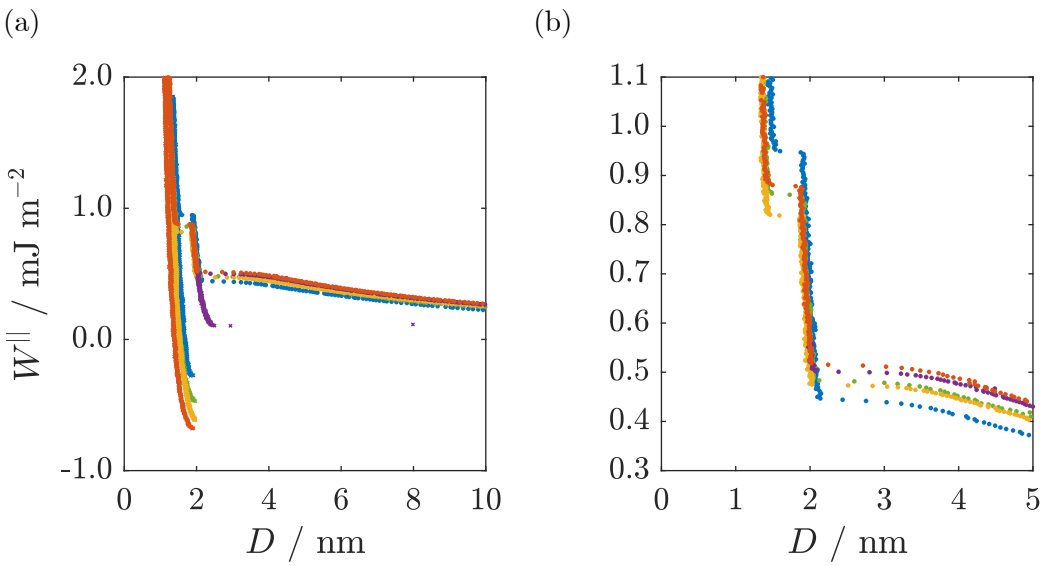

Figure 2.11: Scatter between runs during a typical surface forces balance measurement across an aqueous solution, performed on the same microscopic contact spot. (a) A series of five approach and retractions runs performed during a single experiment. (b) A close-up view of the set of five approaches.

individual runs in a particular experiment. These measurements exhibit limited dependence on equilibration time (between adjacent runs), time after introducing the liquid between the mica surfaces or the specific microscopic contact spot between the two crossed cylinders. Between runs, there are small variations in the energies at which jumps due to a spring instability occur, in addition to the magnitude of long range interactions. On the other hand, the changes in distance over which features occur (*e.g.* molecular layer thicknesses) and screening lengths are more reproducible. In this work, no averaging of multiple measurement runs is performed as this would lead to a 'smearing' of the subtle features captured in individual runs. Instead, a single run that is representative of a series of repeat measurements is usually presented.

2.2 | Total Scattering Measurements

As disordered materials, liquids do not display long-range order between atoms. However, there can exist local correlations - or short-range order - between atoms due to intra- or intermolecular interactions. In order to probe these local correlations

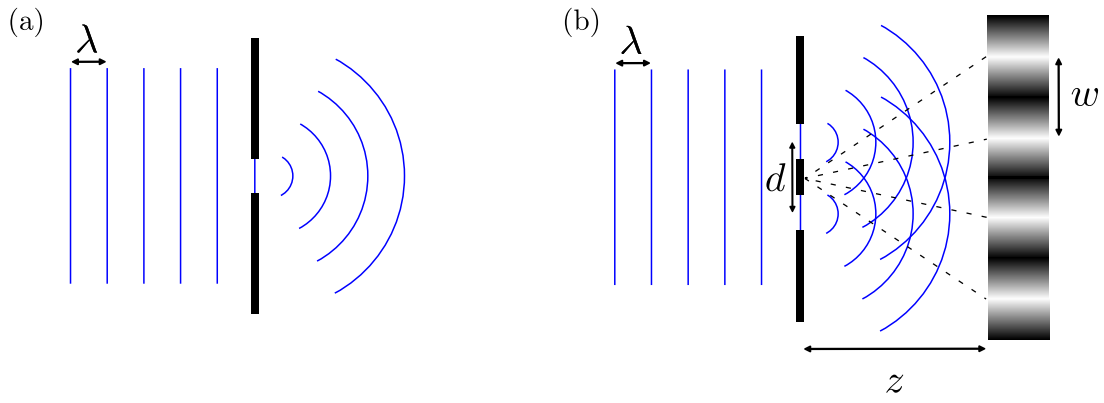

Figure 2.12: Diffraction of a wave of wavelength λ through (a) a single slit and (b) two slits separated by distance d. In the case of the double slit, interference of the diffracted waves results in a diffraction pattern of alternating bright and dark bands of intensity separated by w when observed on a screen at distance z from the slits.

and thus gain an insight into the bulk structure of a liquid, one can perform total scattering measurements using either, or both, of neutrons and X-rays. This section will begin with an overview of diffraction theory, followed by a discussion of the coherent elastic neutron scattering technique employed at the ISIS Neutron and Muon Source, a pulsed source at the Rutherford Appleton Laboratory of the Science and Technology Facilities Council, where all of the measurements of bulk structure in this work were performed. This section will also contain a discussion of the use of X-ray total scattering as a complimentary technique to neutron scattering.

2.2.1 | Diffraction Theory

Diffraction is the phenomenon in which a wave spreads out as it passes an obstacle or through an aperture. Both the wavelength of the travelling wave and the size of the aperture influence the extent to which a wave will diffract. Effective diffraction occurs when the wavelength is of a similar order of magnitude to the size of the aperture: a schematic of this diffraction of a wave is shown in Figure 2.12.

In the case where a wave passes through two slits which are separated by a comparable distance to the wavelength, the diffracted waves emergent from the two slits interfere with one another. This results in a characteristic diffraction pattern if

the intensity of the resulting wave is recorded away from the slits, with alternating bands of high and low intensity emerging from constructive and destructive interference, respectively, of the waves. This effect due to the wave-like nature of light was first evidenced by Thomas Young in 1801.[88] The spacing between the bands of high intensity w is related to the distance between the slits d and the wavelength of the light λ by Equation 2.13:

$$w = \frac{z\lambda}{d} \tag{2.13}$$

where z is distance away from the slits where the diffraction pattern is measured, and with the condition $z \gg d$. This experiment illustrates the simplest example of using the diffraction of waves to extract information about structural features, and has been the catalyst for myriad discoveries in scattering measurements for structural determination.

In order to determine the arrangement of atoms in matter, one must use a source of radiation of wavelength similar to interatomic separations, which is typically of Ångstrom order in condensed matter (1 Å = 10^{-10} m). If using radiation from the electromagnetic spectrum, X-rays would therefore typically be employed for such a diffraction study. However, as we will discuss later, other sources of radiation can be used for structural determination, including neutrons.

To understand how a scattering experiment performed on a liquid can be used to determine structural correlations between atoms within such liquid, it is useful to first consider diffraction from a general object. Only a simple discussion is required for the scope of this thesis; more detailed derivations to those given here can be found in the literature.[89] In this description, we will not specify the type of radiation being used, though we will employ the nomenclature used by the neutron scattering community as this is the dominant technique used for bulk structural characterisation in this thesis.

Figure 2.13 shows a general object, upon which a source of radiation of wave-

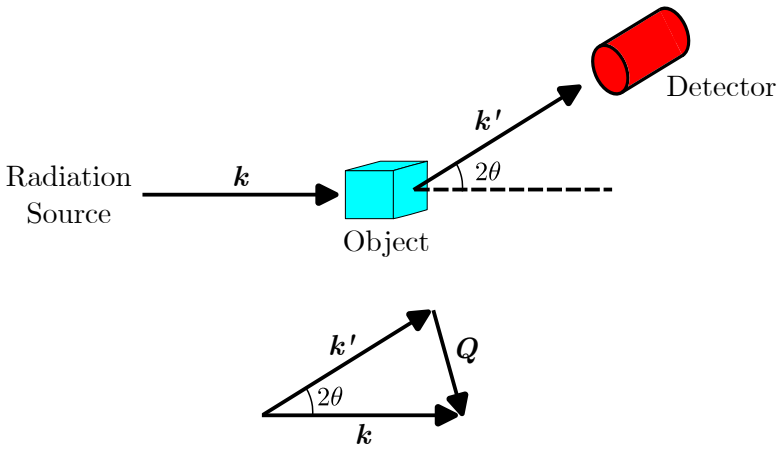

Figure 2.13: Schematic illustrating the geometry of an elastic scattering experiment. Radiation incident to the object of an initial wave vector $\boldsymbol{k}$ is scattered by an angle 2θ to a wave vector $\boldsymbol{k}$'. The scattering vector $\boldsymbol{Q}$ is the difference between the incident and scattered wave vectors.

length λ is incident. In addition to the wavelength of this radiation, it is also useful to consider its wave vector $\boldsymbol{k}$, a vector that is perpendicular to the wavefront and has a magnitude given by Equation 2.14.

$$|\boldsymbol{k}| = \frac{2\pi}{\lambda} \tag{2.14}$$

An elastic scattering event - in which the energy of the radiation is conserved - will result in this incident wave being re-emitted at all angles around the object. At an angle 2θ, the radiation will be emitted with a wave vector $\boldsymbol{k}$' of equal magnitude to the incident wave vector. A scattering vector $\boldsymbol{Q}$ can be defined as the difference between the scattered and incident wave vectors, as described by Equation 2.15.

$$\boldsymbol{Q} = \boldsymbol{k}' - \boldsymbol{k} \tag{2.15}$$

In three-dimensions, one can measure the flux of the scattered radiation at each angle around the object. The differential cross section $d\sigma/d\Omega$ is a measure of this, and is defined as the probability of detecting a scattering event at a given solid angle. This term is defined mathematically in Equation 2.16:

$$\frac{d\sigma}{d\Omega} = \frac{R}{N\Phi d\Omega} \tag{2.16}$$

where R is the rate of detecting a scattering event at a given solid angle Ω, Φ is the incident radiation flux, and N is the number of scattering centres in the object, by which the differential cross section is normalised in some definitions. The differential cross section has dimensions of area; the units of which are normally reported in barns (1 barn = 10^{-28} m^2).

Further derivation can be performed to show that the differential cross section can be separated into two contributions: self-scattering and cross-scattering. The self-scattering term comprises scattering occurring from individual nuclei and is independent of the scattering vector $\boldsymbol{Q}$, dependent only on the composition of the sample and thus contains no information regarding the atomic structure of the object. In contrast, the cross-scattering term does contain information regarding structural correlations; it is the weighted sum of all partial structure factors S_{ij} describing correlations between the i^{th} and j^{th} atoms in the sample. This separation of the two contributions to the differential cross section is shown in Equation 2.17.

$$\left(\frac{d\sigma}{d\Omega}\right) = \left(\frac{d\sigma}{d\Omega}\right)_{\text{self}} + \left(\frac{d\sigma}{d\Omega}\right)_{\text{cross}} = \sum_i c_i b_i^2 + \sum_i \sum_{i \leq j} (2 - \delta_{ij}) c_i c_j b_i b_j S_{ij}(Q) \tag{2.17}$$

where c_i and b_i are the atomic fraction and neutron bound coherent scattering length of the i^{th} atom type, respectively; and δ_{ij} is the Kronecker delta.

The cross-scattering contribution is related to an important quantity in the study of total scattering: the total structure factor, given in Equation 2.18.

$$F(Q) = \sum_i \sum_{i \leq j} (2 - \delta_{ij}) c_i c_j b_i b_j \left[S_{ij}(Q) - 1\right] \tag{2.18}$$

Each partial structure factor S_{ij} for atoms i and j is related the Fourier transform of the pair distribution function g_{ij} for the same pair of atoms, as shown in Equation

2.19.

$$S_{ij}(Q) - 1 = 4\pi\rho \int_0^\infty r^2 \left[g_{ij}(r) - 1\right] \frac{\sin Qr}{Qr} dr \tag{2.19}$$

In Equations 2.17 - 2.19, we used the variable b as the neutron bound coherent scattering length, a term that is nucleus-dependent, and governs the probability that a neutron is scattered by any such nucleus. The value of b is determined by the nature of the interaction between a neutron and a nucleus, and varies not only between atoms of different elements, but also between different isotopes of the same element. This characteristic of neutron scattering is particularly advantageous for the study of aqueous samples, which we will return to later in this thesis. An analogous term exists in the context of X-ray scattering describing the strength of the interactions between a scattering atom and an X-ray. This is known as the atomic form factor f, and is proportional to the atomic number Z of the scattering atom.

In the next two sections, we will further consider the interactions between neutrons or X-rays and a scattering atom, along with other experimental details such as their generation and detection after a scattering event.

2.2.2 | Neutron Total Scattering

First observed in 1932 by James Chadwick, a neutron is a subatomic particle which, along with protons, can be found in the nucleus of all atoms excluding protium.[90,91] Neutrons have no electric charge and a mass slightly greater than that of a proton; these and other properties of neutrons, compared with other subatomic particles, are displayed in Table 2.1.

Uncharged and much heavier than an electron, a free neutron incident on an atom is largely unaffected by the electron density that surrounds the atomic nucleus and is therefore deeply penetrating. The dominant mechanism for the scattering of a free neutron by an atom is instead through an interaction with the atomic nucleus,

Table 2.1: Properties of three subatomic particles: the neutron, the proton and the electron.

	Neutron	Proton	Electron
Mass m / kg	1.675×10^{-27}	1.673×10^{-27}	9.109×10^{-31}
Charge q / e	0	+1	-1
Spin	$\frac{1}{2}$	$\frac{1}{2}$	$\frac{1}{2}$

mediated by the strong nuclear force. An exception to this statement exists in the presence of an unpaired electron, in which case there is a significant scattering contribution from the interaction of the magnetic moments of this electron and the free neutron.

Though traditionally thought of as a particle, a neutron can also be considered to exhibit wave-like properties and the framework for diffraction described previously can therefore also be applied. This property is captured in the more general concept of wave-particle duality, first evidenced by Louis de Broglie in his work showing that an electron around a nucleus could be considered as a standing wave of a wavelength λ that is inversely proportional to the momentum p of the electron,[92,93] with the Planck constant h as the proportionality constant. This famous relationship is reproduced in Equation 2.20.

$$\lambda = \frac{h}{p} \tag{2.20}$$

Since then, many experiments with neutrons have reproduced results predicted by wave-like behaviour, including diffraction measurements through a slit.[94] It is clear therefore, that if the velocity of a neutron is such that its wavelength is of a magnitude similar to that of atomic separations, neutrons can be employed in diffraction studies in order to reveal information regarding atomic arrangement in matter.

There exist two principle ways by which a reliable source of neutrons can be generated for a diffraction experiment: firstly, by a nuclear reactor or secondly, by

a spallation process. In the former, neutron-induced nuclear fission takes place in a reactor, using a heavy element as a fuel source such as uranium or plutonium typically, or occasionally thorium or polonium. In this process, the nuclei captures a neutron and decays into two lighter nuclei, releasing heat and free neutrons in the process. The fission reaction will be self-sustaining if one emitted neutron from this process goes on to initiate a second decay event. Therefore, in order to prevent this nuclear reaction from running out of control and becoming supercritical, the remaining neutrons must be removed from the reaction environment. This is usually effected by making use of moderators, typically materials that are chosen to slow down neutrons and are typically made of light or heavy water, or graphite. In this source, reflectors are also used to direct the generated neutrons towards the target of interest, thus optimising the neutron flux of the beam. Beryllium is the most common material from which these reflectors are made.

In contrast, a spallation source produces neutrons through accelerating bunches of protons in a particle accelerator. These are directed towards a heavy metal target - normally made of tantalum or tungsten - producing excited nuclear states which subsequently decay with the release of subatomic particles, including neutrons. As with the nuclear reactor, moderator and reflector materials are employed to optimise the flux of the beam at the desired target. Spallation sources possess the main benefit over reactor sources that they can be easily switched off and there is no nuclear fuel produced. A further benefit is there is no need for a monochromator at a pulsed neutron source, potentially yielding a higher proportion of generated neutrons that are used to measure useful data.

All of the neutron total scattering data presented in this work was collected at the ISIS Neutron and Muon Source at the Rutherford Appleton Laboratory in Harwell, UK. This facility generates neutrons using a spallation source, delivering a proton beam towards two neutron-producing, tungsten targets.[95] The production of the proton beam is achieved by initially performing an electrical discharge inside a

mixture of hydrogen gas and a small amount of caesium vapour in order to generate hydride ions, H^-. These hydride ions are extracted from the ion source and the beam is focussed, bunched and accelerated using a radio-frequency quadrupole (RFQ). The beam next passes into a linear particle accelerator - a LINAC - in which intense radio frequency (RF) fields accelerate the beam across four accelerator tanks up to an energy of 70 MeV. From here, the hydride ions pass through a very thin carbon stripping foil which removes two electrons and converts the ions into a proton. This proton beam then passes into a synchrotron of radius 26 m, accelerating the 70 MeV beam to an energy of 800 MeV which is made up of ten sections, or 'superperiods', through each of which the beam is bent through an angle of 36°. Each superperiod comprises a dipole magnet and three quadrupole magnets, and the accelerating voltage is provided by ten RF cavities. In total, it takes approximately 8000 turns of the synchrotron for the beam to accelerate to 800 MeV, at which point the protons are moving at 84% of the speed of light. In order to eject the two bunches of protons orbiting the synchrotron, a high-speed magnet can be switched in order to deflect the bunches onto the two extracted proton beam lines leading to the two target stations, TS1 and TS2. In both target stations, the proton bunches are incident on tantalum-clad tungsten targets, generating neutrons as discussed previously. Both targets are surrounded by a beryllium reflectors and moderators: four in TS1 (two water, one liquid methane and one liquid hydrogen), and two in TS2 (one liquid hydrogen and one solid methane).

For the results presented in Chapter 5, all measurements were performed using the Near and InterMediate Range Order Diffractometer (NIMROD), one of the instruments that receive neutrons from TS2.[96] This instrument makes use of a broad spectral range of neutrons, typically of wavelengths between 0.04 to greater than 12 Å, allowing the collection of scattering data across a wide Q range, from 0.02 to 50.0 $Å^{-1}$. This corresponds to correlations at distances in a range between 0.15 to over 300 Å.

During a measurement, the samples of interest are contained within the instrument in a flat plate cell made from a titanium and zirconium alloy (TiZr), at a molar ratio of 7.16:3.438. This ratio is chosen such that the weighted average of the coherent scattering length b for the alloy is zero and thus the sample container is a null scatterer, minimising any scattering signal arising from the sample container.[97]

The wide scattering angle range possible with the NIMROD instrument is made possible by the 1098 detector elements covering wide angles from 3.5 to 40° in addition to a further 756 elements that cover scattering angles from 0.5 to 2.2°. Each detector comprises a scintillating element, formed of alternating layers of glass and a matrix of Ag-doped ZnS in which ^{6}LiF is dispersed. This detector technology employs a popular reaction for the detection of slow neutrons, occurring when a ^{6}Li nucleus absorbs a neutron and subsequently decays, as shown in Equation 2.21.[98]

$$^{6}\mathrm{Li} + \mathrm{n} \longrightarrow {}^{3}\mathrm{H} + {}^{4}\mathrm{He} \tag{2.21}$$

The energy generated from this reaction is absorbed by the ZnS(Ag) scintillator and subsequently a photon is emitted; photomultipliers are used to detect these scintillation events.

2.2.3 | X-ray Total Scattering

Being of wavelength similar to that of interatomic separation, X-rays are frequently chosen in diffraction studies to determine the arrangement of atoms in materials. X-rays are strongly interacting and are readily absorbed by atoms, thus acting as an effective atomic scatterer; and in contrast to neutrons, X-rays are scattered by the electron density that surround atoms.

In general, X-rays are produced from two types of sources: a laboratory source or a synchrotron. In the former, a high energy electron beam is incident on a metal target, producing emergent X-rays; in the latter, a circulating beam of electrons and relativistic speeds generates electromagnetic radiation, predominantly in the X-ray

region. For the measurements in this work, we employ a diffractometer (Malvern Panalytical Empyrean), a laboratory source which produces X-rays that can study samples mounted in silica capillary tubes within the diffractometer.

Numerous methods exist for the detection of X-rays; only a brief overview will be given here. Most detectors comprise a material in which scintillation events are initiated after excitation by X-ray photons, combined with a photomultiplier tube which allows for the detection of these scintillation events. In order to be an effective X-ray detector for diffraction studies of liquids and other disordered materials, it is important that the detector response to X-ray flux is both linear and uniform.

2.2.4 | Data Correction

In order to use the measured scattering data to perform structural determination of the system, one must only use data arising from coherent, elastic scattering. However, the neutron and X-ray detectors used in experiments record radiation indiscriminately, detecting all neutrons or X-ray photons including those that are scattered by incoherent and inelastic scattering events. Furthermore, contributions to the overall scattering pattern that have arisen from multiple scattering events, as well as any scattering arising from the sample container or self scattering, must also be discarded. In this work, we use the methods developed by Soper in order to perform such a post-acquisition analysis, using the GudrunN and GudrunX packages for neutron and X-ray scattering data, respectively. These packages uses complex algorithms which will not be described in their full detail here; more details can be found in the technical report by Soper.[99]

To correct the experimental total structure factor obtained from neutron scattering, one must also collect scattering data from the background (recorded with neither the sample or container present), the container (recorded without the sample present) and a vanadium standard, all of which should ideally be recorded using the same beam conditions including the aperture and detector positions. The Gu-

drunN algorithm seeks to correct the raw data by: identifying and eliminating data from untrustworthy detectors; correcting for attenuation and multiple scattering; correcting for the intrinsic deadtime of the detectors; and finally, normalising the data to the calibration measurement performed on the vanadium standard. The vanadium standard measurement is chosen owing to the fact that its atom has a small coherent scattering length for neutrons; any scattering from Bragg reflections, therefore, is weak compared to the isotropic, single atom scattering.[100] The large mass of the vanadium atom relative to the neutron also means that inelasticity effects will be small, and its attenuation properties are also well understood.

Similarly for X-ray total scattering, one must collect background measurements both with and without the empty silica capillary, on top of the measurement performed on the sample. The GudrunX package calculates a structure factor from these three sets of raw data, as well as correcting for effective density, absorption, multiple scattering, Compton scattering (a form of inelastic scattering whereby electrons recoil under the impact of an incident X-ray)[101] and *bremsstrahlung* scattering (background radiation caused by incident electrons being decelerated in the anode material).[102]

2.2.5 | Data Modelling

Now that we have the corrected total structure factor for our experimental system, we turn to the elucidation of its structure. For a system containing J distinct atom types, there are $N = J(J+1)/2$ distinct atomic site-site correlations to be determined in order to fully describe its structure. However, with only one measurement of the structure factor for the system it is impossible to extract an unambiguous set of these correlation functions between components. In order to overcome this challenge, we can exploit differences between the coherent scattering lengths of isotopes of a given element. With the assumption that isotopic substitution does not significantly affect the structure of our system, we can prepare samples of identical

composition with multiple isotopic contrasts, thus altering the relative weights of the contributions to the total structure factor from individual correlations (Equation 2.18).

Theoretically, if N total structure factors $F(Q)$ could be measured for systems of differing isotopic composition, these could be inverted using a three-dimensional Fourier transform to produce a complete set of the distinct correlations. However, in practice only some atoms in the system have suitable isotopes for substitution and this direct method for structural determination is not accessible. One can instead turn to an alternative powerful technique, empirical potential structure refinement (EPSR): a reverse Monte Carlo simulation technique which can be used to analyse experimental diffraction data.[103]

The EPSR technique initially considers a simple reference potential to describe a system matching the experimental composition and density. The potential contains parameters to account for each atom type present in the sample. In its simplest form, an intermolecular reference potential between two atoms, i and j, is based on a sum of Lennard-Jones and Coulombic contributions, as described in Equation 2.22.

$$U_{\text{inter}} = 4\epsilon_{ij}\left[\left(\frac{\sigma_{ij}}{r_{ij}}\right)^{12} - \left(\frac{\sigma_{ij}}{r_{ij}}\right)^{6}\right] + \frac{q_i q_j}{4\pi\epsilon_0 r_{ij}} \tag{2.22}$$

Additional terms can be included in a reference potential, particularly in order to describe intramolecular interactions, which commonly include classical, harmonic terms for bonds, angles and torsions.

The system is equilibrated using this reference potential, from which theoretical scattering data can be generated and compared to the experimental data. Using the calculated difference between the predicted and experimental data, the potential of the system is refined by applying an additional interatomic potential - an empirical potential - which drives the simulation towards greater agreement with all of the measured structure factors for all of the isotopic contrasts. These empirical

potentials do not derive from any physical basis, and instead comprise a series of appropriate functions which are iteratively refined until a suitable degree of agreement is reached between the simulated structure factors and those obtained from experiment. Once the refinement has taken place, the simulation can be interrogated to reveal specific structural features, such as radial distance or angular distributions between certain chemical moieties in the system.

As a tool, the EPSR package has been vital in the scattering analysis and structural characterisation across a plethora of disordered materials, including simple liquids and mixtures,[104] deep eutectic solvents,[105] ionic liquids[106] and glasses.[107] However, there do exist some limitations to the analysis and system capability of this package, such as the ability to compute suitably large simulation boxes and an increased complexity of molecular systems. In this work we choose to use the Dissolve package, a second generation total scattering analysis tool which was designed in response to these needs.[80] This package aims to be consistent with EPSR, utilising a similar Monte Carlo methodology, but aims also to overcome some of the demands from the disordered materials community including the aforementioned simulation size and molecular complexity limitations to EPSR. As well as incorporating enhanced computational power and algorithmic efficiency - allowing boxes containing up to 3×10^6 atoms to be simulated - Dissolve also features a molecular dynamics (MD) simulation component on top of the Monte Carlo component present in EPSR, therefore facilitating the study of larger, more complex chemical systems. In this work we use Dissolve v1.6.0 to perform the analysis of our scattering data. Figure 2.14 shows a flowchart of the procedure used in Dissolve to generate a simulated structure that resembles the experimental data using the concepts described in this section.

Dissolve also provides several analysis routines which can be used to interrogate various structural properties of the refined structure, including the calculation of radial distribution functions, coordination number distributions, angular distributions

and spatial density functions. These are calculated over a trajectory of 10,000 simulation snapshots which all have the same level of global fit to the experimental data. By calculating these functions over all relevant atomic sites in each snapshot, and over all of the snapshots in this trajectory, reliable statistics can be generated for the aforementioned structural analyses. This same trajectory can also be exported from Dissolve, allowing for custom analysis of the same structural data to be performed; a custom cluster analysis routine was used in this work, which is discussed further in Chapter 5.

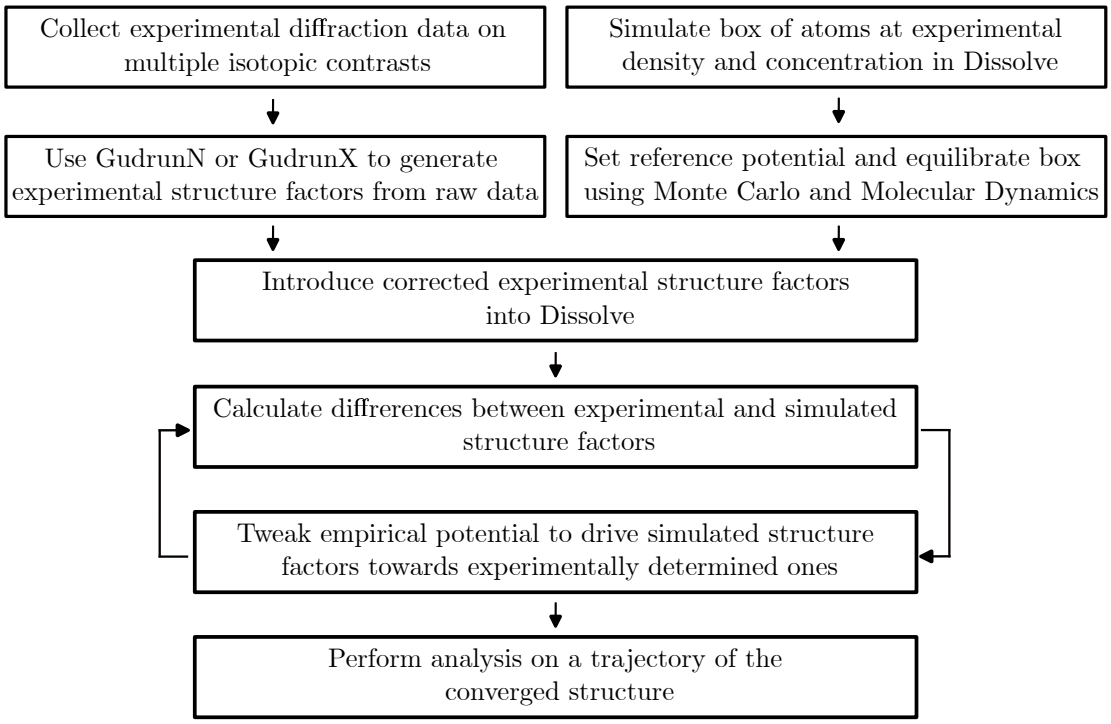

Figure 2.14: Flowchart illustrating the procedure required to analyse neutron and X-ray total scattering data, starting from experimental diffraction data and ending with a simulated structure which matches the experimental data, upon which further analysis routines can be performed.

2.3 | Additional Measurements

As part of the analysis for the primary measurement techniques outlined in the previous sections, determining specific physical properties of the studied liquid systems using some supporting measurements is necessary. This includes measurement of a

sample's refractive index for analysis of FECO (Section 2.1), and its density in order to initialise a simulation in the total scattering studies (Section 2.2).

2.3.1 | Refractive Index Measurements

Refractive index measurements were performed using an Abbe 60 Refractometer (Bellingham and Stanley). In order to perform the measurement, a drop of liquid is placed on a lower, measurement prism and an upper, illuminating prism is clamped onto the sample, forming a thin layer of the liquid between the two prisms. Monochromatic light from a sodium lamp of wavelength 589.3 nm passes through the illuminating prism and along the thin liquid film at grazing incidence, which then passes through the smooth, ground surface of the measurement prism. Light passes through the measurement prism with a critical angle determined by the ratio of the refractive indices between the liquid and the prism medium. This emergent light is passed through a series of lenses into an eyepiece. These lenses can be adjusted using a micrometer in order to accurately find the edge of the cone; thus the critical angle and refractive index can be determined. The micrometer measurements are recorded along with the sample temperature, and the Abbe Utility Program is used to calculate the final refractive index. Measurements are repeated ten times in order to improve the final accuracy.

2.3.2 | Density Measurements

The densities of the liquid samples investigated using total scattering in Chapter 5 were measured using a density meter (Anton Paar DMA 4100 M). A small amount of the sample ($\sim$ 1 mL) is inserted into a U-shaped tube which is excited into an oscillation. The frequency of this oscillation is determined and analysed, from which the density of the sample can be calculated to a precision of 0.0001 g cm^{-3}.

3 | Surface Forces Measurements Across Simple Electrolytes

3.1 | Background

In order to interrogate, both qualitatively and quantitatively, the surface forces measurements across the various aqueous solutions presented in this thesis, it is important to first consider the case of simple electrolyte solutions. This will allow us to introduce a framework through which we can interpret the solutions of increasing complexity in later chapters. To do so, in this chapter we will present surface forces measurements across two well understood liquids: pure water and a dilute potassium chloride electrolyte. In both cases, we will discuss in detail the various features of the total measured interaction profile, including both DLVO, and where observed, non-DLVO contributions.

3.2 | DLVO Theory - Further Details

Before discussing any experimental results, we will elaborate upon the DLVO framework required to interpret such measurements, beyond the introduction provided in Chapter 1.

Electric Double Layer Repulsion

The electric double layer contribution is a term of entropic origin which occurs due to an excess osmotic pressure arising from the overlap of the diffuse layers of cationic countercharge associated with the two negatively charged surfaces as they approach one another. This repulsive interaction can be calculated from the charge distribution away from the surface, as predicted by the Poisson-Boltzmann (PB) equation (Equation 1.6).

Solving the PB equation requires suitable surface boundary conditions, and these extremes are often taken as either constant charge (CC) or constant potential (CP) conditions. However, it often the case that neither CC or CP conditions alone can provide an accurate fit to experimental data. Instead, it is necessary to consider the adsorption of ions to the surfaces as they approach one another and the diffuse layers begin to overlap. This effect results in varying surface charge and potential as the distance between surfaces is changed, and is known as charge regulation. Ultimately, charge regulation is determined by the interplay between the charging of the inner and diffuse layers at each surface, *i.e.* if upon approach of the surfaces an ion is adsorbed within the inner layer, the surface charge at the origin of the diffuse layer is modified. Surface complexation models can be used to describe such effects - employing surface adsorption equilibrium and mass action laws in order to determine surface potentials - but they have the disadvantage of having a large number of parameters that cannot be determined independently. In this work, we employ the constant regulation approximation, which has been used to successfully interrogate a range of measurements across aqueous electrolyte solutions,[108,109] and allows for linear regulation between the CP and CC boundary conditions with a single dimensionless regulation parameter, p, taking values between 0 and 1.[110,111] The value of p can provide an indication of the molecular processes occurring during approach of the surfaces.

Solving the PB equation in this framework yields a contribution to the free energy of interaction from diffuse layer interactions $W_{\mathrm{PB}}^{||}$, given by Equation 3.1:

$$W_{\mathrm{PB}}^{||} = 2\epsilon_0\epsilon\kappa_{\mathrm{D}}\psi_{\mathrm{eff}}^2\frac{e^{-\kappa_{\mathrm{D}}D}}{1+(1-2p)e^{-\kappa_{\mathrm{D}}D}} \tag{3.1}$$

where ϵ_0 is the permittivity of free space, ϵ is the relative permittivity, ψ_{eff} is the effective surface potential, κ_{D}^{-1} is the Debye-Hückel screening length (defined previously in Equation 1.4), and p is the dimensionless charge regulation parameter that can take values between 0 and 1, where these limiting values recover the boundary

condition solutions of constant potential ($p = 0$) and constant charge ($p = 1$).

To further illustrate the the mechanisms encompassed by the charge regulation effects, Figure 3.1 illustrates schematically how the interfaces respond with decreasing surface separation with CC or CP dominated behaviour. In CP dominated conditions, the inner layer can compensate for the increase in charge density within the diffuse layer arising from electric double layer overlap as the surfaces approach; whereas in a CC dominated regime, the inner layer cannot perform such compensating effects.

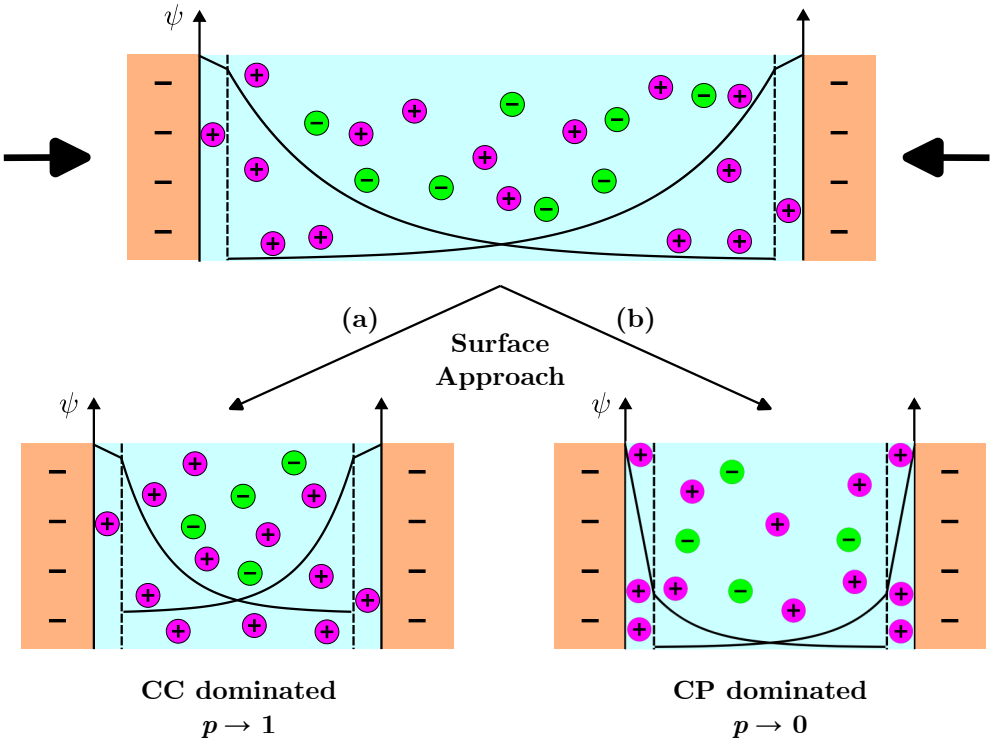

Figure 3.1: Schematic illustrating how the interfaces respond with decreasing surface separation, in CC and CP dominated regimes. The solid black lines indicate the decay of potential from each surface; the dashed black lines indicate the boundary between the inner and diffuse layers. (a) In a CC dominated regime, the inner layer does not compensate for the increase in charge within the diffuse layer resulting from electric double layer overlap as the surfaces approach. (b) In a CP dominated regime, the inner layer does compensate for the increase in charge accumulated within the double layer.

Van der Waals Interaction

The attractive van der Waals term can be calculated for two flat, macroscopic mica surfaces across an electrolyte. For this geometry, the contribution to the free energy

of interaction from van der Waals interactions $W_{\mathrm{vdW}}^{||}$ is given by Equation 3.2 as calculated by Hamaker:[112]

$$W_{\mathrm{vdW}}^{||} = -\frac{A}{12\pi D^2} \tag{3.2}$$

where A is the mica-electrolyte-mica Hamaker constant. Here, and in the remainder of this work, we estimate the Hamaker constant A across a given electrolyte solution between mica surfaces using the Lifshitz theory.[29] This approach extends the original Hamaker model of the summation of pairwise atomic interactions that was described in Chapter 1, accounting for the influence of neighbouring molecules on the interaction between each pair of molecules, necessary for condensed media. This approach derives the interactions between the bodies from bulk properties, including the relative permittivity and refractive indices. The Hamaker constant calculated by the Lifshitz theory has two terms: the first is a zero-frequency contribution, reflecting the interaction of static dipole fluctuations in the materials, and is dependent on the (static) relative permittivities of the various media. The second arises from considering the frequency-dependent dielectric response, and is refractive index-dependent. The full expression is displayed in Equation 3.3:

$$A = \frac{3}{4}kT\left(\frac{\epsilon_{\mathrm{m}} - \epsilon_{\mathrm{e}}}{\epsilon_{\mathrm{m}} + \epsilon_{\mathrm{e}}}\right)^2 + \frac{3h\nu_{\mathrm{e}}}{16\sqrt{2}}\frac{(n_{\mathrm{m}}^2 - n_{\mathrm{e}}^2)^2}{(n_{\mathrm{m}}^2 + n_{\mathrm{e}}^2)^{\frac{3}{2}}} \tag{3.3}$$

where ϵ_{m} and ϵ_{e} are the relative permittivities of mica and electrolyte, respectively, h is the Planck constant, ν_{e} is the plasma frequency of the free electron gas, and n_{m} and n_{e} are the refractive indices of mica and electrolyte, respectively.[29,113] Constants for mica were taken from the literature: ϵ_{m} was taken as 2, ν_{e} was taken as 3×10^{15} s^{-1}, and n_{m} was taken as 1.6.[29] In this chapter, the relative permittivity of the electrolytes studied ϵ_{e} was taken as 78.4, the value for pure water at 298 K.[114] In future chapters, where the solute concentration is more substantial, the solution relative permittivities are estimated by assuming a linear response with solute concentration, and the constants of proportionality - the dielectric increment

or decrement - are obtained from literature. The refractive index of the electrolytes were measured as described in Section 2.3.1.

Total DLVO Interaction

Overall, the full expression for the total interaction free energy between parallel plates $W^{||}$, predicted by the DLVO theory of colloidal stability equal to the sum of contributions from the Poisson-Boltzmann (Equation 3.1) and van der Waals terms (Equation 3.2), is shown in Equation 3.4.

$$W^{||} = -\frac{A}{12\pi D^2} + 2\epsilon_0\epsilon\kappa_{\mathrm{D}}\psi_{\mathrm{eff}}^2\frac{e^{-\kappa_{\mathrm{D}}D}}{1+(1-2p)e^{-\kappa_{\mathrm{D}}D}} \tag{3.4}$$

The effect of varying the charge regulation parameter p on the total interaction free energy $W^{||}$ is shown in Figure 3.2. The interaction energy was calculated using Equation 3.4 for three contrasting values of p: first, at the constant charge boundary condition ($p = 1$); second, at the constant potential boundary condition ($p = 0$); and third, at the mid-point between the two boundary conditions ($p = 0.5$). The comparison illustrates the stark differences between the interaction energies at small surface separations: the constant charge curve displays a very high maximum repulsive barrier, in contrast to the situations where $p < 1$ which display progressively smaller repulsive barriers when regulation of the surface charge is allowed to occur, as the value of p diminishes. It is also important to note that, at large distances, the three calculated lines tend towards the same result at large surface separations, illustrating that the deviations due to charge regulation effects are only significant at small separations.

All measured interaction free energy profiles in this thesis are fitted using the DLVO model outlined in Equation 3.4. A and ϵ are calculated for each solution composition, as described above. A non-linear least squares fitting algorithm is then used to fit values to ψ_{eff}, κ_{D}, and p. In order to account for small errors in the absolute distance D, the fitting procedure allows for small amounts of variation in

the zero separation position to maximise the quality of the fit. For all fits presented in this thesis, therefore, the fitted absolute zero surface separation D_0 is tabulated alongside the other determined parameters.

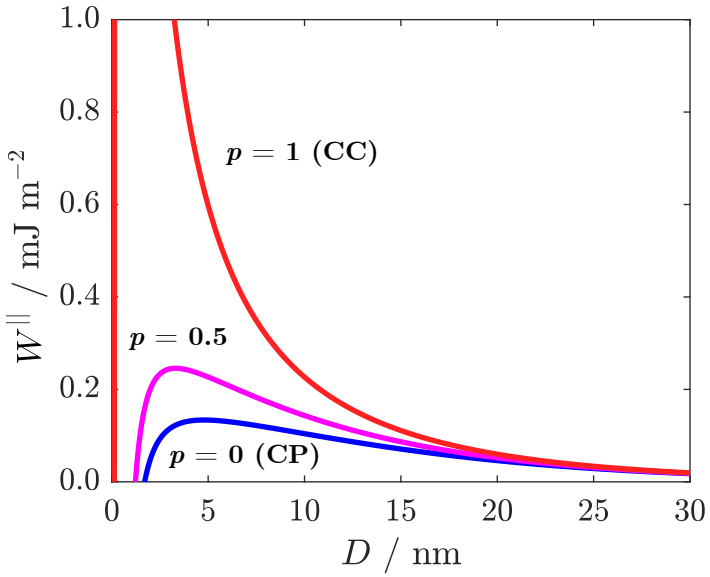

Figure 3.2: Total interaction free energy $W^{||}$ as a function of surface separation D, as predicted by the DLVO theory of colloidal stability in Equation 3.4. The calculated interaction free energy is shown for three contrasting values of the charge regulation parameter p: $p = 1$ (red), which represents the constant charge boundary condition; $p = 0$ (blue), which represents the constant potential boundary condition; $p = 0.5$ (magenta). The remaining parameters used in this DLVO calculation were equivalent for all three lines, and were predicted or taken from existing surface forces measurements for a 1 mM KCl solution: $\psi_{\text{eff}} = 54$ mV, $\kappa_{\text{D}}^{-1} = 9.7$ nm, A $= 21 \times 10^{-20}$ J.[1]

Calculation of Surface Charge Density

As has become apparent from our discussion thus far, depending on the specific situation, it can be useful to refer to either the surface charge or the surface potential. However, only a value for the effective surface potential ψ_{eff} is required to fit each measurement of interaction energy using the DLVO expression (Equation 3.4). It can be useful, therefore, to outline the relation which can be used to convert between the surface potential, determined directly from fitting, and an appropriate value for the surface charge σ. In this work, in order to perform such conversion, we use the relations discussed in the review article by Smith *et al.*,[109] which are reproduced

below.

For weakly charged surfaces ($\psi \lesssim 25$ mV), the effective surface charge density σ_{eff} can be calculated using the Debye-Hückel relation shown in Equation 3.5.

$$\sigma_{\text{eff}} = \epsilon_0 \epsilon \kappa_{\text{eff}} \psi_{\text{eff}} \tag{3.5}$$

For more highly charged surfaces ($\psi \gtrsim 25$ mV), the Poisson-Boltzmann framework introduced in Chapter 1 must be invoked. Equation 3.6 relates the effective surface potential ψ_{eff}, extracted from our measurements, and diffuse layer potential ψ_{dl}, the potential at the origin of the diffuse layer, across a symmetric 1:1 electrolyte.

$$\psi_{\text{eff}} = \frac{4k_{\text{B}}T}{e} \tanh\left(\frac{e\psi_{\text{dl}}}{4k_{\text{B}}T}\right) \tag{3.6}$$

A surface charge density σ can be calculated from the diffuse layer potential ψ_{dl} using the Graheme equation, shown in Equation 3.7 for a symmetric 1:1 electrolyte.

$$\sigma = \frac{2k_{\text{B}}T\epsilon_0\epsilon\kappa_{\text{D}}}{e} \sinh\left(\frac{e\psi_{\text{dl}}}{2k_{\text{B}}T}\right) \tag{3.7}$$

3.3 | Experimental Details

3.3.1 | Materials and Solution Preparation

In this chapter, we present measurements of surface forces between mica surfaces across both pure water and a 0.001 m KCl electrolyte. KCl (Thermo Scientific, Puratronic$^{\text{TM}}$, 99.997%) was used as received and stored under dry conditions until use. Surface forces measurements were performed using the SFB as described in Chapter 2.

3.3.2 | Refractive Indices and Hamaker Constants

The refractive indices for the electrolytes investigated in this chapter were measured using the method outlined in Chapter 2. The Hamaker constants for all electrolytes

reported in this chapter are displayed in Table 3.1.

Table 3.1: Parameters used for Hamaker constant calculations. Refractive index n_e, relative permittivity ϵ_e and Hamaker constant A are shown.

Solution	n_e	ϵ_e	A / 10^{-20} J
Pure water	1.3320	78.4	2.08
0.001 m KCl	1.3320	78.4	2.08

3.4 | Pure Water

The measured interaction free energy, as a function of the separation between mica surfaces across pure water, is displayed in Figure 3.3. Upon approach, the surfaces repel each other from large distances; the repulsion increases in strength down to surface separations of around 5 nm, at which point the surfaces jump into close surface separation owing to a large attractive force causing a spring instability. This jump brings the surfaces to an observed surface separation of -0.7 nm, at which point no change in surface separation is seen upon continued application of increasing force; in other words, a repulsive hard wall is observed, indicative of surface contact. Measured negative surface separations relative to the calibrated mica-mica contact in air can be attributed to a layer of adsorbed water and carbon dioxide from the atmosphere formed on mica surfaces during the mica cleaving process, which will quickly dissolve upon immersion in water.[115–117]

In additional to the raw, measured data points, Figure 3.3 also displays the fit to this measurement using the DLVO model. We obtain a good fit to the measured data using this model, and the fitted parameters are displayed in Table 3.2. The good fit suggests that mica surfaces interact across pure water in accordance with DLVO theory, and no structural, non-DLVO terms contributions are observed. Similar surface forces measurements have been made across pure water samples by Israelachvili, Pashley, Raviv, Klein and others, all of which reveal a long-range electric double layer repulsion and an attractive jump together of the surfaces at small separations.[64,118–122]

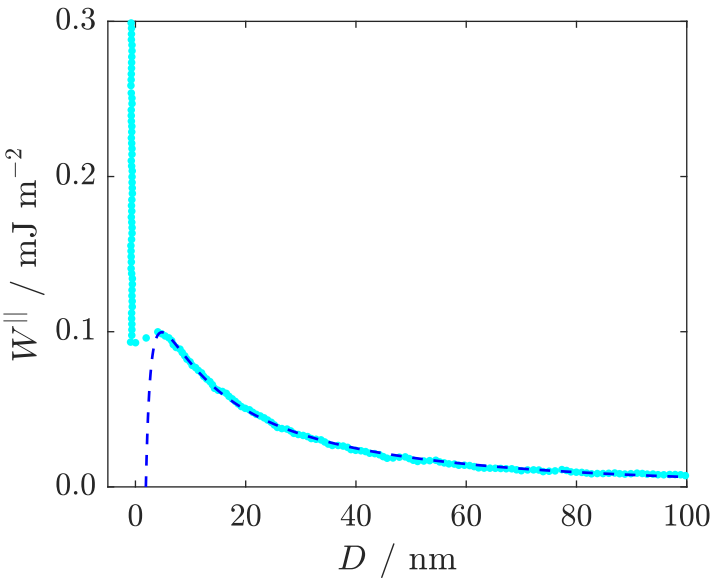

Figure 3.3: Measured interaction free energy as a function of surface separation across pure water. The measured interaction potential on approach of surfaces is shown in light blue. The DLVO fit to the long-range repulsive regime using Equation 3.4 is shown by the dashed dark blue curve, the parameters for which are displayed in Table 3.2.

Table 3.2: Parameters obtained from the DLVO fit to the measured interaction free energy across pure water shown in Figure 3.3. The fitted effective surface potential ψ_{eff}, Debye screening length κ_{D}^{-1}, charge regulation parameter p and offset to the zero surface separation D_0 are shown.

	ψ_{eff} / mV	κ_{D}^{-1} / nm	p	D_0 / nm
Pure Water	38 ± 14	65 ± 21	0.88 ± 0.10	0.1 ± 1.3

A deep minimum is revealed upon retraction of the surfaces. However, the separation to which the surfaces jump upon retraction is larger than that which can be accurately determined using the approach outlined in Chapter 2. Therefore, the adhesive minimum can also not be accurately determined and no data obtained upon retraction of the surfaces are shown here.

3.5 | Dilute Potassium Chloride Electrolytes

The interaction energy between negatively charged surfaces across a 0.001 m concentration solution of KCl in water is shown in Figure 3.4. As for the measurement across pure water, there exists a repulsive force that is observed from long-range distances ($\sim$ 100 nm); the DLVO fit to this is again shown, and the associated pa-

rameters are displayed in Table 3.3. However, instead of observing the surfaces jump together over the distance of several nanometres due to an attractive, van der Waals interaction, at distances smaller than 3 nm alternating repulsive and attractive regions are observed with jump-in distances of size ~ 0.3 nm. Such an observation suggests the presence of a structural, non-DLVO contribution, which is seen rather than the van der Waals jump, preventing the surfaces from falling into adhesive contact.

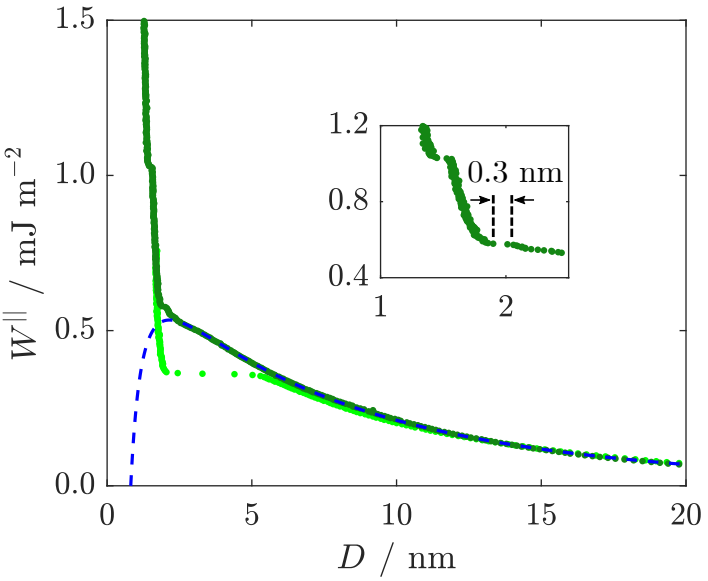

Figure 3.4: Measured interaction free energy as a function of surface separation across 0.001 m KCl. The measurement upon approach of the surfaces is shown in dark green and that upon retraction is shown in light green. The DLVO fit is shown by the blue dashed curve, parameters for which are displayed in Table 3.3. The inset shows a zoomed-in view of the structural features.

Table 3.3: Parameters obtained from the DLVO fit to the measured interaction free energy across the 0.001 m KCl electrolyte shown in Figure 3.4. The fitted effective surface potential ψ_{eff}, Debye screening length κ_{D}^{-1}, charge regulation parameter p and offset to the zero surface separation D_0 are shown. The predicted Debye screening length $\kappa_{\text{D, pred}}^{-1}$ for this ion concentration is also shown.

	ψ_{eff} / mV	κ_{D}^{-1} / nm	p	D_0 / nm	$\kappa_{\text{D, pred}}^{-1}$ / nm
0.001 m KCl	56 ± 4	9.5 ± 0.9	0.72 ± 0.06	0.2 ± 0.3	9.7

A strong, short-range contribution to the measured interaction at small distances (less than ~ 2 nm) is consistent with previous observations by Pashley and

Israelachvili[118,123–125] who suggested the presence of so-called 'hydration forces' to explain the observed steep repulsion at small surface separations. The fact that the DLVO theory does not capture the measured interactions at small surface separations can be rationalised by molecular size effects. The DLVO interactions are based on mean field approximations, where solvents are continuous and ions are point charges: this approximation breaks down at small surface separations where the distance is close to the size of ions and molecules.

In a series of experiments investigating the phenomenon of hydration forces in aqueous electrolyte solutions, Pashley and Israelachvili found that at low enough salt concentrations, the interaction between mica surfaces in a surface forces measurement did obey DLVO theory, and no structural contributions to the measured forces at small separations were observed. Instead, hydration forces were only measured at high enough electrolyte concentrations, above the 'critical hydration concentration' at which these additional forces could be seen. From their measurements they suggested that these forces arise from the hydration of the surfaces due to the binding of cations to the surface, which retain some of their hydrating water molecules upon binding. When the surfaces come close to contact, these water molecules are expelled with the 'squeeze out' of individual 0.3 nm layers of molecules resulting in the observed stepped interaction profile. In a series of measurements across salt solutions with varying cations, this theory was also supported through the observation that the strength and range of hydration forces is positively correlated with the hydration number of the binding cations, and also with the critical hydration concentration.[29] In KCl solutions, the critical concentration required to measure hydration forces was found to be $\sim 10^{-4}$ M.[123]

The presence and role of hydration forces has been investigated in systems including more complex situations such as rough or chemically heterogeneous surfaces, and soft biological or amphiphilic surfaces. Monotonic, short-range forces are found to be present between such hydrophilic surfaces and play a significant role in de-

termining the behaviour of a range of systems, including the stability of colloidal dispersions,[126] the swelling of clays[127] and the interactions between biological membranes.[128,129]

Specifically oscillatory hydration forces have only be observed on a handful of occasions experimentally using the surface forces apparatus, firstly by Pashley and Israelachvili in the 1980s[124,125] and recently in our laboratory.[1] Measurements using atomic force microscopy have also revealed similar oscillatory forces.[130] Such oscillatory forces are not unique to water-dominated layering in aqueous systems; other solvent-dominated layering has been observed in different liquid systems including the polar solvent, propylene carbonate.[131] Water layering in particular remains challenging to measure due to the demanding distance sensitivity required, and as there are only a limited number of literature measurements their presence is sometimes been considered controversial. These features can only be observed in optimum experimental conditions, where the surfaces being used to perform the measurement must be sufficiently smooth and free of contamination, and the experimental setup must have sufficient mechanical stability. The measurement of either monotonic or oscillatory hydration forces may initially appear conflicting. However, these differing observations may be reconciled by considering that the 'smearing out' of oscillatory contributions if the surfaces are too rough or the mechanical stability of the measurement technique is poor can result in a smooth, monotonic repulsion being the overall measured contribution.[132] It is worth noting, however, the concept of hydration forces is abundant in its usage in the literature to describe deviations from DLVO theory at various lengthscales. For clarity, the use of the term will only be used in this thesis to describe any observed water-dominated steps in measured interaction profiles.

Whilst the form of our measured hydration forces can be rationalised through the packing of water molecules between the surfaces, there remain unanswered questions about their origin. As previously noted, structural forces are observed for other polar

solvents including propylene carbonate in the absence of any additional solutes. It is interesting, therefore, why the presence of hydration forces in aqueous electrolytes is linked to a minimum ion concentration, above or below which the overall interaction profile can take significantly different forms as highlighted in Figure 3.5.

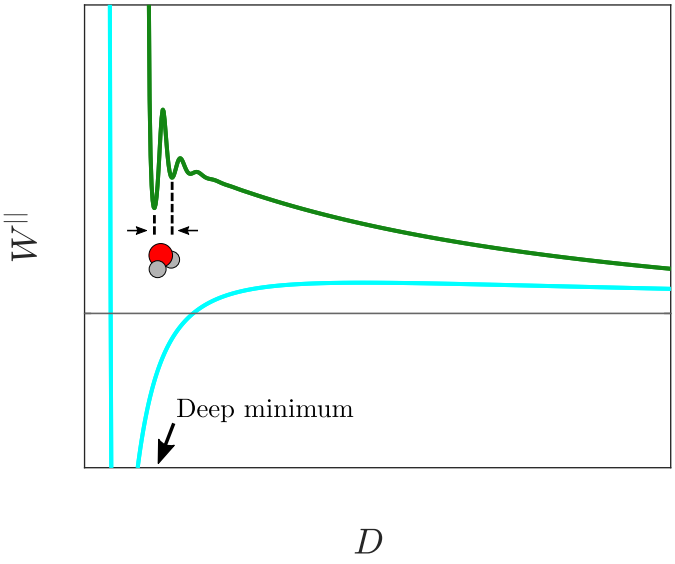

Figure 3.5: Schematic of the interaction free energy as a function of surface separation in pure water (light blue) and a dilute KCl electrolyte (green). The pure water measurement obeys predictions from DLVO theory, exhibiting a deep adhesive minimum at small surface separations. In contrast, the dilute KCl electrolyte exhibits oscillatory structural forces, with a characteristic wavelength approximately equal to the size of a water molecule, preventing the effects of a van der Waals jump and the resulting deep adhesive minimum.

3.6 | Summary

In this chapter, we have introduced the framework required to interrogate measurements of interaction free energies between surfaces through the lens of simple, dilute electrolytes. We began with a discussion of the DLVO model which incorporates charge regulation effects upon approach of the surfaces, which will be used to quantitatively interpret surface interactions across various electrolytes throughout this work. This was followed with a presentation of direct surface force measurements across pure water and a dilute 0.001 m KCl electrolyte, including fits to the DLVO model.

For the measurement across the KCl electrolyte, we also discussed the presence of structural forces which are observed at small surface separations, not predicted by the mean-field DLVO theory. Our observation of hydration forces in this electrolyte, in accordance with literature measurements across similar electrolytes, emphasises the fact that, even at low electrolyte concentrations, non-DLVO contributions can be significant, especially at small surface separations.

Knowledge of surface interactions across aqueous electrolytes systems is essential for understanding various processes in nature including those involving biological surfaces. In this chapter we have introduced a framework through which these interactions can be interrogated, and upon which we can build as the complexity of such electrolytes increases. However, our discussion has shown that even in the most simple electrolytes, the interactions can be complex and beyond mean-field theories.

4 | The Role of Zwitterions in Model Cytosol Solutions

4.1 | Background

In Chapter 1, we outlined some of the biochemical strategies employed by various organisms in order to perform osmoregulation, most notably in those that have evolved to survive and thrive in high salinity environments. We described one of the significant challenges facing these organisms - the requirement to accumulate molecules in order to tune the osmotic balance without deleteriously perturbing intracellular functionality - and highlighted some common osmolytes that are used across the biosphere, such as trimethylglycine or proline, which are present as zwitterions in ambient conditions. As neutral molecules, they might, traditionally, be considered to simply contribute towards the 'dielectric background' of the surrounding fluid and not significantly modify inter-particle interactions. Therefore, whilst a multicomponent osmolytic environment is required to tune both the osmotic balance and interactions between intracellular particles, the roles of these osmolytic species in mediating interactions have remained relatively unexplored, in contrast to simple salts whose role is much better understood. However, recent works studying more complex osmolytic systems have begun to reveal a more significant influence on such interactions by these neutral molecules, warranting further study of their contribution to the overall osmolytic background.[133–136]

In this chapter, we report on model experiments investigating the combined effect of zwitterionic solutes, with and without added ionic co-solutes, on the measured interaction energy across electrolytes. This allows for the exploration of the role played by these common osmolytes in modifying interactions between charged particles, and to reveal potential synergies or competing effects between different

Figure 4.1: Molecular structure of zwitterions (a) L-proline and (b) trimethylglycine.

zwitterionic and ionic solutes present. In this series of measurements, we study the influence of two osmolytic zwitterions, L-proline (Pro) and trimethylglycine (TMG), with and without added KCl. The molecular structures of these two osmolytes are displayed in Figure 4.1.

4.1.1 | Proline

Proline, an amino acid used in the synthesis of proteins, plays a significant role as an osmoprotectant in a variety of plant species.[23,137] In particular, organisms exposed to environmental stresses such as high salinity, drought, extreme temperatures and UV radiation have been found with elevated proline levels.[138–141] In one example among vascular halophytes, free proline was found to be present in quantities of up to $10 - 20\%$ of the dried shoot weight *Triglochin maritima*.[142]

As for other osmolytes, proline is known to protect these organisms living in salt-stressed environments primarily by matching the osmotic pressure of the cellular fluid with that of the external growth environment, thus providing a barrier against dehydration.[8,20] It has also been shown to have additional protective properties, including by acting as a free radical scavenger and buffering cellular redox potentials,[139] therefore providing protection against oxidative stress.[143]

Inspired by its utilisation in biological organisms, proline has also shown to be beneficial in agricultural contexts. When provided exogenously to plants in salt-stressed environments, it has been found to enhance the growth rate of various crops.[144] The amino acid therefore has potential for usage in agricultural applications, and could provide a route to combat the increasing salinisation of soils arising from the anthropogenic accumulation of salts in farmland.[145–148]

As previously discussed, the accumulation of proline in the biological fluids in response to external osmotic stress should not be deleterious towards cellular activity. Indeed, enzyme activity has been found to be relatively insensitive to wide changes in proline concentration for a range of enzymes in salt-tolerant plants (halophytes).[142] In terms of any potential influence on intracellular interactions, in a recent study proline was observed to directly modulate the strength of protein-protein interactions, rendering the interactions more repulsive even at millimolar concentrations.[149,150] Furthermore, proline has been shown to control the formation of liquid-liquid phase separated droplets (biomolecular condensates) *in vivo*.[151]

4.1.2 | Trimethylglycine

Trimethylglycine - also known as glycine betaine - is an osmolyte that is widely found across the biosphere; indeed it has been discovered to be accumulated in all three kingdoms of life, in both halophilic and non-halophilic organisms.[16–18,152] Typical concentrations of TMG in halophilic organisms are on the order of several hundred millimolar, though in the most strongly halophilic organisms concentrations can reach several molar.[20,153]

In addition to providing resistance to osmotic stress or stabilising protein structure, TMG is also involved in various metabolic or synthetic processes. It contributes to the synthesis of many biological molecules through various metabolic pathways, including as a methyl group donor. For example, it is used in the remethylation of homocysteine to methionine, an essential amino acid, necessary for the regulation of homocysteine levels and mediating cardiovascular risk.[154] Ultimately, TMG is degraded to methylglycine or glycine, which can then be incorporated into proteins.[155] Anything that threatens the bioavailability of this osmolyte can then therefore result in a negative impact on cell health or function through disrupting such metabolic pathways.[156]

4.2 | Experimental Details

4.2.1 | Materials and Solution Preparation

We investigated the surface forces and structures present in aqueous solutions containing proline or trimethylglycine as the zwitterionic osmolytes of interest; either as the sole solute, or with potassium chloride as a co-solute. L-Proline (Sigma-Aldrich®, BioUltra, $\geq$ 99.5%), trimethylglycine (Sigma-Aldrich®, BioUltra, $\geq$ 99.0%) and KCl (Thermo Scientific, Puratronic^{TM}, 99.997%) were used as received and stored under dry conditions until use. Surface forces measurements were performed across a range of concentrations of the two solutes using the SFB as described in Chapter 2. Raw data for the surface forces measurements performed in this chapter are available from the Oxford University Research Archive.[157,158]

4.2.2 | Refractive Indices and Hamaker Constants

The refractive indices for the electrolytes were measured using the method outlined in Chapter 2. The Hamaker constants for all electrolytes reported in this chapter are shown in Table 4.1 for the Pro-KCl electrolytes and Table 4.2 for the TMG-KCl electrolytes. The displayed relative permittivity of the electrolytes were estimated using Equation 4.1:

$$\epsilon_{\mathrm{e}} = \epsilon_{\mathrm{r}}^{0} + \delta_{\mathrm{Zw}} c_{\mathrm{Zw}} + \delta_{\mathrm{KCl}} c_{\mathrm{KCl}} \tag{4.1}$$

where $\epsilon_{\mathrm{r}}^{0}$ is the relative permittivity of water (78.4), δ_i is the dielectric increment or decrement of the zwitterion (Zw = Pro or TMG) or KCl and c_i is the solute concentration. The dielectric increments or decrements were obtained from literature, and we have taken δ_{Pro} to be 21.0 / m,[159] δ_{TMG} to be 18.2 / m,[160] and δ_{KCl} to be -8.85 / m.[161]

Table 4.1: Parameters used to calculate the Hamaker constant for the Pro-KCl solutions investigated in this chapter. Concentrations of Pro c_{Pro} and KCl c_{KCl}, refractive index n_{e}, relative permittivity ϵ_{e} and Hamaker constant A are shown.

c_{Pro} / m	c_{KCl} / m	n_{e}	ϵ_{e}	A / 10^{-20} J
0.07	-	1.3339	79.9	2.05
0.35	-	1.3394	85.5	1.98
0.90	-	1.3507	97.3	1.84
0.33	0.001	1.3382	85.3	2.00
0.46	0.010	1.3414	88.0	1.96
-	0.010	1.3321	78.3	2.08
-	2.500	1.3551	56.3	1.76

Table 4.2: Parameters used to calculate the Hamaker constant for the TMG-KCl solutions investigated in this chapter. Concentrations of TMG c_{TMG} and KCl c_{KCl}, refractive index n_{e}, relative permittivity ϵ_{e} and Hamaker constant A are shown.

c_{TMG} / m	c_{KCl} / m	n_{e}	ϵ_{e}	A / 10^{-20} J
0.06	-	1.3330	79.7	2.07
0.75	-	1.3448	92.1	1.91
0.50	0.001	1.3405	87.5	1.97
2.88	0.130	1.3814	129.7	1.47
0.50	0.800	1.3470	80.4	1.88

4.3 | Surface Forces Measurements Across Proline Solutions

4.3.1 | Proline-Only Solutions

The measured interaction free energy across an aqueous solution of proline at a low concentration (0.07 m) with no added salt is shown in Figure 4.2. Upon approach the surfaces repel one another from large separations, with the repulsion increasing in strength as the separation decreases. This repulsion continues to increase down to a surface separation of around 4 nm, at which point a strong attractive force dominates and the surfaces jump together. The presence of a strong attraction (energy minimum) is confirmed upon separation of the surfaces, where a negative interaction energy of around -1 mJ m^{-2} is required to bring the surfaces out of contact, at which point there is a sudden jump to large surface separations.

In addition to the experimental measurements, the inset to Figure 4.2 also shows

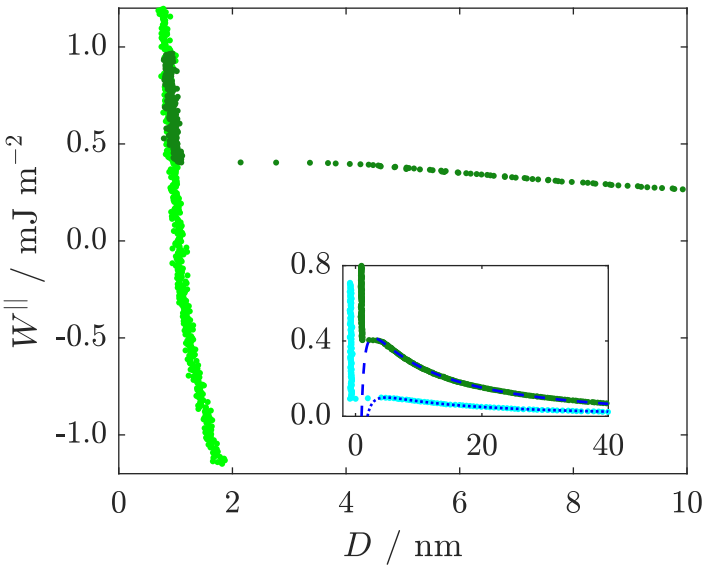

Figure 4.2: Measured interaction free energy as a function of surface separation across a solution containing 0.07 m proline. The measurement upon approach of the surfaces is shown in dark green and that upon retraction is shown in light green. The DLVO fit is shown in the inset by the blue dashed curve, parameters for which are displayed in Table 4.3. The interaction across pure water is also shown in light blue in the inset for comparison, along with its associated DLVO fit shown by the dark blue dotted line.

the fit of the long-range, monotonic repulsive regime to the charge regulation DLVO model that was introduced in Chapter 3, along with a comparison to the measurement across pure water presented in the previous chapter. The chosen functional form for the interaction potential provides an accurate fit to the long-range repulsion, as well as providing an attractive force that can explain the jump at smaller surface separations. The parameters resulting from this fit are displayed in Table 4.3 and reveal a measured Debye-Hückel screening length $\kappa_{\mathrm{D}}^{-1} = 40 \pm 2$ nm, which corresponds to a 1:1 salt concentration of approximately 6×10^{-5} M. With no salt added in the preparation of this electrolyte, this small amount of residual ionic strength could arise from a number of possible sources, including trace ionic impurities in the proline samples, dissolution of carbon dioxide in the electrolyte and auto-ionisation of water.[81,123]

Despite there being little difference in the Debye screening length between the proline and pure water cases, there is a significant enhancement to the effective sur-

Table 4.3: Parameters obtained from the DLVO fit to the measured interaction free energy across the 0.07 m Pro solution shown in Figure 4.2. The fitted effective surface potential ψ_{eff}, Debye screening length κ_{D}^{-1}, charge regulation parameter p and offset to the zero surface separation D_0 are shown.

c_{Pro}/ m	ψ_{eff} / mV	κ_{D}^{-1} / nm	p	D_0 / nm
0.07	63 ± 5	40 ± 2	0.90 ± 0.01	0.0 ± 0.0

face potential in the presence of proline: $\psi_{\text{eff}} = 62 \pm 5$ mV ($\approx 2.5\ k_{\text{B}}T/e$) for 0.07 m proline and $\psi_{\text{eff}} = 38 \pm 14$ mV ($\approx 1.5\ k_{\text{B}}T/e$) for pure water. Such enhancement may occur due to adsorption of proline zwitterions at the mica interface, evidence for which we shall see more clearly in subsequent measurements across higher proline concentrations. There may be multiple driving forces for this adsorption, but most simply, it can be rationalised by considering the favourable interaction between the negatively charged surface and the high molecular dipole moment of the proline zwitterion. The interfacial zwitterions replace the ions that would otherwise be present in the Stern layer, and the cations have a reduced affinity to the plane of negative charge at the edge of the zwitterion layer than to the charged mica interface. This results in a more negative effective potential relative to the pure water measurement.

In order to illustrate the described differences between the pure water and proline-containing measurements, a schematic illustrating the structure of the charged interfaces is shown in Figure 4.3. The schematic shows the case with and without zwitterions, along with representative plots of electric potential ψ as a function of distance from the interface x.

The fitted charge regulation parameter is found to be $p = 0.90 \pm 0.03$, and indicates that, for 0.07 m proline, the system remains close to the CC boundary during approach of the surfaces. This is likely a result of the very small concentration of free ions present in the solution (6×10^{-5} M, as calculated previously) available to adsorb during approach of the surfaces. In light of this, it is meaningful to report the surface charge σ_{eff} which can be calculated from the effective surface potential using the Graheme equation, which was discussed in Chapter 3. For this measurement,

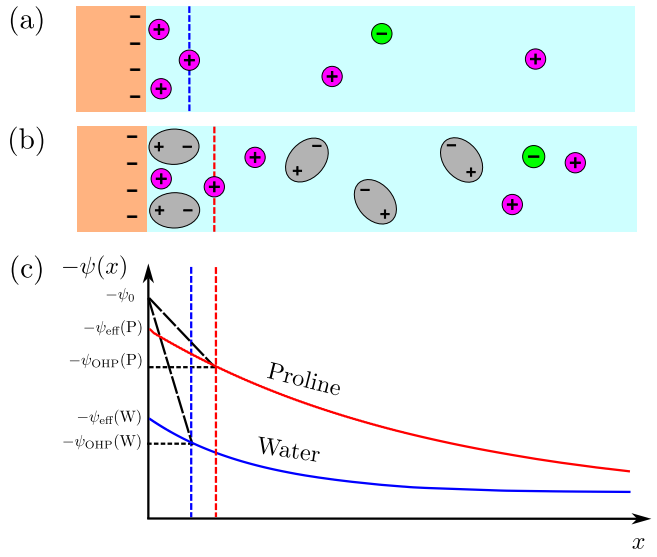

Figure 4.3: Schematic illustrating the structure of a charged interface in two cases: (a) no zwitterions and (b) with zwitterions, and (c) an illustrative plot of potential ψ as a function of distance from the interface x in both cases. The actual surface potential at the interface ψ_0, the effective potential extrapolated from the electric double layer potential ψ_{eff} and the Outer Helmholtz Plane (OHP) potential ψ_{OHP} are shown. These values differ because the decay of potential across the Stern layer is not captured in the Poisson-Boltzmann equation.

we calculate the surface charge to be $\sigma_{\text{eff}} = 1.8$ mC m^{-2}; a result slightly lower than biologically relevant net surface charges, such as the average net surface charge of proteins in *E. coli* cells which takes the value $\sigma_{\text{eff}} = 15$ mC m^{-2}.[162] Both of these values are larger than that measured across pure water $\sigma_{\text{eff}} = 0.4$ mC m^{-2}.

Next, we look to measurements at higher proline concentrations. A measurement performed across a 0.90 m proline solution is shown in Figure 4.4, with the DLVO fit displayed in the inset. The parameters associated with the DLVO fit are displayed in Table 4.4. We observe a similar long-range repulsion as the surfaces approach, again with an enhanced effective surface potential relative to the pure water case ($\psi_{\text{eff}} = 49 \pm 5$ mV) along with a mostly unchanged Debye screening length ($\kappa_{\text{D}}^{-1} = 30 \pm 5$ nm) and charge regulation parameter ($p = 0.92 \pm 0.03$).

At elevated concentrations, however, we observe an additional feature at small surface separations not present at the lower concentration. A spring instability is again seen from around 4 nm, but not into as small a surface separation. Instead,

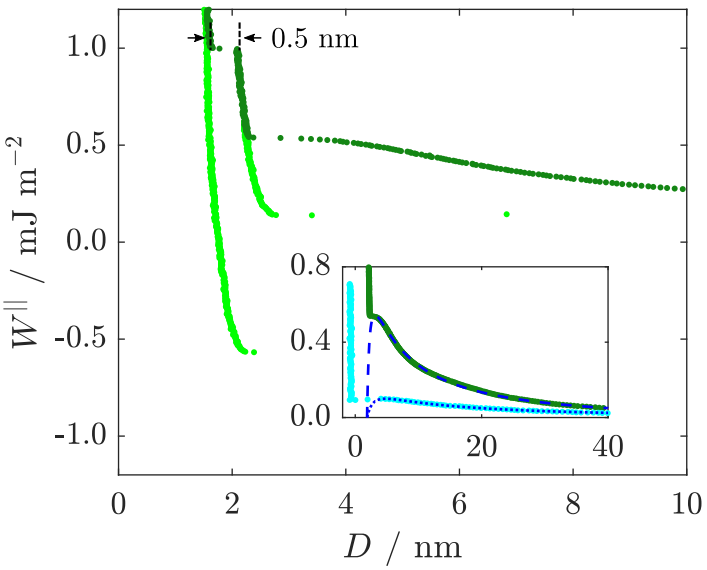

Figure 4.4: Measured interaction free energy as a function of surface separation across a solution containing 0.90 m proline. The measurement upon approach of the surfaces is shown in dark green and that upon retraction is shown in light green. The DLVO fit is shown in the inset by the blue dashed curve, parameters for which are shown in Table 4.4. The interaction across pure water is also shown in light blue in the inset for comparison, along with the associated DLVO fit shown by the dark blue dotted line.

Table 4.4: Parameters obtained from the DLVO fit to the measured interaction free energy across the 0.90 m Pro solution shown in Figure 4.4. The fitted effective surface potential ψ_{eff}, Debye screening length κ_{D}^{-1}, charge regulation parameter p and offset to the zero surface separation D_0 are shown.

c_{Pro}/ m	ψ_{eff} / mV	κ_{D}^{-1} / nm	p	D_0 / nm
0.90	49 ± 2	30 ± 5	0.92 ± 0.03	0.6 ± 0.3

a hard wall in the interaction profile is observed at an intermediate distance. Upon onset of the initial spring instability during approach, the surfaces jump to 2.3 nm surface separation where a steep repulsion is observed. At $W^{\parallel} \approx 1$ mJ m^{-2}, the surfaces jump together to ~ 1.5 nm, the closest measurable surface separation. This jump is different to the previous one: instead of occurring due to a maximum in the DLVO interaction, it is occurring between two hard walls in the interaction profile, *i.e.* in a similar manner to the jumps observed between water layers in the KCl electrolyte presented in the previous chapter.

Quantitatively similar measurements containing this additional feature were made for a range of concentrations between 0.26 m and 0.90 m (see Figure A.1 for an

additional measurement at a proline concentration of 0.35 m). Across these measurements, the step size is reproducibly found to be 0.5 ± 0.1 nm, consistent with the size of a proline molecule along its axis as obtained from X-ray diffraction structural determination.[163] We suggest therefore, that this structural, non-DLVO feature at small surface separations arises from layers of proline adsorbing with their positively charged ammonium group at the negatively charged mica surface, and the negatively charged carboxylate group pointing away from the surface. Our interpretation of proline forming layers at the interface is consistent with our earlier analysis behind the enhanced effective surface potential, as well as other recent discoveries finding layering of zwitterions at charged interfaces.[136]

Interestingly, the longer-ranged force between the surfaces across proline solutions appears remarkably insensitive to the proline concentration (above a low threshold; in our experiments the lowest concentration studied is 0.07 m). Higher proline concentration gives rise to more adsorbed layers and stronger short-range forces, but the far-field is not affected. It appears that accumulation of proline could be used to tune the osmotic pressure whilst retaining close regulation of interaction forces.

4.3.2 | Proline-KCl Mixtures

Next, we present surface forces measurements across aqueous mixtures containing both proline and KCl: a measurement of a solution containing 0.46 m proline and 0.01 m KCl is shown in Figure 4.5. The parameters associated with the DLVO fit to the long-range repulsion are displayed in Table 4.5, where we see an effective surface potential similar to the proline-only cases ($\psi_{\text{eff}} = 49 \pm 5$ mV). In contrast, there is a noticeable difference in the Debye screening length ($\kappa_{\text{D}}^{-1} = 3.0 \pm 0.2$ nm) and the charge regulation parameter ($p = 0.61 \pm 0.08$). The Debye length can be simply attributed to the presence of KCl, matching that predicted for a 1:1 electrolyte solution at the same KCl concentration (3.0 nm, according to Equation 1.4). Clearly,

the reduced value of p in the presence of 0.01 m KCl indicates an increased tendency to regulate surface charge during approach: the higher ion concentration means that ions are more available in solution to adsorb and lower the effective charge. Consistent with this observation, a measurement across 0.33 m proline in the presence of 0.001 m KCl, displayed in Figure A.2, was found to have an intermediate value between these two cases ($p = 0.84 \pm 0.03$).

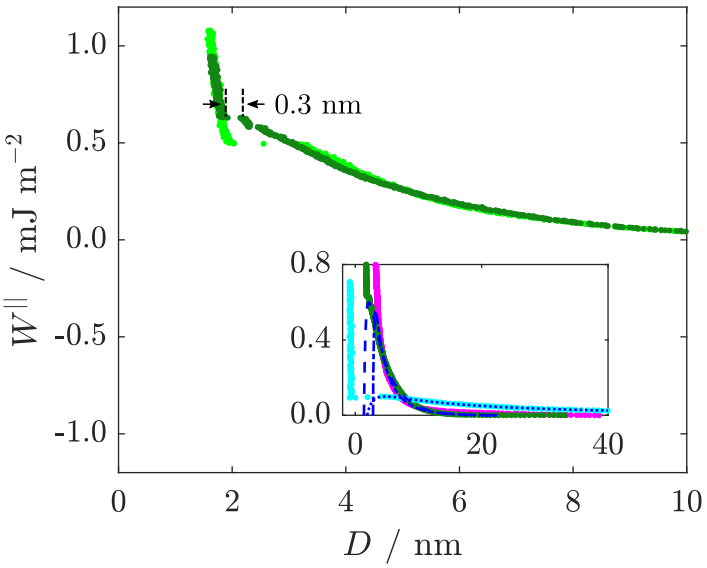

Figure 4.5: Measured interaction free energy as a function of surface separation across a solution containing 0.46 m proline and 0.01 m KCl. The measurement upon approach of the surfaces is shown in dark green and that upon retraction is shown in light green. The DLVO fit is shown in the inset by the blue dashed curve. In the inset, the interaction across pure water is shown in light blue, along with its DLVO fit shown by the dark blue dotted line. The inset also shows the interaction profile for 0.01 m KCl displayed in magenta, measured by Dr James Hallett, and the associated DLVO fit shown by the dark blue dash-dotted line. Parameters for the DLVO fits are displayed in Table 4.5.

Table 4.5: Parameters obtained from the DLVO fits to the measurements of interaction free energy shown in Figure 4.5. The fitted effective surface potential ψ_{eff}, Debye screening length κ_{D}^{-1}, charge regulation parameter p and offset to the zero surface separation D_0 are shown. The predicted Debye screening length $\kappa_{\text{D, pred}}^{-1}$ is also shown. †The quality of the fit for this measurement is lower than for the others, and as such, the derived parameters may be less reliable.

c_{Pro}/ m	c_{KCl}/ m	ψ_{eff} / mV	κ_{D}^{-1} / nm	p	D_0 / nm	$\kappa_{\text{D, pred}}^{-1}$ / nm
0.46	0.010	49 ± 3	3.0 ± 0.2	0.61 ± 0.08	0.6 ± 0.3	3.3
-	0.010 †	29 ± 1	3.8 ± 0.8	1.0 ± 0.0	2.3 ± 0.4	3.1

Turning to the non-DLVO, structural contribution at small surface separations: we see that, in the presence of salt, the short range 'step' characteristic of squeezing out near-surface molecular layers is now reduced to 0.3 ± 0.1 nm. Such features are reminiscent of those present in measurements across dilute aqueous electrolyte solutions investigated in Chapter 3. As discussed there, the hydration forces are thought to be intrinsically linked to the presence of weakly hydrated ions at the mica interface. Despite proline zwitterions being present at much higher concentration than the KCl ions, it appears that the structural features are now dominated by the molecular packing of hydrated ions at the interface. Indeed, this observation of a shift in the structural features from proline-dominated to water-dominated due to the presence of monovalent ions in the solution is consistent with the appearance of charge regulation behaviour across the solutions with salt. Constant charge behaviour prevails in the electric double layer repulsive regime when proline dominates the near-surface structure, but charge regulation is enhanced when the water-dominated structural features are observed, owing to the presence of adsorbed ions at the interface.

Finally, we return to examine the values of surface potential and surface charge density apparent in each of our experiments, as displayed in Table 4.6. It is noticeable that the values of the determined effective surface potentials ψ_{eff} vary only slightly with electrolyte composition in the range $1k_{\text{B}}T - 3k_{\text{B}}T$. In contrast, the value of the surface charge in the presence of proline is much more variable and sensitive to ion concentration: values range from $\sigma_{\text{eff}} \sim 2$ mC m^{-2} with no added KCl, to ~ 4 and ~ 16 mC m^{-2} in the presence of 0.001 m and 0.01 m KCl, respectively. This arises from the intrinsic inverse coupling between σ_{eff} and κ_{D}^{-1} for (relatively) invariant ψ_{eff}; the latter being set by the ambient thermal energy. For a fixed available energy, a higher surface charge can be supported at higher salt concentration due to the shorter-ranged screening leading to a lower average charge separation. Conversely, at low salt concentration, only a low surface charge can be supported

due to the larger average separation over the electrical double layer.

Table 4.6: Table of calculated constants for surface potentials and charge densities. Concentrations of proline c_{Pro} and KCl c_{KCl}, fitted effective surface potential ψ_{eff}, effective surface charge density σ_{eff}, double layer potential ψ_{dl} and surface charge density σ are shown. †The quality of the fit for this measurement is lower than for the others, and as such, the derived parameters may be less reliable.

c_{Pro}/ m	c_{KCl}/ m	κ_{D}^{-1} / nm	ψ_{eff} / mV	σ_{eff} / mC m^{-2}	ψ_{dl} / mV	σ / mC m^{-2}
-	-	65	38	0.4	40	0.5
0.07	-	40	63	1.1	74	1.8
0.35	-	34	55	1.2	61	1.7
0.90	-	30	49	1.4	54	1.8
0.33	0.001	11	49	3.3	53	4.3
0.46	0.010	3.0	49	12.5	53	16.2
-	0.001	9.5	56	4.1	63	5.8
-	0.010 †	3.8	29	5.3	30	5.7

4.3.3 | Influence of Solution Composition on Interfacial Structure

Across the range of measurements seen for solutions containing proline, KCl, or both, we have seen that the observed interfacial structure is delicately influenced by the solution composition. In the measurements so far, we have observed three distinct regimes of interfacial structure. First, at low proline concentrations, there was no distinct interfacial structure; a jump over several nanometres due to van der Waals attraction was instead measured. Second, at elevated proline concentrations, a repulsive wall due to adsorbed layers of zwitterions was measured at small surface separations. Third, for the compositions of the mixed proline-KCl solutions shown here, a structural contribution dominated by water layering was seen, akin to the hydration forces measured in dilute electrolytes containing KCl only.

Measurements of surface forces across KCl electrolytes at high enough concentrations can display structural features different to any of these previous regimes, as evidenced by the measurement across a significantly more concentrated KCl electrolyte (2.5 m) shown in Figure 4.6. Here, the structural forces have a length-scale of ~ 0.4 nm, which likely originates from salt-dominated layering in the interfacial

region. Similar measurements were observed for KCl solutions at concentrations greater than ~ 0.1 m. The switch from water (solvent)-dominated structural contributions to salt-dominated structural contributions has been frequently observed in other concentrated electrolyte solutions.[32,164] This phenomenon is closely connected to the Kirkwood line which defines the transition from a monotonic to an oscillatory decay of charge correlations in bulk electrolyte solutions.[131]

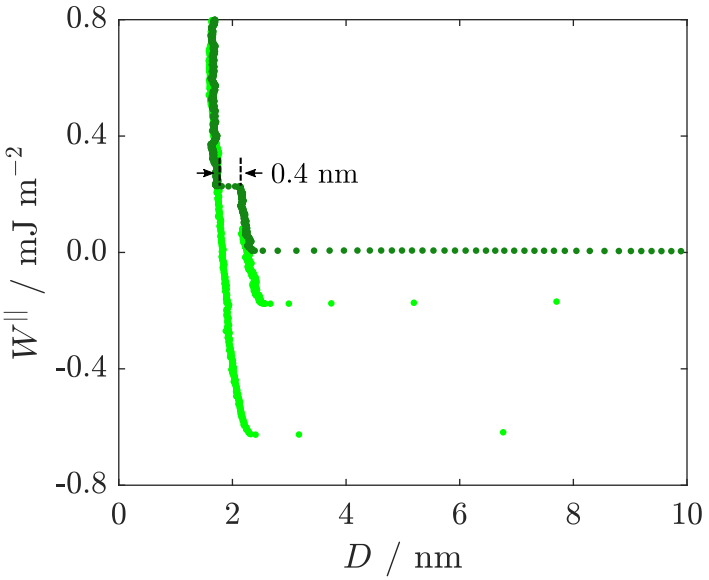

Figure 4.6: Measured interaction free energy as a function of surface separation across a solution containing 2.5 m KCl. The measurement upon approach of the surfaces is shown in dark green and that upon retraction is shown in light green. No DLVO fit is shown due to the small magnitude of the far-field repulsion observed in this measurement. This measurement was performed by Dr James Hallett.

Considering the structure away from the negatively charged surface, this oscillatory decay manifests as a layer of cations followed by a layer of excess anions, then excess cations, and so on. As the two surfaces are approached, therefore, electroneutrality is maintained by expelling a pair of cation and anion layers, and the size of this structural feature corresponds to such a pair of ion layers. This wavelength can be rationalised by considering the distance between two cation, or anion, planes in the rock salt crystal structure, which is $a/\sqrt{3}$ for a lattice constant a. This distance is 0.36 nm in the case of KCl;[165] similar to our observed wavelength, and deviation can be attributed to the hydration-driven swelling of the layers relative to that

expected for a pure molten salt.

Assimilating all of the structural regimes seen in our measurements, Figure 4.7 shows a phase diagram alongside schematic cartoons indicating the differing interfacial arrangement of water, ions and zwitterions for the four types of interfacial structures observed:

I. DLVO-only;

II. Zwitterion layering;

III. Water layering;

IV. Ion layering.

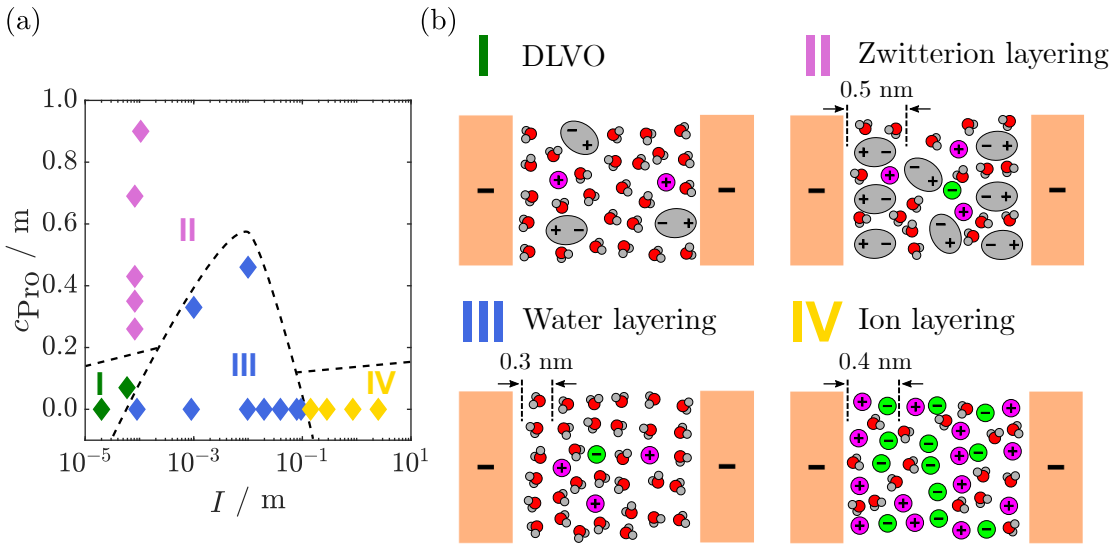

Figure 4.7: (a) Phase diagram summarising the range of proline and KCl concentrations at which different types of interfacial structure are seen. The marker colours refer to the type of interfacial structure observed. The salt concentration is reported as ionic strength I; for solutions with no added salt, an approximate concentration was estimated using the measured Debye length κ_D. Illustrative phase boundaries between the regimes of interfacial structure are shown by the dashed lines. (b) Schematic cartoons indicating possible interfacial arrangement of water, ions and zwitterions for the four observed types of interfacial behaviour. The behaviour at each composition has been observed to involve either: I) no structural force, or 'DLVO-like' behaviour (green data points); II) structural force due to zwitterion layering (pink data points); III) structural force due to water layering (blue data points); and IV) structural force due to salt layering (yellow data points).

4.4 | Surface Forces Measurements Across TMG Solutions

In order to investigate whether the results discussed so far are unique to proline, or qualitatively similar results can be observed for other zwitterions, in the following sections we present a series of results across solutions containing trimethylglycine (TMG). As previously, these solutions are investigated with and without additional KCl. All measurements presented in this section were performed in collaboration with Dr James Hallett.

4.4.1 | TMG-Only Solutions

Figure 4.8 displays two surface forces measurements across solutions containing only the zwitterion, TMG: one at a low concentration (0.07 m) and another at a higher concentration (0.75 m). These two measurements are highly analogous to the measurement across a low and high concentration proline electrolytes discussed earlier in this chapter (Figures 4.2 and 4.4). Firstly considering the low concentration case: the surfaces repel from large separations upon approach with the repulsion increasing in strength down to around 3 nm. At this point, a strong attractive force is observed resulting in a spring instability and a jump of the surfaces to small surface separations. Upon retraction, a deep attractive minimum is revealed, as shown in the inset to Figure 4.8 (a).

At the higher concentration, an additional step is observed at small separations before the smallest surface separation is reached upon approach. The size of this step is ~ 0.6 nm, corresponding closely with the end-to-end size of the TMG molecule,[166] and therefore this feature can again be attributed to the adsorption of TMG zwitterions at the mica interface. This can be thought of in an analogous manner to that of proline described earlier in this chapter, with the dipole moment - and the long axis - of the molecule aligned perpendicular to the interface.

The parameters associated with the DLVO fits to the long range repulsion for each of the two measurements are displayed in Table 4.7.

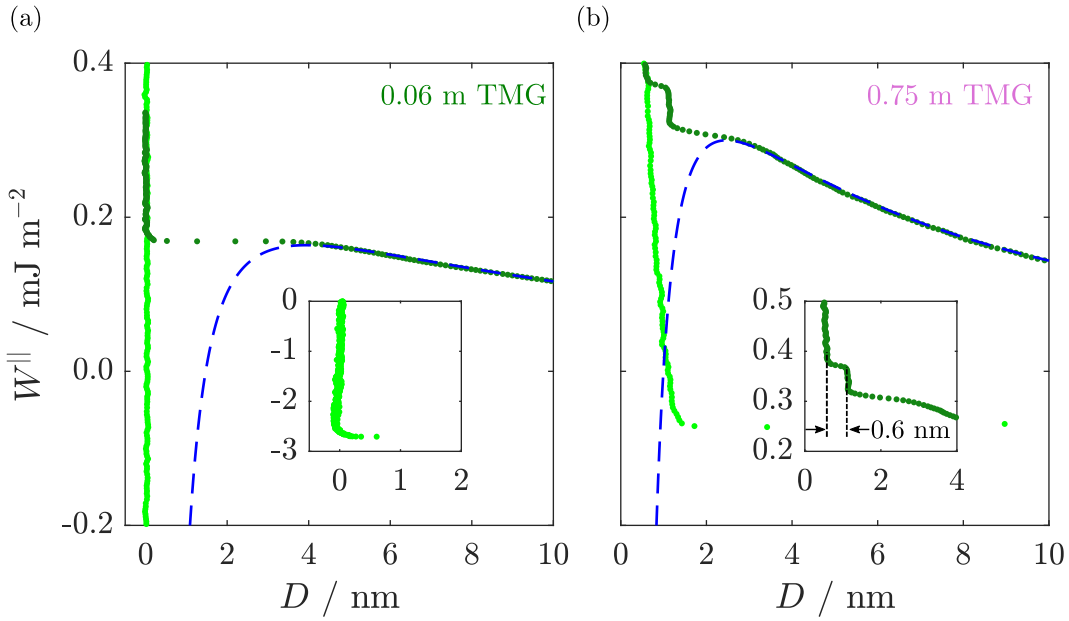

Figure 4.8: Measured interaction free energy as a function of surface separation across solutions containing: (a) 0.06 m and (b) 0.75 m TMG. Parameters for the DLVO fits are displayed in Table 4.7. (a) 0.06 m TMG shows 'DLVO-like' behaviour (Type I); the adhesive minimum observed upon retraction is shown in the inset. (b) 0.75 m TMG shows zwitterion layering (Type II); the inset shows a zoomed-in view of the structural features.

Table 4.7: Parameters obtained from the DLVO fits to the measurements of interaction free energy shown in Figure 4.8. The fitted effective surface potential ψ_{eff}, Debye screening length κ_{D}^{-1}, charge regulation parameter p and offset to the zero surface separation D_0 are shown.

c_{TMG}/ m	ψ_{eff} / mV	κ_{D}^{-1} / nm	p	D_0 / nm
0.06	44	21	0.79	0.0
0.75	39	23	0.91	0.0

4.4.2 | TMG-KCl Mixtures

Next, we show a series of measurements across three TMG-KCl mixtures of varying composition (Figure 4.9). The measurements displayed here were from solutions containing (a) 0.5 m TMG + 0.001 m KCl, (b) 2.88 m TMG + 0.13 m KCl and (c) 0.5 m TMG + 0.8 m KCl, and were chosen from the array of investigated concentrations to best illustrate the range of interfacial structures in these mixtures. The parameters associated with the DLVO fits for these measurements, where appropriate, are displayed in Table 4.8.

The first measurement (Figure 4.9 (a)) was performed across a solution contain-

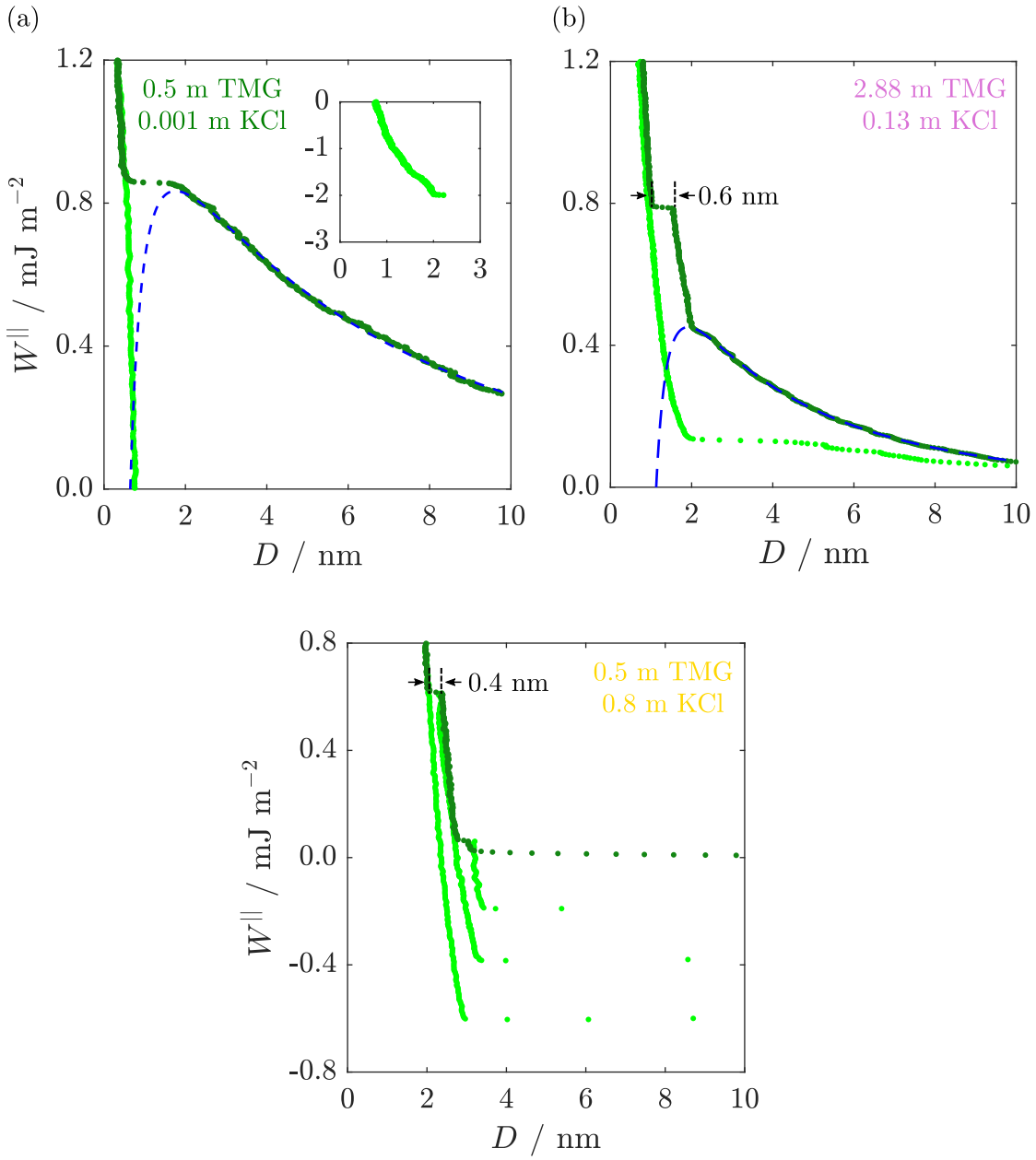

Figure 4.9: Measured interaction free energy as a function of surface separation made across a solution containing: (a) 0.5 m TMG + 0.001 m KCl; (b) 2.88 m TMG + 0.13 m KCl; and (c) 0.5 m TMG + 0.8 m KCl. Parameters for the DLVO fits are displayed in Table 4.8. (a) shows 'DLVO-like' behaviour (Type I), (b) shows zwitterion layering (Type II), and (c) shows ion layering (Type IV).

ing 0.5 m TMG and 0.001 m KCl. Here, the DLVO-like behaviour is observed, with no measured interfacial structure. By comparing this measurement to a salt-only case, such as that shown in Figure 3.4 in the previous chapter, we can observe that the presence of TMG acts to suppress the structural features due to water layering that would otherwise be seen.

Table 4.8: Parameters obtained from the DLVO fits to the measurements of interaction free energy shown in Figure 4.9. The fitted effective surface potential ψ_{eff}, Debye screening length κ_{D}^{-1}, charge regulation parameter p and offset to the zero surface separation D_0 are shown. The predicted Debye screening length $\kappa_{\text{D, pred}}^{-1}$ is also shown.

c_{TMG}/ m	c_{KCl}/ m	ψ_{eff} / mV	κ_{D}^{-1} / nm	p	D_0 / nm	$\kappa_{\text{D, pred}}^{-1}$ / nm
0.50	0.001	65	8.2	0.73	0.0	10.3
2.88	0.130	30	5.7	0.87	0.5	1.1

Further interplay between the zwitterions and salt can also be seen in the following two measurements. At high TMG concentrations, in Figure 4.9 (b), it is the TMG molecules that dominate the near-surface layering, with a structural feature of size $\sim$ 0.6 nm. In contrast, at higher salt concentrations in Figure 4.9 (c), salt layering is instead observed, with ion-dominated structural features of size $\sim$ 0.4 nm extending to separations of $\sim$ 4 nm.

Combined, this series of measurements across TMG-KCl mixtures further illustrate the interplay between zwitterions and ions in defining the total interaction profile. The measurements illustrate that TMG, like proline, can adsorb strongly at the mica surfaces, and in doing so, can frustrate the near-surface ordering of water molecules as observed in dilute KCl electrolytes. Furthermore, in solutions containing both TMG and KCl, the interfacial structure is influenced by the relative composition, and either zwitterions or ions can dominate the type of near-surface layering that is observed. A phase diagram for the interfacial structural regimes in TMG-KCl solutions, analogous to the one shown for proline-KCl solutions previously, is shown in Figure 4.10.

4.5 | Proline and TMG Comparison

The measurements presented in this chapter reveal a palette of colloidal stabilising strategies beyond mean-field DLVO interactions for both proline- and TMG-containing electrolyte solutions. Qualitatively, both zwitterionic osmolytes act to modify interactions in a similar manner. For instance, in the absence of salt both are observed to adsorb at charged surfaces when present at a sufficient concentration

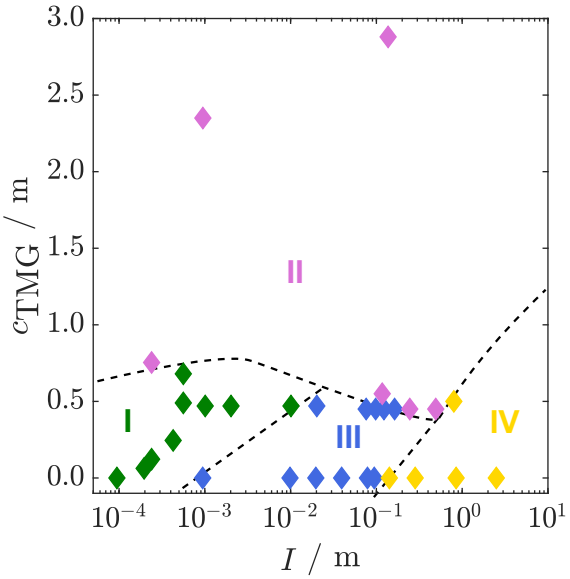

Figure 4.10: Phase diagram summarising the range of TMG and KCl concentrations at which different types of interfacial structure are seen. Data points are shown for all measurements presented up until this point in the thesis, along with additional measurements that are not presented in this work. The marker colours refer to the type of interfacial structure observed, using the same colour scheme as used in Figure 4.7: Type I - DLVO (green); Type II - zwitterion layering (pink); Type III - water layering; and Type IV - ion layering (yellow). Illustrative phase boundaries between the regimes of interfacial structure are shown by the dashed lines. The salt concentration is reported as ionic strength I; for solutions with no added salt, an approximate concentration was estimated using the measured Debye length κ_{D}.

and can act to enhance repulsive interactions relative to pure water. In the presence of salt, there exists an interplay between zwitterions and ions as observed in the resulting interfacial behaviour. At sufficient KCl concentrations, ions can displace zwitterions at the interfaces resulting in ion-induced water layering.

Despite the qualitative similarity, there do exist some quantitative differences that are worth examining further. The most notable of these are the concentration at which, in zwitterion-only solutions, the switch from DLVO-like (Type I) behaviour to zwitterion layering (Type II) behaviour is observed. For proline, this switch occurs at occurs at lower concentration than for TMG: the minimum concentration at which proline layering is observed is 0.26 m, whereas for TMG the minimum concentration was 0.75 m. If this concentration is deemed to be the point at which a complete monolayer of zwitterions has adsorbed onto the interface and the onset of multilayer formation, this suggests that proline has a greater affinity for surface adsorption

resulting in a more effective surface coverage.

Another quantitative difference can be seen in the enhancement of the far-field repulsion in the absence of salt, where proline appears to enhance the effective surface potential ψ_{eff} more strongly than TMG. The most direct comparison between the two sets of measurements is that at 0.07 m Pro, where the observed effective surface potential was $\psi_{\text{eff}} = 63$ mV, and 0.06 m TMG, where $\psi_{\text{eff}} = 44$ mV. This difference can be deemed to have the same origin as the previous observation; if proline has a greater propensity for surface adsorption than TMG, then employing the argument we made previously to rationalise the enhancement, proline would be expected to more effectively disrupt the Stern layer, replacing the cations and resulting in a more negative potential.

The structure of the zwitterions and their respective adsorption geometries likely account for both of these observed differences. We previously suggested that proline adsorbs with its pyrrolidine ring at the interface, pointing its carboxylate group away from the surface. This produces a larger surface coverage per molecule than TMG, which we suggest adsorbs with its trimethylammonium group at the surface. Each molecule of proline is therefore more effective at disrupting the ions that makeup the Stern layer, more significantly enhancing the negative surface potential relative to proline, and a lower concentration is required for complete surface coverage and therefore also the observation of multilayers through the additional step in the interaction profiles.

4.6 | Summary

In this chapter we have presented a series of measurements of interaction free energy across zwitterion-containing solutions, in order to investigate the role of these molecules in modulating interactions between charged surfaces. We investigate aqueous solutions containing two osmolytic zwitterions, L-proline and trimethylglycine, with and without added KCl.

The series of results across the proline-containing solutions demonstrate a clear link between proline and an enhanced electrostatic repulsion, revealing mechanistic detail for a stabilisation strategy against aggregation of biological particles in the cellular environment. Additionally, we find that the nature of the far-field component of the repulsion is rather insensitive to the cytosolic proline concentration. In other words, the repulsion appears to be regulated even as the proline concentration can be dialled up in response to osmotic stresses. By interpreting the results in the framework of the DLVO introduced in the previous chapter, we find that in low salt conditions the surfaces remain at constant charge due to the absence of free ions, but in the presence of salt the surfaces regulate their charge during approach. We illustrate that an interplay between the zwitterionic proline and free ions at charged interfaces allows for tuning of the overall interaction, determining the resulting near-surface structures as well as the longer-ranged interaction between particles.

By comparing these results to analogous TMG-containing solutions, in addition to TMG-KCl mixtures and a higher concentration KCl electrolyte, we find that in solutions containing both zwitterions and salt, the interfacial structure is carefully controlled by the relative solution composition. At high zwitterion concentrations, it is zwitterion-dominated structural features that are observed; whereas at high salt concentrations, ion-dominated structural features are instead observed. In more dilute solutions, there remains an interplay between zwitterions and ions, but instead it manifests in either water-dominated structural features being observed, or none at all. We interpret this to arise from the zwitterion-induced frustration of the near-surface ordering of water molecules that otherwise occurs in salt-only solutions. By comparing the results across proline and TMG solutions, we note that the switch to zwitterion layering occurred at lower concentrations for proline, and that proline was more effective at enhancing the surface potential in the absence of additional salt. Both of these observations can be rationalised by considering the greater surface

coverage per proline molecule than per TMG molecule.

Overall, this series of measurements reveals mechanisms behind the simultaneous tuning of intracellular interactions and osmoregulation. Interactions in these zwitterion-ion mixtures are complex and the palette of various DLVO and non-DLVO contributions can be tuned across the compositional phase space. These results have broad implications both in nature, for our mechanistic understanding of the role of zwitterions as osmolytes across the biosphere, and also in technology, for the development of salt-resistant crops in response to the increasing threat posed by salinisation of agricultural soils.

5 | Bulk Structure and Ion Effects in Zwitterion Solutions

5.1 | Background

Structural determination using scattering techniques has been of fundamental importance in the study of water and aqueous solutions.[167] In particular, neutron scattering has played a vital role in uncovering the molecular structure of water.[168,169] As we described in Chapter 2, the primary scattering interaction of neutrons is with the nuclei of the molecules in the sample of interest. This is in stark contrast to the use of X-rays in scattering studies, which interact with the electron clouds of water molecules, the distribution of which is easily polarized. Such studies involve complex interactions and it is difficult to reliably extract information regarding molecular arrangement. Scattering techniques have also been essential in monitoring perturbations to the structure of water upon the introduction of simple, monovalent ions into a solution,[170–172] and there are now also numerous studies looking at the effects of osmolytes on the structure of water, such as proline,[173] TMAO,[174] urea[175] and trehalose.[176]

However, there are relatively few studies considering the combined effects of molecular osmolytes and ionic species in a solution,[177] yet as we have discussed previously, biological environments contain complex mixtures of solutes, ranging in chemical complexity. Therefore, a model cytosol solution such as ours can begin to bridge this knowledge gap and elucidate understanding surrounding the combined role of, and potential synergies between, ionic and zwitterionic solutes. Furthermore, recent work has proposed a role for these zwitterionic osmolytes in preventing the salting out of proteins via the formation of ion-molecular associates.[178]

In this chapter, we present total scattering measurements performed on aqueous

mixtures of the osmolyte, TMG, and either potassium or sodium chloride, both of which are commonly found in the cytosol. These measurements reveal the impact of specific ions on various structural motifs within these solutions, such as TMG-ion pairs and TMG-TMG clusters, allowing us to further our understanding of the role of these zwitterionic osmolytes in maintaining biomolecule structure and function.

5.2 | Experimental and Simulation Details

We performed neutron and X-ray total scattering measurements on two aqueous electrolyte solutions. Each solution contained equimolar concentrations of trimethylglycine and either potassium or sodium chloride. The experimental and theoretical background to these measurement techniques, including the necessary simulation techniques required to interrogate the scattering data, were described previously in Chapter 2. The neutron total scattering was performed using the NIMROD instrument at the ISIS Neutron and Muon Source and the X-ray total scattering was performed using a Malvern Panalytical Empyrean diffractometer. Raw neutron scattering data are available in the ISIS Data Catalogue[179] and raw X-ray scattering data, in addition to Gudrun data reduction and Dissolve simulation files, are available from the Oxford University Research Archive.[180]

5.2.1 | Materials and Solution Preparation

As previously discussed, isotopic substitution is commonly employed in total scattering experiments to generate multiple total structure factors without significantly altering the structure of the system. This allows for the enhancement in the accuracy of the simulated structure. Specifically, in neutron scattering experiments of systems containing hydrogenous material, protium-deuterium substitution is commonly used owing to the highly contrasting neutron scattering lengths of the protium and deuterium isotopes of hydrogen ($b_{\mathrm{H}} = -3.74$ fm and $b_{\mathrm{D}} = 6.67$ fm).[181] The aqueous solutions of interest in this chapter contain two types of hydrogen atoms that can be

Table 5.1: The seven isotopic substitutions used to study each of the two aqueous solutions containing TMG and either KCl or NaCl. These seven solutions are required for an ideal two-site substitution, where the TMG and water hydrogen atoms are substituted.

Isotopic Substitution	TMG	Water
1	H-TMG	H_2O
2	H-TMG	D_2O
3	HD-TMG	HDO
4	HD-TMG	D_2O
5	D-TMG	HDO
6	D-TMG	H_2O
7	D-TMG	D_2O

readily isotopically substituted: those of the trimethylglycine molecules and those of the water molecules. TIn the ideal case for a two-site substitution, *i.e.* H/D substitution of the water and TMG hydrogen atoms, there are seven isotopic substitutions which must be used, outlined in Table 5.1. This set of substitutions allow the unique determination of the partial structure factors between the following three sets of atoms: the water hydrogen atoms, TMG hydrogen atoms and the remaining atomic sites in the system.[182,183]

The aqueous solutions were prepared by mixing a known mass of either or both of H-TMG (Sigma-Aldrich®, BioUltra, $\geq$ 99.0%) and D-TMG (ISIS Deuteration Facility); KCl (Thermo Scientific, Puratronic™, 99.997%) or NaCl (Thermo Scientific, Puratronic™, 99.998%); and ultrapure H_2O (18.2 MΩ cm), D_2O (Sigma-Aldrich®, 99.9 at% D), or HDO (a 1:1 molar mixture of H_2O and D_2O). Measurements were made at concentrations of 2 m TMG and 2 m salt. The molal concentration is only strictly defined for the solution containing only H_2O as the solvent; solutions containing D_2O were made at an equivalent molar ratio between all of the components in the solution containing only H_2O.

These solutes and concentrations were carefully chosen as a compromise between ideal physiological conditions and experimental practicality: higher concentrations are required to obtain a good scattering signal from the solutes and the requirement

to simulate a representative model of the system. Nevertheless, while the concentrations of the individual solutes are higher than those found in typical cytosol, they are found more widely in the most strongly halophilic organisms, such as in the examples provided in previous chapters.

For the neutron scattering measurements, the solution samples were transferred to flat, null scattering alloy cans ($Ti_{0.68}Zr_{0.32}$) of 1 mm thickness, and sealed with PTFE before being loaded onto a sample changer on the NIMROD instrument. For the X-ray scattering measurements, the solution samples were transferred to silica capillaries and sealed with beeswax.

5.2.2 | Solution Densities

Knowledge of the atomic density of the solutions is necessary in order to simulate a model box of the solution. The mass density of the two solutions containing only H_2O as the solvent was measured using the method described in Chapter 2 and from this value the atomic density of each solution was calculated. The density values are displayed in Table 5.2.

Table 5.2: Measured mass and atomic densities of the two aqueous solutions containing TMG and either KCl or NaCl.

Solution	ρ / g cm^{-3}	ρ / atoms Å^{-3}
2 m H-TMG + 2 m KCl (H_2O)	1.0978	0.09967
2 m H-TMG + 2 m NaCl (H_2O)	1.0897	0.10129

5.2.3 | Simulation Details

The Dissolve package was used to simulate and refine the structure of a model box of the two liquid solutions, at equivalent composition and densities to the experimental solutions. Each box contained 9330 water molecules and 340 of each of the solute species (trimethylglycine, potassium or sodium cation, and chloride anion), in a cubic box of side length 70.3 Å. This box size was deemed appropriate as a

compromise between enhanced statistics on the one hand, and on the other, greater computing power required for larger box sizes. When generating a simulation box for this purpose, an additional consideration is the limit on the length scale over which structural correlations can be calculated. The method used in this work places a limit on the maximum length scale at half the box side length; our simulated box is of a large enough size to investigate all of the structural correlations of interest.

As discussed previously, the Dissolve package requires a classical molecular dynamics forcefield to be applied to each of the species in the simulation. For the water molecules in our simulation, we use the flexible single point-charge water model (SPC/E).[184] For the TMG molecules, we extract a forcefield using the LigParGen tool, which provides bond, angle, dihedral and Lennard-Jones OPLS-AA parameters, as well as partial atomic charges.[185–187] The forcefield for the K^+, Na^+ and Cl^- species was obtained using Equation 2.22 for the simplest intermolecular potential - comprising the sum of a Lennard-Jones and a Coulomb term - that was outlined in Chapter 2. The parameters for this potential were obtained from literature neutron diffraction studies on aqueous solutions of KCl and NaCl, which are displayed in Table 5.3.[171]

Table 5.3: Lennard-Jones and Coulomb parameters for the K^+, Na^+ and Cl^- species in the Dissolve simulations.[171]

Species	ϵ / kJ mol^{-1}	σ / Å	q / e
K	0.5144	2.94	1
Na	0.5144	2.29	1
Cl	0.566	4.191	-1

The refined simulations were used to perform subsequent analysis routines, including calculating radial and spatial distribution functions. Rather than performing these calculations over a specific snapshot of the refined simulation, they were performed over a trajectory of 10,000 frames. The resulting analysis therefore reflects a wide range of snapshots that are all valid solutions to the EPSR fitting process.

5.3 | Bulk Structure Measurements and Discussion

The experimentally measured neutron and X-ray structure factors and their associated simulated fits for the two solutions are displayed in Figure 5.1. Analogous figures for the measured and simulated total radial distribution functions $G(r)$ are displayed in Appendix B (Figure B.1). The overall quality of fit between the measured and simulated structure factors is reported in Dissolve as an R-factor, a weighted sum of the squared residuals, where a lower value represents a better quality fit. The final R-factors for the fits were 0.0007 and 0.0017 for the KCl- and NaCl-containing solutions, respectively, which represent good agreement for both simulations. In a number of the neutron structure factors, there are some discrepancies between the experimental and simulated datasets in the low-Q region, as illustrated in the difference functions displayed in Appendix B (Figure B.2). These differences most likely due to errors in the corrections performed to the scattering data in the Gudrun packages; a potential source of these errors may be found in the inelasticity corrections which are particularly difficult to calculate accurately, especially in samples such as these which contain large amounts of hydrogen.[188]

The good agreement between the simulated and experimental structure factors signifies that the structure of the liquid in the simulation box is an accurate representation of the liquid structure, allowing for the interrogation of further specific structural features and correlations between constituent components of the liquid. A snapshot of the refined configuration of the solution containing TMG and KCl is shown in Figure 5.2.

5.3.1 | Bulk Water Structure

To begin with, we consider the structure of the water network in our solutions and the perturbations to the structure of pure water due to the presence of additional solutes in the studied solutions. Structure and interactions within the liquid can be analysed using the radial distribution function - RDF, or $g(r)$ - a function that

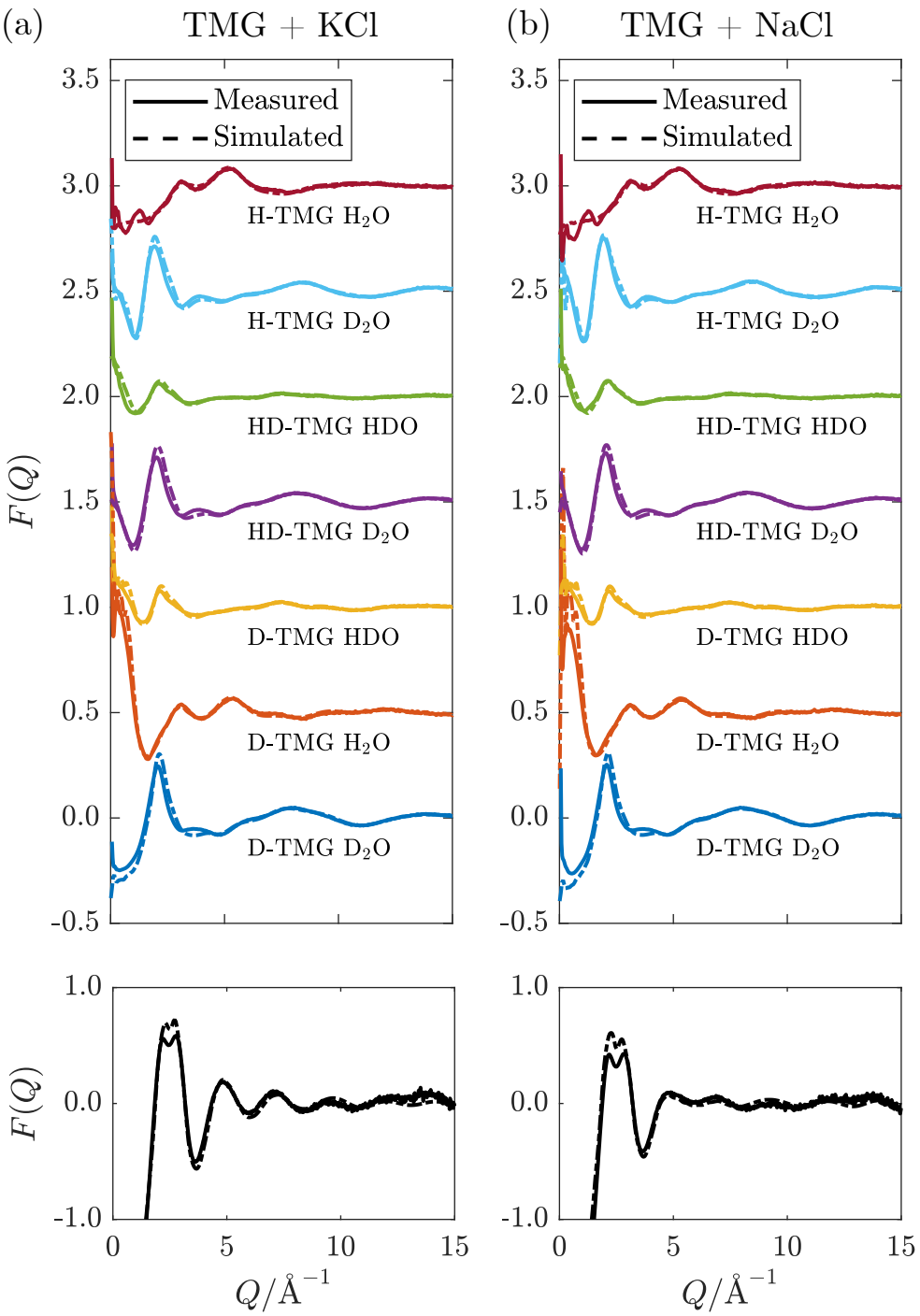

Figure 5.1: Measured (solid lines) and simulated (dash-dotted lines) structure factors $F(Q)$ for aqueous solutions containing (a) TMG + KCl and (b) TMG + NaCl (right). Top: Structure factors obtained from neutron diffraction in seven isotopic contrasts; each dataset is vertically shifted by 0.5 for clarity. Bottom: Structure factor obtained from X-ray diffraction.

describes the likelihood of finding an atom of type B at a distance r from a reference atom A, normalised by the mean density of the system. The RDFs that describe the

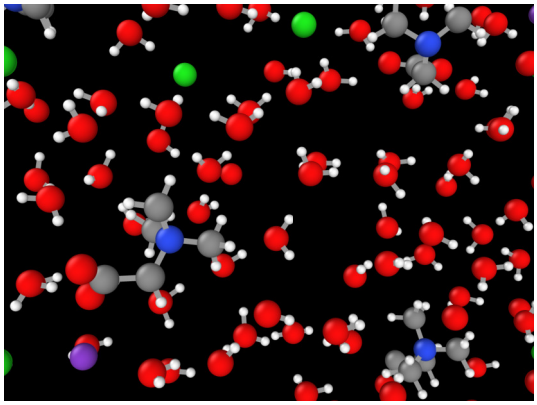

Figure 5.2: Snapshot from the refined configuration of the TMG and KCl solution. Atom types: C - grey; H -white; O - red; N - blue; K - purple; Cl - green. Atomic radii are not to scale.

intermolecular correlations between water molecules in both KCl and NaCl solutions are shown in Figure 5.3 alongside literature data for pure water.[189] The differences between the calculated RDFs for the KCl- and NaCl-containing solutions appear negligible. The figures each display two RDFs that are significant for characterising water-water correlations. The first is calculated from one oxygen atom to another oxygen on a different water molecule, indicative of the correlations between the centres-of-mass of water molecules; the second considers correlations between the oxygen atoms of a reference water molecule and the hydrogen atoms of surrounding molecules, and is informative about the hydrogen bonding structure between water molecules.

The primary peak in the O_w-O_w RDF is insensitive to the addition of the solutes - located at 2.8 Å in both pure water and our measurements - and is consistent with previous literature measurements of salt-containing solutions[170] and molecular osmolytes including proline.[173] More notable is the disruption to the secondary peak, located at 4.5 Å in pure water but not discernable in the measurements of our solutions. A variety of effects upon this second O_w-O_w peak have been observed upon addition of solutes to aqueous solutions. In some instances, most notably upon the addition of monovalent salts,[170,172] there is a marked inwards shift of this peak; to which an equivalence is made to the compression of water structure upon

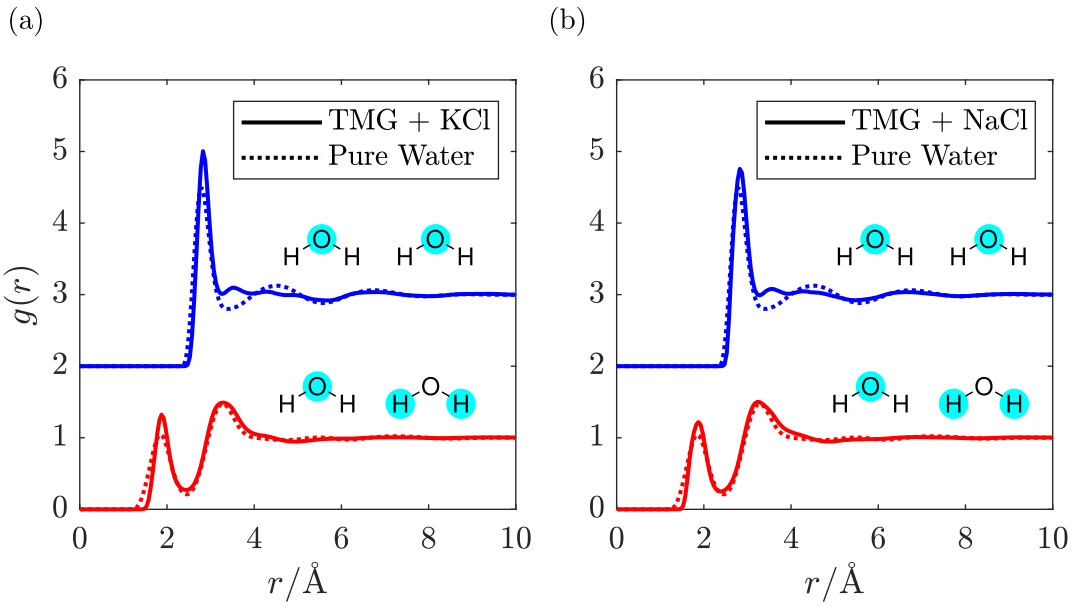

Figure 5.3: Intermolecular RDFs $g(r)$ for correlations between atomic sites in H_2O for: (a) the TMG + KCl solution and (b) the TMG + NaCl solution. In each case, the O_w-O_w (blue) and O_w-H_w (red) correlations are shown. The correlations present in pure water are shown as dotted lines, reproduced from Soper.[189] Only correlations between atoms in different water molecules contribute to the displayed functions. For clarity, the functions have been vertically shifted.

the application of a large external pressure.[190,191] A similar inward shift of this second peak was also observed upon the addition of TMG on its own to an aqueous solution,[192] in contrast to the observation made upon the addition of TMAO which was able to resist these pressure or salt-induced perturbations to the structure of water, shifting this peak outwards to larger distances.[177,193] It is difficult to discern a second peak in our case, similar to the flattening of the peak observed for solutions containing other large solutes such as proline or *tert*-butyl alcohol.[173,194] Consistent with these previous studies, we do not notice any significant changes to the O_w-H_w RDF relative to pure water upon addition of the solutes. This RDF has a primary peak at 1.9 Å, corresponding to the length of the hydrogen bonds between water molecules. Overall, this set of RDFs are indicative of a water hydrogen bond network that remains intact but is distorted due to an insufficient number of water molecules present to form a coordination shell beyond the first without other species also present.

Further characterisation of the bulk water structure can be performed by calculating the water dipole angle distribution of molecules around a reference water molecule. In the context of the bulk water structure, one can calculate the distribution of water dipole angles hydrating a central, reference water molecule. This angle is defined as that between the vector connecting the oxygen atom of a reference water molecule and the oxygen of a hydrating water molecule, and the vector corresponding to the dipole moment of the water molecule. The distribution is presented in Figure 5.4. It is clear that this distribution is bimodal: there is one peak centred on a dipole angle of 48.5° and a second, broader peak centred on 147.5°. The peak at the smaller angle corresponds to the central water molecule accepting a hydrogen atom from a surrounding molecule, and that at the larger angle corresponds to the central molecule donating a hydrogen to a surrounding water. This bimodal distribution is therefore consistent with water molecules being both hydrogen bond-acceptors and donators, and an analogous distribution for pure water would be expected.

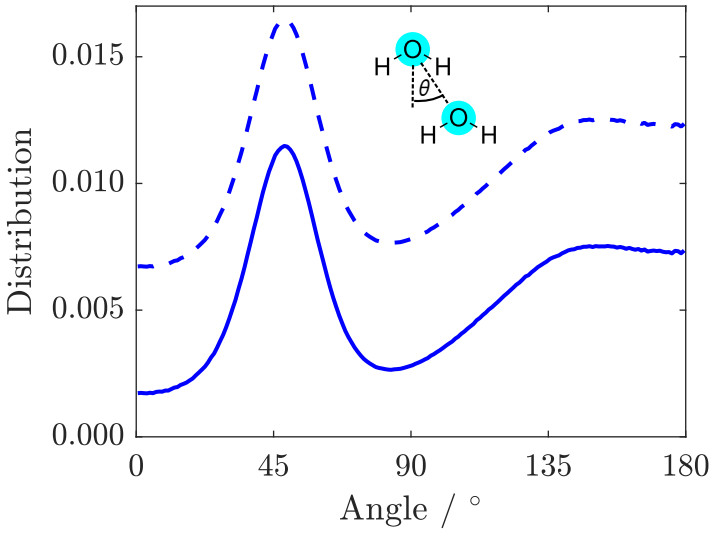

Figure 5.4: Distribution of the dipole angles for water molecules hydrating a reference water molecule. This angle is defined as the angle between the vector connecting the oxygen atom of a reference water molecule and the oxygen of a hydrating water molecule, and the vector corresponding to the dipole moment of the water molecule. Distributions are shown for the TMG + KCl (solid line) and TMG + NaCl (dashed line) solutions, which are shifted for clarity.

The water self-coordination numbers also yield a valuable insight into the water

network. These and all other coordination numbers in this chapter were calculated using the Dissolve package, by spherically integrating the RDF $g_{\alpha\beta}(r)$ for site β around site α between the limits r_1 and r_2, as described by Equation 5.1:

$$N_{\alpha}^{\beta} = \rho \int_{r_1}^{r_2} 4\pi r^2 g_{\alpha\beta}(r) dr \tag{5.1}$$

where N_{α}^{β} is the coordination number of atom β around a central atom α, ρ is the number density of atom type β and $g_{\alpha\beta}$ is the radial distribution function (RDF). In all analysis performed in this chapter, the lower limit of integration r_1 was set to zero and the upper limit r_2 was set to the radial cutoff, the distance at the first minimum in the relevant radial distribution function, as required to perform the calculation across the first coordination shell.

In the coordination number analysis performed in this work, the error in the mean is small owing to the large number of simulation snapshots that contribute to its calculation. This error is approximately 0.01 for all coordination numbers; all values are reported to two decimal places to reflect this accuracy. Additionally, for most coordination number distributions, it is also possible to determine their standard deviations, a measure of the width of the distribution. These are reported alongside the mean coordination number where appropriate; however, for coordination numbers smaller than one it is not meaningful to calculate a standard deviation as they are not symmetrical distributions, and they are not reported in these cases.

The water self-coordination numbers, calculated using the O_w-O_w RDF and a cutoff of 3.4 Å, are displayed in Table 5.4. The water self-coordination numbers are clearly reduced in the presence of solutes relative to pure water; the deviation can likely be attributed to the fact that the TMG molecules are relatively large and the concentration of both the TMG and salt solutes are quite high, thus lowering the number of water molecules solvating another water molecule, consistent with our conclusions from our studying of the water-water RDFs.

Table 5.4: Comparison of the water self-coordination numbers in the KCl- and NaCl-containing solutions, calculated from the O_w-O_w RDFs in Figure 5.3. †The pure water coordination number is reproduced from Soper.[189]

Solution	Coordination Number	Cutoff r / Å
Pure water†	4.67	3.4
TMG + KCl	3.99 (1.19)	3.4
TMG + NaCl	4.10 (1.16)	3.4

5.3.2 | TMG Hydration Structure

We now turn to study the solute-solvent interactions in our solutions, analysing first the hydration structure of our osmolyte, TMG. The unique hydration structure of TMG resulting from its antagonistic dipolar and hydrophobic properties is thought to contribute to its stabilising effect on biomolecules.[195] We consider correlations between TMG and surrounding water molecules, centred on two contrasting sites on the osmolyte molecule: first, the anionic, carboxylate group, where correlations are calculated from the carboxylate oxygen atoms (O); and second, the cationic, quaternary ammonium group, where correlations are calculated from the methyl carbon atoms (C_m).

Considering first the carboxylate-water interactions, the O-O_w and O-H_w RDFs are displayed in Figures 5.5 (a) and (b), respectively. As expected from a negatively charged, hydrophilic carboxylate group, our RDFs illustrate a strong hydrogen bonding environment, with a well-defined, sharp peak in both the O-O_w and O-H_w RDFs. The primary peak in the O-H_w RDF is located at 1.8 Å, the hydrogen bond distance between TMG and water. This hydrogen bond is shorter than that observed between water molecules (shown in Figure 5.3), which suggests that the interaction between TMG and water is potentially slightly stronger than the hydrogen bonds between water molecules themselves in this solution. This increase in strength can be attributed to the negatively charged carboxylate oxygens, and has been observed in previous neutron scattering structural studies of aqueous solutions containing osmolytes including both TMAO or TMG.[174,192,196]

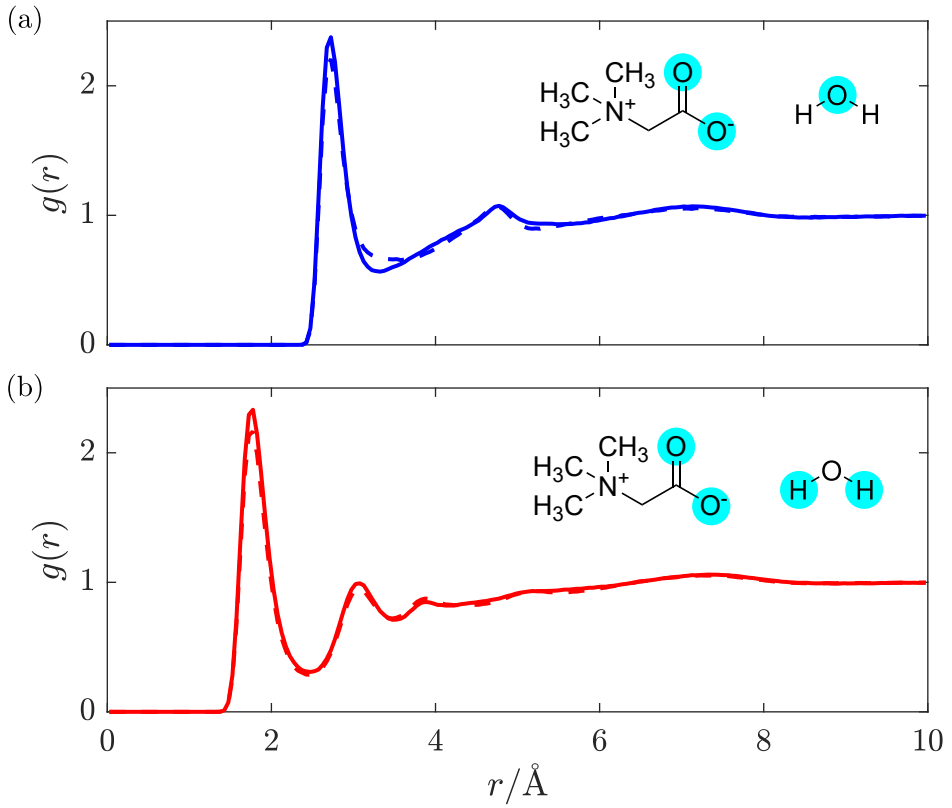

Figure 5.5: (a) O-O_w and (b) O-H_w RDFs, shown for the TMG + KCl (solid line) and TMG + NaCl (dashed line) solutions. (Note, the solid and dashed line are almost exactly on top of each other for both panels.)

Next, we consider the trimethyl ammonium-water interactions. The calculated C_m-O_w and C_m-H_w RDFs are displayed in Figures 5.6 (a) and (b), respectively. These RDFs display clear peaks, although the primary peaks - located at 3.6 Å for C_m-O_w and 3.9 Å for C_m-H_w - are notably broader than those in the carboxylate-water RDFs. Although the two RDFs are more qualitatively similar than those presented for the carboxylate oxygen analogues, the slight difference in the primary peak position implies a net favourable orientation of water molecules to point their oxygen atoms towards the methyl group. This observation suggests that the water molecules are somewhat oriented due to the presence of the positive charge on the TMG nitrogen atom, and as such the interaction between the TMG quaternary ammonium group and surrounding water molecules is not purely hydrophobic at this moiety. Similar observations have been made previously in molecular dynamics simulations of aqueous TMG solutions.[195,197] This difference implies that the water

molecules surrounding the carboxylate group are more strongly ordered than those surrounding the methyl groups: something that is to be expected between more hydrophilic or hydrophobic regions of an osmolyte molecule.

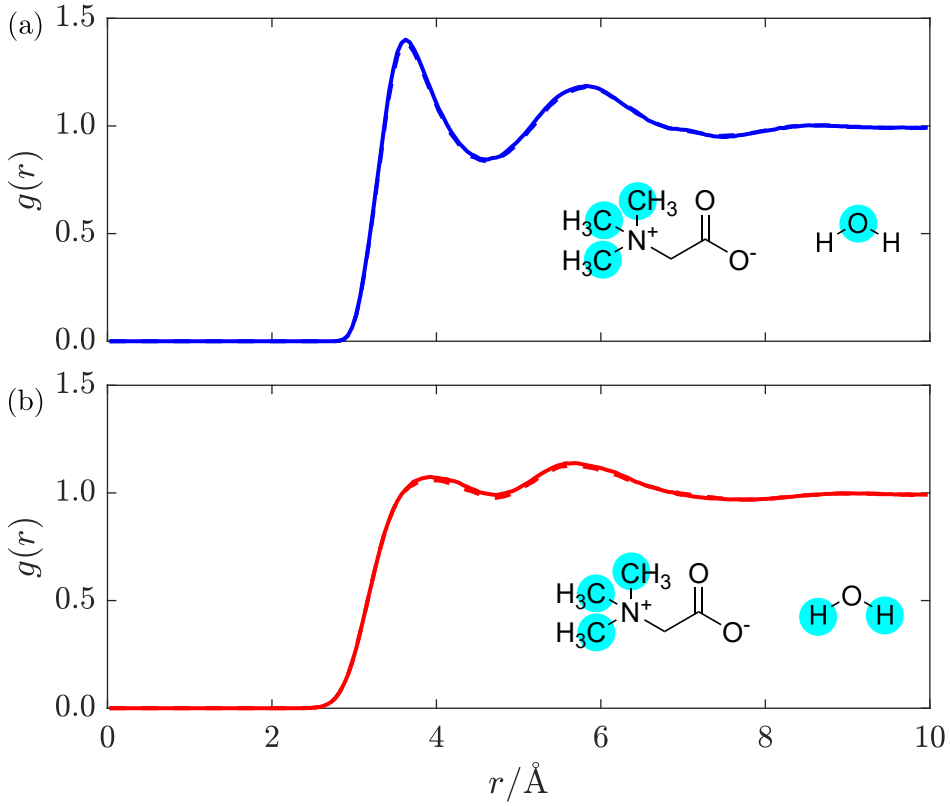

Figure 5.6: (a) C_m-O_w and (b) C_m-H_w RDFs, shown for the TMG + KCl (solid line) and TMG + NaCl (dashed line) solutions. (Note, the solid and dashed line are almost exactly on top of each other for both panels.)

The TMG hydration coordination numbers calculated from both sets of TMG-H_2O RDFs in Figures 5.5 and 5.6 are displayed in Table 5.5.

Table 5.5: TMG-water coordination numbers in the KCl- and NaCl-containing solutions calculated from the RDFs in Figures 5.5 and 5.6.

Environment	Coordination Number	Cutoff r / Å
O-O_w (KCl)	2.67 (0.84)	3.3
O-O_w (NaCl)	2.70 (0.86)	3.3
C_m-O_w (KCl)	7.72 (1.55)	4.6
C_m-O_w (NaCl)	7.75 (1.57)	4.6

This orientational geometry can be further interrogated by calculating the water dipole angular distribution for the hydrating water molecules at the two sites, which are displayed in Figure 5.7 and are analogous to the distribution in the previous section when we were considering water-water interactions. In these distributions, the angle is calculated between one vector connecting an atomic site on the TMG molecules - either the carboxylate oxygen or the methyl carbon - and the oxygen of a water molecule, and another vector directing along the water dipole moment. Again, only water molecules located at smaller distances than the first minimum on the TMG-water RDF contribute to the distribution.

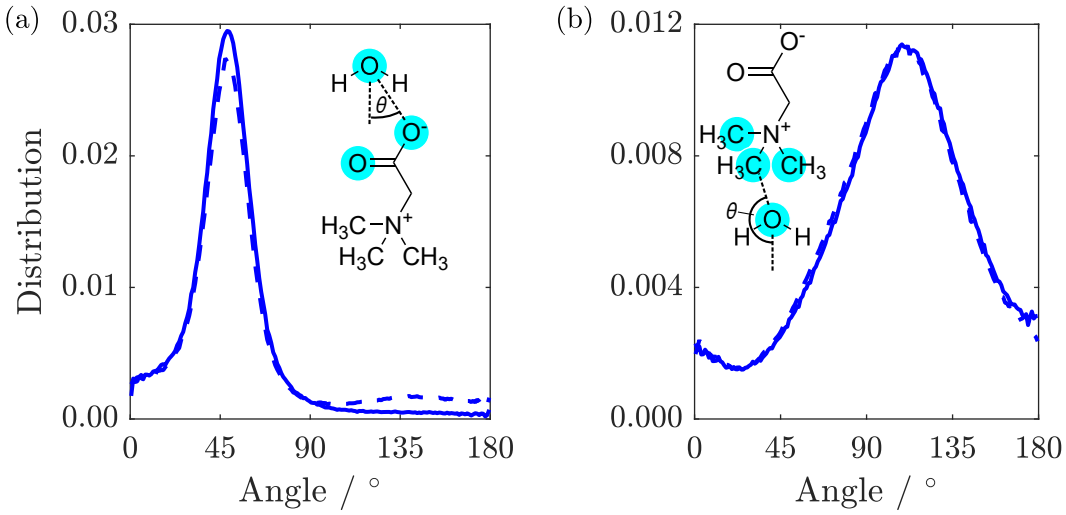

Figure 5.7: Distribution of the dipole angles for water molecules hydrating (a) the TMG carboxylate group or (b) TMG methyl group. This angle is defined as the angle between the vector connecting (a) a carboxylate oxygen or (b) methyl carbon and the hydrating water molecule, and the vector corresponding to the dipole moment of the water molecule. Distributions are shown for the TMG + KCl (solid line) and TMG + NaCl (dashed line) solutions.

In Figure 5.7 (a), the distribution contains a single sharp maximum located at 47.5°, characteristic of the hydrogen bond-accepting properties we inferred from the TMG-H_2O RDFs (Figures 5.5 and 5.6) and that we might expect for a negatively charged, hydrophilic moiety. This peak is indicative of a hydrating water molecule geometry where it is pointing one of its hydrogen atoms towards the carboxylate oxygen. It is worth comparing these results to the analogous distribution for the

water-water interactions we displayed previously in the discussion of the bulk water structure. That distribution (Figure 5.4) contained two peaks rather than the single peak seen here. This difference can simply be ascribed to the water molecules acting as both hydrogen bond-donators and acceptors where the TMG carboxylate group can only accept hydrogen bonds. However, we also note a small peak at $\sim$140° for the NaCl system, which is not the case for KCl. We will return to this later, after considering the TMG-ZCl interactions.

Turning to the water dipole angle distribution around the methyl group in Figure 5.7 (b), the distribution again contains a single peak, but it is instead located at an angle of 109.5° and is much broader. As we inferred from the TMG-H_2O RDFs, despite the more hydrophobic nature of the methyl groups there is still some ordering of the hydrating water molecules around this region of the TMG molecules owing to the positive charge on the nitrogen atom. This angular distribution is consistent with this picture as it suggests that the water molecules orient their hydrogen atoms away from these methyl groups, instead orienting their oxygen electron density towards to the positively charged region of the zwitterion. The increased width of the distribution relative to the carboxylate analogue can be easily explained through the fact that this functional group would not be expected to hydrogen bond with the surrounding water molecules, and as such there is much more disorder present in this angular distribution.

The RDFs presented in this section are largely similar in nature when compared to the literature results with no salt present. It is clear, therefore, that the presence of salt in the solution does not have significant implications for the hydration of TMG, and the osmolyte is able to retain its hydration shell even at high concentration, in agreement with predictions from simulation.[178]

5.3.3 | Ion Hydration Structure

The next structural aspect of our solution that we will consider will be the hydration structure of the monovalent ions in our solutions, namely potassium or sodium cations and chloride anions. We will begin this aspect of the structural interrogation by considering the RDFs calculated between the cation Z (either K or Na) and the water oxygen and hydrogen, displayed in Figure 5.8 (a); and equivalently for the chloride anion in both solutions, displayed in Figure 5.8 (b).

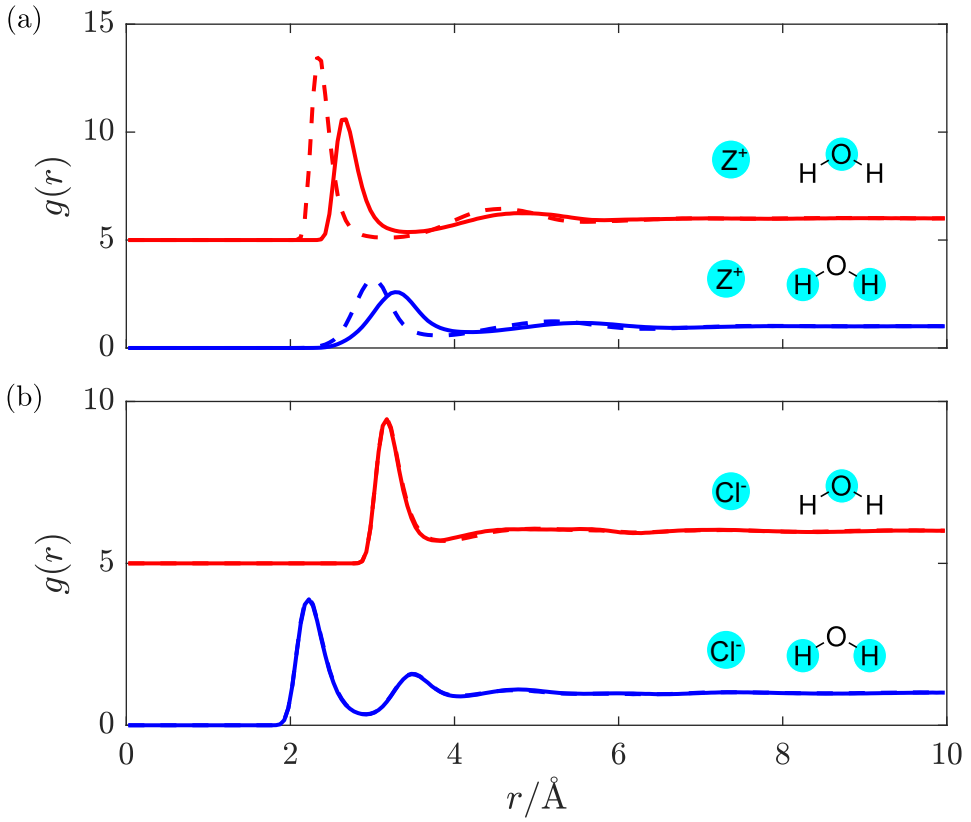

Figure 5.8: (a) Cation-water and (b) anion-water RDFs, shown for: $Z^+ = K^+$ (solid line) and $Z^+ = Na^+$ (dashed line). The RDFs calculated between the ions and O_w are shown in red and H_w in blue; these functions have been shifted for clarity. The anion-water RDFs in (b) are almost completely overlapping for $Z^+ = K^+$ and Na^+.

The ion-water RDFs are consistent with the results obtained from structural studies upon aqueous solutions containing only monovalent ions from Mancinelli *et al.*[171] The position of the primary peak in the K-O_w RDF can be found at 2.7 Å, and at 2.3 Å in the Na-O_w RDF. Similarly, the position of the primary peak in the Cl-H_w

RDF can be found at 2.2 Å. In their work, Mancinelli *et al.* observe that the primary peak position of these RDFs is insensitive to the ion concentration, even if the peak intensity and water coordination number is indeed sensitive to concentration. Our results are consistent with this, and demonstrate that these peak positions are also insensitive to additional osmolyte co-solutes present in the solution. From Figure 5.8 (b), it is clear that the hydration structure of the chloride anion is unaffected by the identity of the cation.

All cation- and anion-water coordination numbers are displayed in Tables 5.6 and 5.7, which satisfactorily reproduce the weakly concentration sensitive results reported by Mancinelli *et al.*[171]

Table 5.6: Cation-water coordination numbers in both the KCl- and NaCl-containing solutions calculated from the RDFs in Figure 5.8 (a). Water oxygen-cation (O_w-Z) coordination numbers are also displayed for later comparison with TMG oxygen-cation interactions.

Environment	Coordination Number	Cutoff r / Å
O_w-K	0.20	3.5
O_w-Na	0.18	3.2
K-O_w	5.58 (1.26)	3.5
Na-O_w	4.86 (1.21)	3.2
K-H_w	16.04 (2.34)	4.1
Na-H_w	12.34 (2.31)	3.7

Table 5.7: Anion-water coordination numbers in both the KCl- and NaCl-containing solutions calculated from the RDFs in Figure 5.8 (b).

Environment	Coordination Number	Cutoff r / Å
Cl-O_w (KCl)	6.59 (1.16)	3.8
Cl-H_w (KCl)	6.08 (1.19)	2.9
Cl-O_w (NaCl)	6.87 (1.04)	3.8
Cl-H_w (NaCl)	6.25 (1.11)	2.9

Further analysis of the ion hydration structures can be performed by calculating the water dipole angle distribution of molecules hydrating a central ion. This

distribution was calculated for all ion species - K^+, Na^+ and Cl^- - by considering all of the hydrating water molecules in the first coordination shell of each ion. The results for the potassium and sodium cations are displayed in Figure 5.9 (a), and those for the chloride anions in Figure 5.9 (b). Comparing the distribution for the two cations, we find a tighter distribution in the case of Na relative to that of K, implying a more disordered hydration structure around the K cation than for Na.

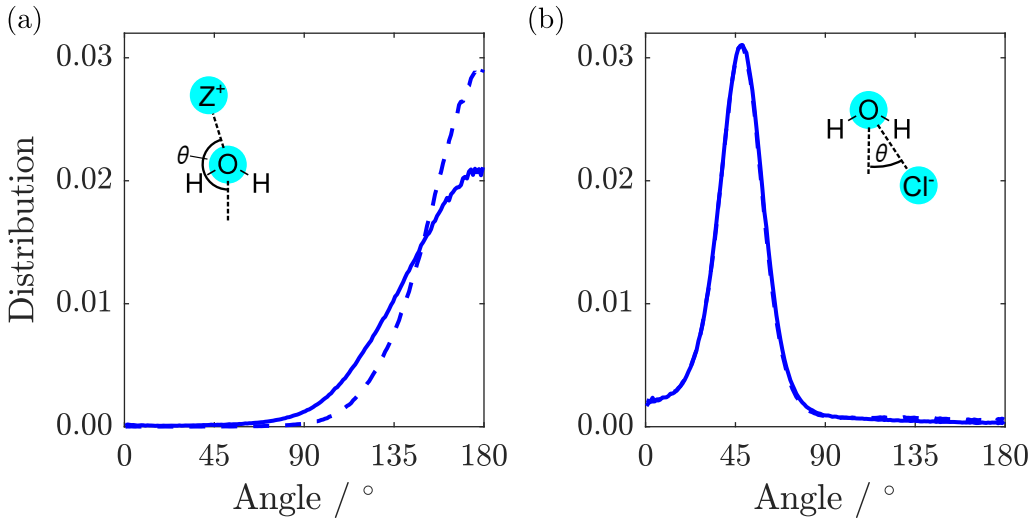

Figure 5.9: Distribution of the dipole angles for water molecules hydrating a central potassium or sodium cation (a) or chloride anion (b) within the first hydration shell of the ions. Data for the KCl- and NaCl- containing datasets are shown with solid and dashed lines, respectively. This angle is defined as the angle between the vector connecting the ion and the hydrating water molecule, and the vector corresponding to the dipole moment of the water molecule.

Combined, these results imply a difference in the hydration structures of the K and Na cations. Similarly to literature results, we find a tighter, more ordered distribution of water molecules surrounding the Na cation relative to that of the K cation which has a more disordered hydration structure, owing to the differences in ionic radii and charge density of the two ions. The sodium ion is smaller than the potassium, allowing water to approach more closely and giving rise to a more tighter coordination and thus a narrower angle distribution.

With regard to the hydration of the chloride anions, both the chloride-water RDFs (Figure 5.8) and the water dipole angle distribution in the first hydration

shell (Figure 5.9), it is evident that the structure of the hydration shell is largely independent of the cation, whether it be potassium or sodium. In both cases, the water dipole angle distribution has a maximum at 47.5°, as would be expected for a water molecule which is pointing its hydrogen atoms towards the hydrated ion and equivalent to that at the maximum of the dipole angle distribution for water molecules hydrating a TMG carboxylate oxygen atom in Figure 9.

5.3.4 | TMG-Ion Binding

Next, we will concentrate on the nature of association of the cationic species in our solution and the TMG osmolyte molecules. RDFs illustrating correlations between the TMG oxygen atoms (O) and the potassium or sodium cations (Z^+) are displayed in Figure 5.10. The sharp primary peak for both cations, located at 2.6 Å for the O-K RDF and 2.3 Å for the O-Na RDF illustrate a strong coordination between the TMG oxygen and the solution cations. These RDFs are largely reminiscent of the Z-O_w RDFs we presented earlier in this chapter (Figure 5.8), showing an initial peak that is taller and at smaller distances in the O-Na RDF relative to the O-K RDF: a difference that can again be attributed to differences in the ionic radii of the two cations. The relevant coordination numbers obtained from these TMG-ion RDFs are reported in Table 5.8 and reveal similar numbers for both cations. The taller peak in the O-Na RDF is therefore indicative of a tighter distribution for the coordination of Na^+around the TMG carboxylate group relative to the analogous K^+ coordination.

Table 5.8: Comparison of the TMG oxygen-cation (O-Z) coordination numbers in both the KCl- and NaCl-containing solutions calculated from the RDFs in Figure 5.10.

Environment	Coordination Number	Cutoff r / Å
O-K	0.31	3.5
O-Na	0.34	3.2
K-O	0.54	3.5
Na-O	0.75	3.2

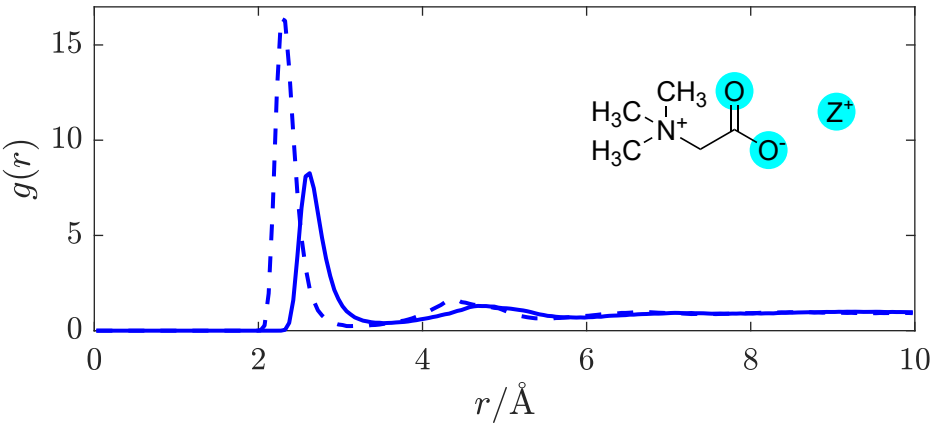

Figure 5.10: TMG oxygen-cation (O-Z) RDFs. The O-K (solid line) and O-Na (dashed line) distributions are shown.

Whilst the TMG O-Z RDFs illustrate a well defined coordination of cations to the oxygen atoms, the coordination numbers of ~ 0.3 for both cations appear to illustrate that this coordination is not strongly favoured. However, carboxylate oxygens are outnumbered by water oxygens by 14 to 1, which themselves have a coordination number of ~ 0.2 for both cations - displayed previously in Table 5.6 - thus demonstrating a preference for TMG-cation coordination compared to pure hydration.

We note greater distinction between the two cationic species by considering the Z-O coordination number. K^+ has a CN of 0.54 with the TMG oxygen compared to 0.75 for Na^+. Given the similarity between the O-Z coordination numbers for the two cationic species, this suggests either that the sodium ions are more likely to coordinate to both TMG oxygens at the same time (*i.e.* bidentate coordination) than potassium, or that they are more likely to be shared between two TMG molecules.

In order to differentiate between monodentate and bidentate coordination, in Figure 5.11 we display the distribution for the angle formed between a vector directing from the cation to the centre of mass of the two carboxylate oxygen atoms, and another vector directing from this centre to the carboxylate carbon atom. This distribution was calculated for all cations found within distances from carboxylate oxygen atoms up to the first minimum in the O-Z RDFs (Figure 5.10). Both K^+ and

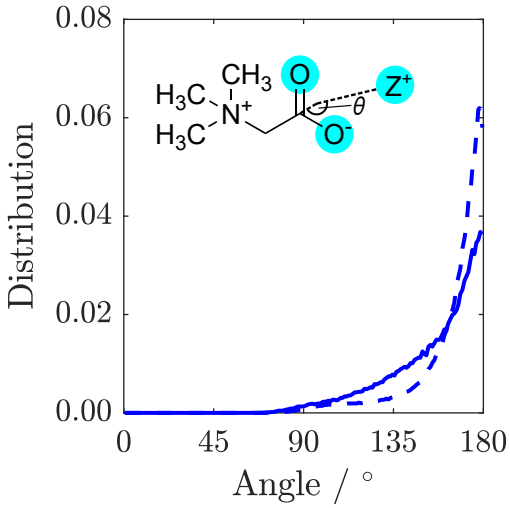

Figure 5.11: Distribution of the binding angles for potassium (solid line) or sodium (dashed line) cations coordinating to a TMG carboxylate group. This angle is defined as the angle between the vector connecting the cation and the centre of mass of the two carboxylate oxygens, and the vector connecting the same centre of mass and the carboxylate carbon atom (*i.e.* parallel to the dipole moment of the carboxylate group).

Na^+ ions are most likely to be located at binding angles of 180° (that is, equidistant to the two oxygen atoms), consistent with a bidentate binding geometry at the carboxylate group. We also note that the sodium ion distribution displays a tighter distribution about the modal angle relative to that of potassium. We interpret this to be indicative of sodium ions being bound more tightly to the carboxylate group and more often found in bidentate configurations than potassium ions, consistent with predictions from simulations,[178] while the weak shoulder around 130° that is more pronounced for potassium is representative of some monodentate coordination.

We also attribute this highly localised sodium to the differences we previously observed in the distribution of dipole angles for water molecules hydrating the TMG carboxylate group (Figure 5.7 (a)). As a reminder, the noted differences were in regard to the small peak at $\sim 140°$ present for the NaCl system, but not for KCl. The tightly-bound sodium can, in effect, fulfil the role of a pseudo-cationic group for the TMG molecule which can in turn coordinate with the water oxygen atom. It is likely that potassium fulfils a similar function, but due to being much less localised, this is not visible in the dipolar angle distribution.

5.3.5 | Ion Total Coordination Environments

For completion, it is worth considering the total coordination environments of the cations, *i.e.* from both TMG and water oxygen atoms. Running coordination numbers, *i.e.* as a function of radial distance, were calculated from the relevant pair distribution functions for various ion-oxygen interactions, and are displayed in Figure 5.12. These were calculated for the TMG oxygen-cation (O-Z) interaction and the reciprocal Z-O interaction, shown in Figures 5.12 (a) and (b), respectively. They were also calculated for the cation-water oxygen (Z-O_w) interactions (Figure 5.12 (c)) and the total cation-oxygen coordination, Z-(O+O_w) (Figure 5.12 (d)), calculated from the sum of Figures 5.12 (b) and (c). In all of the figures, vertical lines illustrate the radial cutoff distances used to determine absolute coordination numbers in the first coordination shell. These were set to $r = 3.5$ Å for Z = K, and $r = 3.2$ Å for Z = Na, the distance at the first minimum in the relevant pair distribution functions. Due to the flatness of the running CNs around the radial cutoff values, the reported CN is largely independent of whether the specific O-K or O-Na cutoff distance is used. For example, if the O-K cutoff was used for the O-Na calculation, and vice versa, the difference in the resulting O-Z CNs is small (~ 0.02).

Figure 5.12 (b) illustrates the enhanced coordination of TMG oxygens around sodium ions relative to potassium ions, along with the increased compactness of the coordination shell. The total coordination of oxygen atoms around the ions shown in Figure 5.12 (d), from both TMG and water molecules, also reflects this difference. Whilst it may be expected that potassium ions should have a larger oxygen coordination number than sodium, it has been shown that these values decrease and converge at increasing ion concentration.[171,198] Additionally, the presence of TMG further increases the similarity of these coordination numbers, as the bidentate carboxyl oxygens can sit closer together than two separate water oxygens ($\sim$ 2.1 Å compared to $\sim$ 2.8 Å), an effect more pronounced for sodium, as described previously.

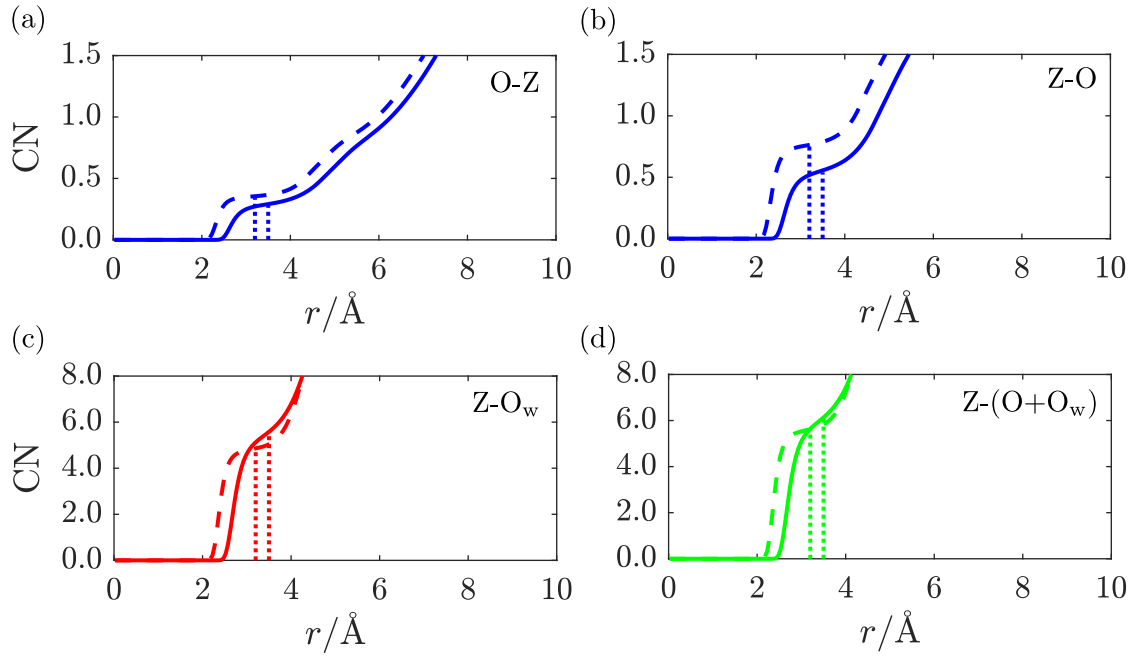

Figure 5.12: Running coordination numbers (CN) as function of radial distance r for ion-oxygen interactions, shown for potassium (solid line) and sodium (dashed line) ions. The functions are shown the following interactions: (a) O-Z, (b) Z-O, (c) Z-O_w, and (d) Z-(O+O_w). In each case, vertical dotted lines are shown at the radial cutoff values to illustrate the determined coordination number; r = 3.5 Å for Z = K, and r = 3.2 Å for Z = Na.

5.3.6 | TMG-TMG Correlations and Ion-Mediated Clusters

We next consider correlations between TMG species themselves. The calculated TMG-TMG RDFs are displayed in Figure 5.13. A comparison between the O-O RDFs in the presence of KCl and NaCl is shown in Figure 5.13 (a), and the remaining functions for a variety of correlations calculated from the two solutions are shown in Figure 5.13 (b).

The O-O RDF in the NaCl reveals two distinct peaks at distances of 3.4 Å and 4.4 Å, in contrast to the single shoulder at a distance of 4.3 Å when KCl is present. This latter case is more similar to results from a previous study by Gioacchino *et al.* determining the structure of a TMG-containing aqueous solution with no salt present.[192] In this work, a single peak at 4.1 Å was reported in the O-O RDF, attributed to water-mediated association of TMG molecules via their carboxylate groups. In the presence of NaCl, we attribute the O-O correlation peak at smaller

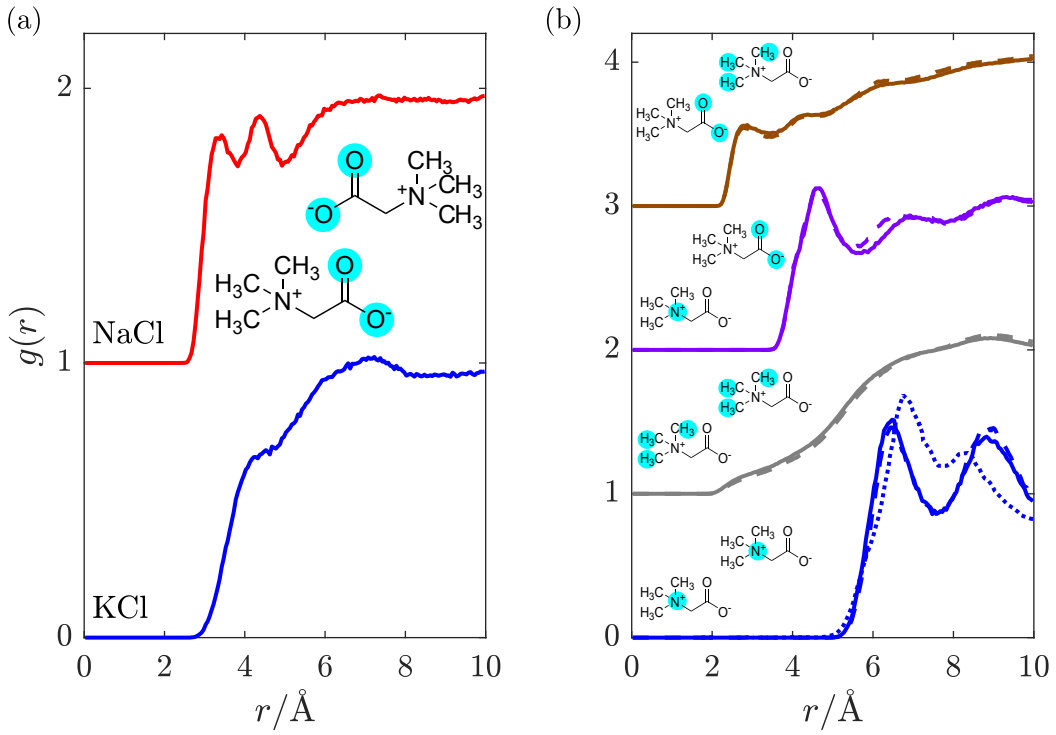

Figure 5.13: TMG-TMG RDFs calculated for a selection of intramolecular interaction sites. (a) Comparison of the O-O correlations in the presence of KCl (blue) and NaCl (red), vertically shifted for clarity. (b) N-N (blue), H-H (grey), N-O (purple) and O-H (brown) RDFs, calculated for the TMG + KCl (solid line) and TMG + NaCl (dashed line) solutions. H sites are considered on the trimethyl group only. For the N-N correlations, an additional dotted line for the case with no salt present is shown for comparison, from Gioacchino *et al.*[192]

distances to the formation of ion-mediated correlations between TMG molecules; the tight-binding between the ions and the TMG carboxylate group reduces the distance between carboxylate oxygen atoms on different molecules, relative to the case with no salt. We infer from the presence of the double peak in the presence of NaCl that the Na-mediated association of TMG is more ordered and tightly bound than the K-analogue. This is supported by Figure 5.11, the previously discussed binding angle distributions of cations coordinating to the TMG carboxylate group, which indicated similar sodium localisation.

In the context of understanding TMG-TMG associations, it is also worth considering the N-N RDF shown in Figure 5.13 (b), which displays two distinct peaks at 6.5 Å and 8.8 Å. These results are qualitatively similar to the double peak reported

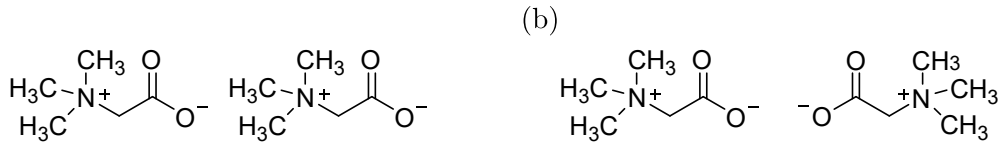

Figure 5.14: Schematic of TMG cluster geometries: (a) head-to-tail and (b) head-to-head.

for the case with no salt,[192] where the peak at a smaller distance is attributed to direct TMG-TMG chain configurations driven by electrostatic interactions due to opposite charges on the N and O sites, owing to its zwitterionic character (*i.e.* head-to-tail clustering). The peak at the larger distance was attributed to the presence of water-mediated association of TMG molecules, as we discussed previously; which, in our case, now includes ion-mediated associations (*i.e.* head-to-head clustering). Schematic geometries of these head-to-head and head-to-tail correlations are shown in Figure 5.14. It is interesting to note in the N-N RDFs that the second of these peaks is significantly smaller in height than the first with no salt present, whereas we observe a peak much more similar in height from our results in the presence of KCl or NaCl. We can obtain a measure of this by comparing the coordination number of each peak. For the case with no salt[192] the coordination number of the second peak is 2× larger than for the first, while for KCl it is 2.6× larger and for NaCl 2.9× larger (although we emphasise that in all cases similar N-N distances can be obtained through other means as well, *e.g.* from molecules located side-to-side rather than end-to-end, so are not indicative of of the absolute ratio of head-to-head versus head-to-tail correlations). From these results we infer a significantly increased likelihood of TMG-TMG association via an ion-mediated carboxylate interaction rather than a head-to-tail chain interaction driven by the TMG zwitterionic character.

Next, we further investigate these inferences via a cluster analysis, quantifying the size of TMG clusters where the TMG oxygen to oxygen distance cutoff is set at 4.9 Å, obtained from the second minimum in the O-O (NaCl) RDF in Figure 5.13 (a). Here, we employ a method used previously to study clustering and percolation in a number of experimental systems, including ionic liquids,[199] calculating

the probability $P(n)$ of finding a molecules of a specific type within a cluster of size n. In Figure 5.15 we show this cluster analysis for TMG-ion clusters in KCl- and NaCl-containing solutions, where the reported probability is scaled by the calculated percolation threshold $P^*(n) = P/P_\mathrm{p}$, in order to ensure that the identified clusters are statistically significant, and not due to random fluctuations. The threshold is given by $P_\mathrm{p} = \alpha n^{-1.2}$ where the exponent arises from the universal Fisher exponent, calculated for a three-dimensional system of non-interaction spheres and which is independent of any lattice geometry[200,201] and α is a normalisation factor.

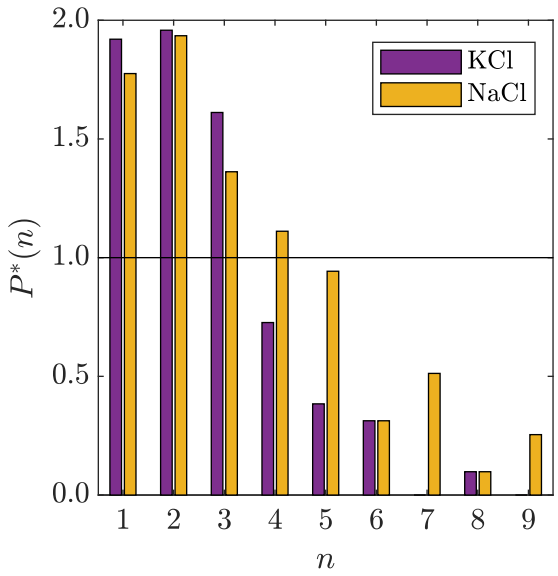

Figure 5.15: Normalised distribution function for finding clusters of TMG molecules of size n, calculated by considering O-O correlations with a radial cutoff at 4.9 Å. The reported probability $P^*(n)$ is the calculated probability of finding a cluster of size n in the box, scaled by the percolation threshold $P_\mathrm{p}(n)$.

The analysis reveals a TMG population dominated by monomers (individual TMG molecules), followed by dimers (water or ion-bridged TMG pairs, such as the example shown in Figure 5.16) and finally trimers. Unlike the differences we observe in the O-O RDFs, there is no significant difference in the extent of association across the two salt solutions. Other clusters of size $n \geq 4$ were found in both salt solutions, typically with greater frequency in NaCl, suggesting more extensive large scale structure than for KCl. However such structures were only statistically significant

for $n = 4$ - that is, larger assemblies were also detected but with probabilities lower than the percolation threshold and thus no more likely than might be expected from random fluctuations.

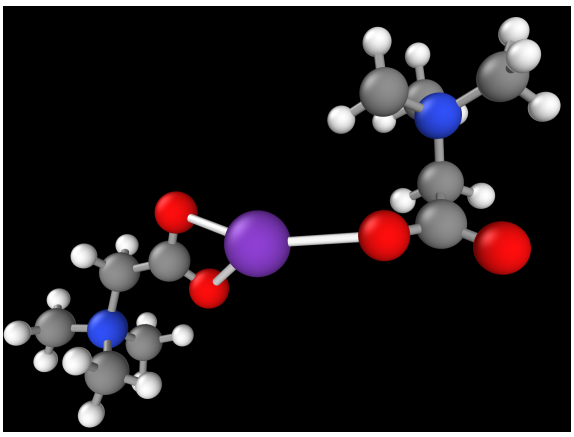

Figure 5.16: An ion-mediated TMG dimer found in the simulated structure. For emphasis, bonds are shown between the O and K atoms. Atom types: C - grey; H - white; O - red; N - blue; K - purple.

Therefore, even though the structure of such associates is seen to vary with ion identity, *i.e.* more ordered TMG-ion and TMG-TMG correlations in the presence of sodium, the size of the associates does not change dramatically. This is supported by Figure 5.13 (b), which shows similar second peak heights in the N-N RDF, indicating similar coordination numbers. However, we emphasise that neither the cluster analysis nor the RDF strictly captures the shape or stability of any aggregates. It may be that one ion species creates more long-lived, more compact or more ordered aggregates. It also does not distinguish between head-to-head configurations brought about by ion-bridging and those brought about by water-bridging, which are still likely to occur.

To establish the organisation of any TMG clusters, we instead turn to the spatial density function (SDF), which can be used to illustrate the most likely locations for finding a species of interest around a central reference site. These functions are usually displayed as surfaces where the probability of finding a surrounding species is beyond a certain threshold; other conditions can also be applied, such as specific molecular orientations.

SDFs calculated for specific TMG-TMG orientations are shown in Figure 5.17, and support the idea that the zwitterion-ion clusters are more compact in the presence of sodium than for potassium. The most likely location for a TMG molecule next to another TMG molecule is highly localised at the carboxylate group for sodium chloride, but is much less localised for potassium chloride, forming off-axis diffuse lobes either side of the carboxylate group in addition to a weaker on-axis lobe (Figures 5.17 (a) and (d)). By only considering TMG molecules oriented parallel or anti-parallel to each other, we can draw a further distinction between the two cationic species. For sodium, the SDF maxima is also the antiparallel SDF (*i.e.* head-to-head) maxima, and there is also a ring around the quaternary ammonium, suggesting side to side head-to-tail localisation (Figures 5.17 (c) and (e)). For potassium, the anti-parallel SDF is similar in character to the sodium, but the head-to-tail ring is broader (Figures 5.17 (c) and (f)). One might expect the cationic species to play no role in the head-to-tail interaction, but in fact for the potassium ion this ring is at larger distances (Figure 5.17 (c)). This could be due to presence of off-axis head-to-head TMG at the carboxylate group for potassium versus on-axis head-to-head TMG for sodium, resulting in a different overall coordination structure. On the other hand, we see little difference between the parallel SDF between the two cationic species (Figures 5.17 (b), (e) and (f)). In both cases the most likely locations are off-axis, whether at the carboxylate or quaternary ammonium group, less well defined than the anti-parallel SDFs and at very similar distances. This supports the idea that the cationic species plays little role in head-to-tail chain formation, which does not need to be propagated via an intermediate species. This analysis also emphasises the clear role of cationic species in forming head-to-head clusters: if these correlations were primarily mediated by water molecules, we would expect little difference in the SDFs between the two salt species.

Our experimental results thus confirm the presence of TMG-ion associates in solution, giving credence to the idea that TMG molecules can retain inorganic ions

in close proximity, potentially imparting protection from the salting out of proteins or biomolecules.

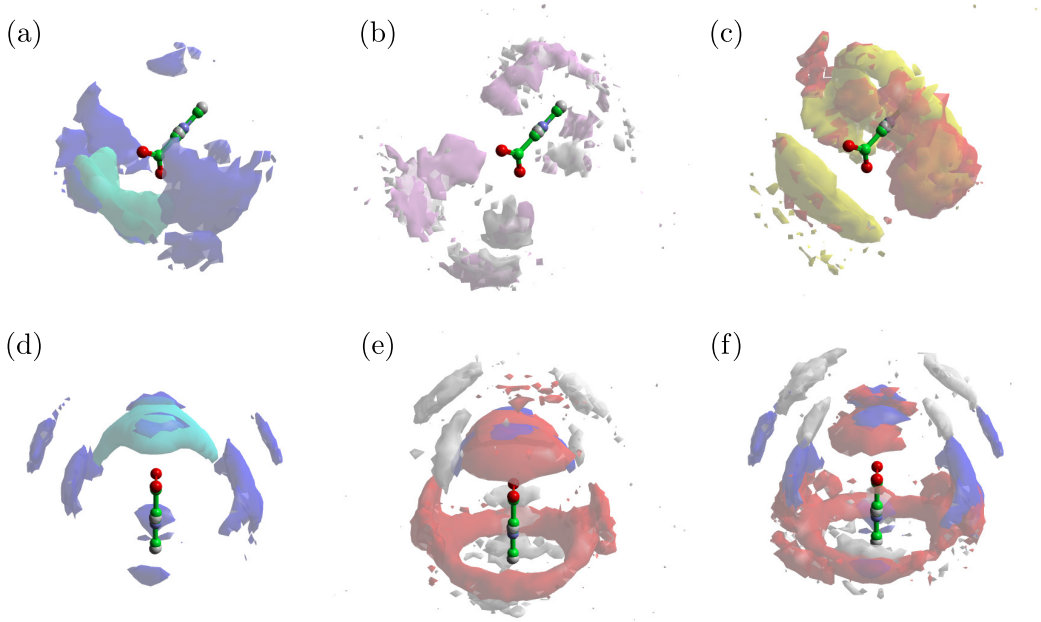

Figure 5.17: TMG carboxylate – TMG carboxylate SDFs, showing most likely locations for: (a) all orientations for both NaCl (light blue) and KCl (dark blue); (b) parallel orientation for NaCl (pink) and KCl (white); (c) antiparallel orientation for NaCl (yellow) and KCl (red); (d) same as (a) but different orientation; (e) NaCl, for all orientations (blue), antiparallel (red) and parallel (white); (f) KCl for all orientations (blue), antiparallel (red) and parallel (white). Isosurfaces are drawn of the 10% most likely configurations of carboxylate centres-of-mass.

5.4 | Summary

In this chapter, we have used a total scattering approach to determine the structure of mixed osmolyte-ion solutions, revealing molecular-level details including osmolyte-ion interactions and clustering. Specifically, we study solutions containing the common osmoprotectant, trimethylglycine (TMG), in the presence of either KCl or NaCl as a co-solute. We employ H/D isotopic substitution to generate multiple neutron scattering contrasts in addition to a further X-ray contrast, and perform structural determination with an Empirical Potential Structure Refinement (EPSR) approach using the Dissolve package.

Using the empirically refined structure, we analyse various properties concern-

ing the solution structure, including the bulk water structure, solute hydration and solute-solute interactions, for both the zwitterionic and ionic solutes. In particular, we reveal some interesting details concerning the nature of TMG-cation interactions, observing that the carboxylate group exhibits clear binding to the cations in the solution, promoting strong head-to-head TMG-TMG correlations via bridging ions. This contrasts to the case with no salt,[192] where head-to-tail dipolar chain correlations dominate, with weaker head-to-head correlations also present, mediated by hydrogen-bonded water. Sodium ions appear more highly localised than potassium ions, both in terms of distance to the carboxylate oxygen atoms and the distribution of angles with which they bind, owing to the difference in ion size and preference for bidentate coordination. This difference also enables more structurally ordered TMG-TMG associates in the presence of sodium ions, observed from the clear structuring in the TMG O-O radial distribution function, in the TMG carboxylate-water dipolar angle and most significantly in the TMG-TMG SDFs.

The observation of osmolyte-ion binding has implications for the role of TMG as an osmoprotectant in the cellular environment, providing mechanistic detail for the protection of proteins and other biomolecules from an excess of salt in the cytosolic fluid, and the bioavailability of these metabolically valuable molecules. Larger, more stable aggregates might help suppress the harmful effect of osmotic stress, at the expense of withholding them from metabolic processes. Taken together, we observe that the TMG-TMG coordination and the hydration of the TMG carboxylate group are not only influenced by the addition of salt, but show strong cation species dependence. The results from this chapter demonstrate the complex relationships that dictate self assembly and solvation structure in cytosol solutions, and highlights the role of zwitterionic osmolytes in ion-containing solutions alongside their other osmoprotective mechanisms, such as their ability to maintain water structure at high pressure, and their capacity to interact with, and modulate interactions between, biological surfaces.

6 | Interactions Across Protein Stabilising and Destabilising Osmolyte Solutions

6.1 | Background

In addition to tuning the cellular osmotic pressure, some osmolytes that are accumulated in the cytosolic fluid of certain organisms possess the advantageous ability to stabilise the folded state of biomolecules such as proteins, including proline, trimethylglycine (TMG)[202] and trimethylamine *N*-oxide (TMAO).[203] TMAO, a common protein-stabilising osmolyte whose molecular structure is displayed in Figure 6.1 (a), is considered by many to be a unique osmolyte, as unlike others, it is frequently found in nature alongside a protein destabiliser.[204] Perhaps the most notable destabilising agent is urea, a small molecule whose molecular structure is displayed in Figure 6.1 (b), which is known to play a significant role in physiological processes,[205] serving as a nitrogen source[206] and controlling osmotic pressure.[207] Hydrostatic pressure can also induce destabilisation, yet deep sea organisms have evolved to survive in such extreme environments including the Mariana Trench, where the maximum known depth is around 11 km at which hydrostatic pressures reach 1.1 kbar.[208] Much attention has been paid to the ability of TMAO to act as a 'piezolyte', *i.e.* a molecule that can resist such pressure-induced changes.[193]

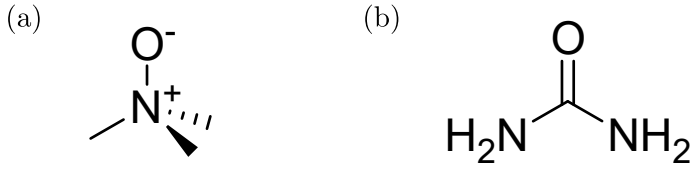

Figure 6.1: Molecular structures of (a) TMAO and (b) urea.

TMAO and urea are often found together in the cytosol of marine organisms. For example, in the tissue of southern stingrays (*Dasyatis americana*), TMAO was found at a concentration of 0.255 m and urea at a concentration of 0.604 m.[17] Across many organisms, the osmolytes urea and TMAO are often found in a molar ratio of around 2:1, but this can vary substantially depending on the organism and its surrounding environment. Most notably, in cartilaginous fish this ratio is greatly sensitive to the depth below sea level at which they live, decreasing to 0.67:1 in the deepest species found at a depth of around 2000 meters.[209]

The TMAO-urea model system has been particularly well studied in an attempt to uncover molecular mechanisms through which these osmolytes can impart protection upon, or destabilise, cellular macromolecules such as proteins. Such properties can be seen in how the protein thermal unfolding transition temperature - the temperature at which a protein thermally denatures - varies in aqueous TMAO or urea solutions of increasing concentration.[203,210] In TMAO solutions, the temperature at which a typical protein unfolds, or is thermally denatured, rises as the TMAO concentration is increased; in other words, the protein is stabilised. In contrast, increasing urea concentrations results in a lower unfolding temperature, *i.e.* the protein is destabilised. Finally, in TMAO-urea mixtures, the unfolding temperature is found to be less sensitive to osmolyte concentration than either of the individual cases. The thermal unfolding of a protein is illustrated in Figure 6.2, along with a plot showing how the unfolding transition temperature T_{m} of the enzyme ribonuclease (RNase) T1 varies as a function of osmolyte concentration in TMAO, urea and mixed TMAO-urea solutions, adapted from Lin and Timasheff.[203]

Through various structural,[174,175,196] spectroscopic[212,213] and computational[214–216] studies, a number of mechanisms have been proposed to explain these observations, invoking both enthalpic and entropic arguments.[217] These include both direct mechanisms, where osmolytes can stabilise or destabilise a protein via a direct interaction either with its backbone or side chains,[218] or indirect mechanisms where the stabilis-

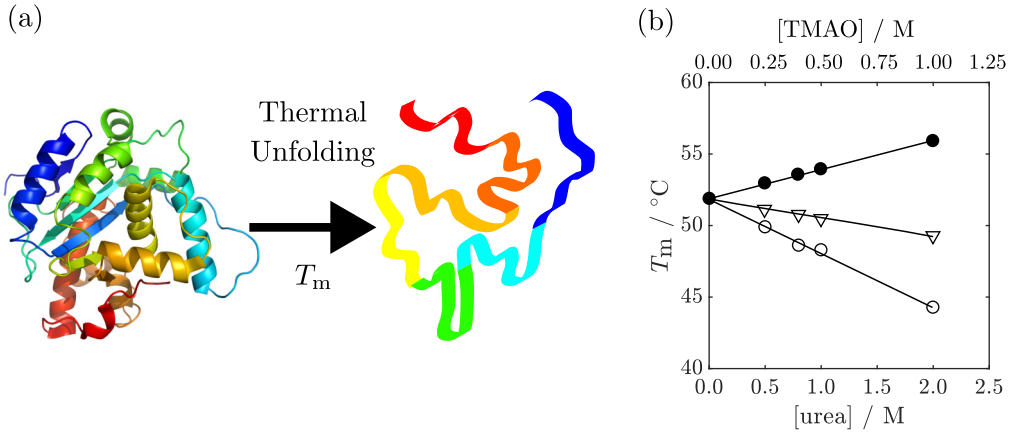

Figure 6.2: (a) Schematic of a protein thermal unfolding transition which occurs at the transition temperature T_m. The image of the protein structure is a cartoon representation of the *S. pombe* Pop2p deadenylation subunit created by Debstar and is licensed under a CC BY-SA 3.0 Licence.[211] (b) Plot showing how the thermal unfolding transition T_m of RNase T1 varies as a function of osmolyte concentration in TMAO (•), urea (○) and mixed TMAO-urea (▽) solutions. This plot is adapted with permission from Lin and Timasheff.[203] Copyright © 1994 American Chemical Society.

ing effect is instead mediated by the solvent, *i.e.* the molecular osmolytes modulate the properties of the solvent surrounding the biomolecules.[219] Despite this, a consensus remains to be reached on some of the mechanistic picture.

Some studies provide evidence supporting an independent-action model, which suggests that the opposing effects of TMAO and urea are additive, and act via independent mechanisms.[220,221] In the case of TMAO, various mechanisms of stabilising action have been suggested. A common suggestion is that TMAO can act to stabilise folded protein structures through preferential exclusion from a protein surface. Combined with its hard sphere-like properties such that two molecules do not readily overlap or associate in solution,[222] this exclusion into the surrounding solution reduces the space available to the protein. These excluded volume or crowding effects act to destabilise the unfolded state of a protein which takes up more volume relative to the more compact, folded state, therefore providing an entropic driving force for the folding of the protein.[219] Additionally, suggested enthalpic stabilising effects have included its ability to strengthen water structure which can alter the nature of the protein hydration.[193] On the other hand, urea is thought to denature via pref-

erential binding to protein backbones with little observed effect on the surrounding water structure.[175,223] Various studies challenge this independent-action model, and suggest that there is instead an interaction between TMAO and urea which could contribute to the mechanism behind TMAO counteraction of urea.[174,212,224,225] However, even where works suggest there is a measurable interaction, there is not yet an agreed picture for the nature of this TMAO-urea interaction. Some propose an interaction mediated by a hydrogen bond between the TMAO oxygen and urea hydrogen atoms,[225] whereas others suggest a hydrophobic association between the TMAO methyl groups and urea hydrogen atoms.[224]

As we have found in previous chapters, measurements using the surface force balance allow for the resolution of interactions at the molecular level between charged surfaces across aqueous solutions. Therefore, this technique has the potential to contribute new insight into the role of these two opposing osmolytes at charged surfaces, and their effect on the colloidal interactions between biomolecules in the cellular environment. The interactions between proteins in real biological environments are significantly more complex than the solely colloidal interactions that can be measured using our model system, and results from our apparatus cannot inform any specific mechanistic details surrounding osmolyte-driven protein folding, or unfolding, processes. However, the measurements performed between hydrophilic mica surfaces do have implications for understanding the surrounding electrolyte environment in which such biomolecules are found and the resulting colloidal contribution to stability or instability. These can provide an insight to the role of the osmolytes in modulating solution properties, in addition to any significant behaviour at charged surfaces. In particular, results from our model system have fundamental significance for net-negatively charged protein surfaces, with exposed hydrophilic residues.[162]

In this chapter, we present direct measurements of the interaction energy between charged mica surfaces across solutions containing TMAO and urea in dilute, aqueous KCl electrolytes. We begin by considering solutions containing TMAO and urea

individually, followed by an investigation of a mixture containing both osmolytes.

6.2 | Experimental Details

6.2.1 | Materials and Solution Preparation

Trimethylamine *N*-oxide dihydrate (TMAO, Sigma-Aldrich®, > 99.0%), urea (Thermo Scientific, > 99.3%) and potassium chloride (KCl, Thermo Scientific, > 99.995%) were used as received. Surface forces measurements were performed across solutions containing: 0.6 m TMAO, 0.6 m urea, and one containing both 0.6 m TMAO and 0.6 m urea, all with a background KCl concentration of 0.003 m KCl. An additional measurement was also performed across a higher concentration urea solution (0.9 m).

6.2.2 | Refractive Indices and Hamaker Constants

The refractive indices for the electrolytes were measured using the method outlined in Chapter 2. The Hamaker constants for all electrolytes reported in this chapter are shown in Table 6.1, and the displayed relative permittivity of the electrolytes were estimated using Equation 6.1:

$$\epsilon_{\mathrm{e}} = \epsilon_{\mathrm{r}}^{0} + \delta_{\mathrm{TMAO}} c_{\mathrm{TMAO}} + \delta_{\mathrm{urea}} c_{\mathrm{urea}} + \delta_{\mathrm{KCl}} c_{\mathrm{KCl}} \tag{6.1}$$

where $\epsilon_{\mathrm{r}}^{0}$ is the relative permittivity of water (78.4), δ_i is the dielectric increment of solute i and c_i is the solute concentration. The dielectric increments were obtained from literature, and we have taken δ_{TMAO} to be 2.16 / m,[226] δ_{urea} to be 2.7 / m,[227] and δ_{KCl} to be -8.85 / m.[159]

6.3 | Surface Forces Measurements Across TMAO or Urea Solutions

In the following section, we will present various results from surface forces measurements across TMAO-urea solutions, firstly considering solutions containing TMAO

Table 6.1: Parameters used for Hamaker constant calculations. Concentrations of TMAO c_{TMAO}, urea c_{urea}, KCl c_{KCl}, refractive index n_{e}, relative permittivity ϵ_{e} and Hamaker constant A are shown.

c_{TMAO} / m	c_{urea} / m	c_{KCl} / m	n_{e}	ϵ_{e}	A / 10^{-20} J
-	-	0.003	1.3323	78.4	2.08
0.6	-	0.003	1.3381	79.7	2.00
-	0.6	0.003	1.3374	80.0	2.01
-	0.9	0.003	1.3398	80.9	1.97
0.6	0.6	0.003	1.3429	81.2	1.93

and urea individually. This allows for the interrogation of the influence of each on the measured interactions, necessary to form a benchmark to which to compare a mixture of both osmolytes in a future section.

6.3.1 | TMAO Solutions

The measured interaction potential across an electrolyte containing TMAO (0.6 m) in a background KCl (0.003 m) electrolyte is shown in Figure 6.3. A repulsion is observed between the surfaces upon approach from large separations. This repulsion increases in magnitude down to distances as close as $\sim$ 3 nm, at which point attractive forces dominate, causing a spring instability and resulting in the surfaces jumping together. A deep adhesive minimum is revealed upon retraction of the surfaces, where a large force is required for the surface separation, at which point they jump to large separations. The parameters for the DLVO fit to this measurement are displayed in Table 6.2. Also displayed for comparison in Figure 6.3 is a measurement across the osmolyte-free, background KCl electrolyte (0.003 m). In a similar manner to the dilute KCl electrolyte discussed in Chapter 3, data from approach of the surfaces reveal an electric double layer repulsion at larger surface separations and a contribution from hydration forces at smaller separations. This measurement is shown in full, *i.e.* with data obtained from retraction of the surfaces, in Appendix C (Figure C.1).

For multiple measurements across the TMAO solution, there are significant fluc-

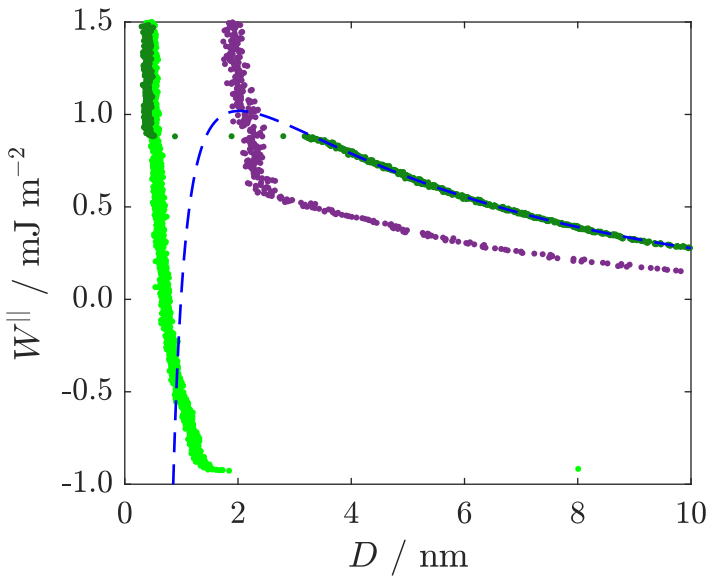

Figure 6.3: Measured interaction free energy as a function of surface separation across a solution containing 0.6 m TMAO in a 0.003 m KCl background electrolyte. The measurement upon approach of the surfaces is shown in dark green and that upon retraction is shown in light green. The DLVO fit for this measurement is shown by the blue dashed curve, parameters for which are displayed in Table 6.2. Also displayed for comparison in purple is the measured interaction across the osmolyte-free background KCl electrolyte (0.003 m).

Table 6.2: Parameters used for DLVO fits to the measured interaction free energy across the TMAO solution shown in Figure 6.3. The fitted effective surface potential ψ_{eff}, Debye screening length κ_{D}^{-1}, charge regulation parameter p, and offset to the zero surface separation D_0 are shown.

c_{TMAO}/ m	c_{urea}/ m	c_{KCl}/ m	ψ_{eff} / mV	κ_{D}^{-1} / nm	p	D_0 / nm
0.6	-	0.003	80 ± 44	6.9 ± 1.8	0.63 ± 0.18	0.0 ± 0.0

tuations in both the magnitude of the repulsive barrier and the depth of the primary minimum, indicated by the large error in ψ_{eff}. A series of runs illustrating these observations are shown in Appendix C (Figure C.2). As a result the magnitude of the electric double layer repulsion between the two interactions shown in Figure 6.3 should not be directly compared. These complex variations over a series of runs are indicative of fluctuations in surface properties that cannot be easily understood. In contrast, the change in surface separation upon the jump to small separations is highly consistent between runs ($\sim$ 3 nm).

6.3.2 | Urea Solutions

Next, we present the analogous measurement containing urea, shown in Figure 6.4, and the parameters for the DLVO fit are displayed in Table 6.3.

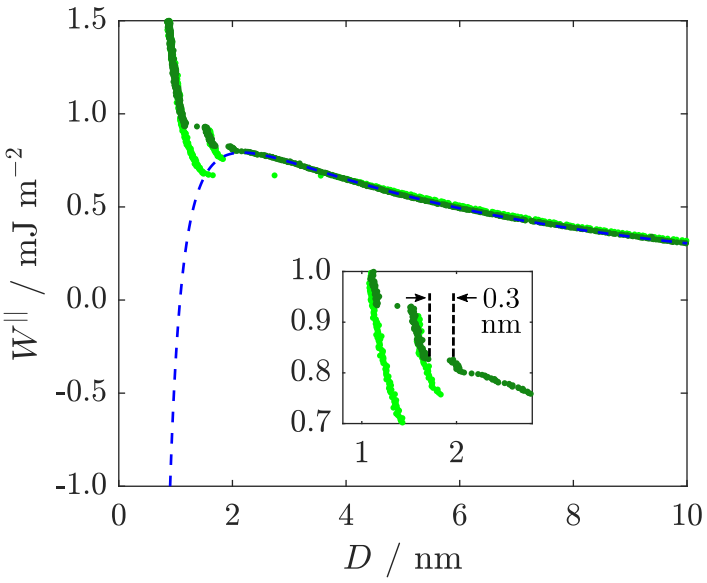

Figure 6.4: Measured interaction free energy as a function of surface separation across a solution containing 0.6 m urea in a 0.003 m KCl background electrolyte. The measurement upon approach of the surfaces is shown in dark green and that upon retraction is shown in light green. The DLVO fit is shown by the blue dashed curve, parameters for which are displayed in Table 6.3. The retraction at larger surface separations was recorded on a different run to the rest of the displayed measurement; due to small differences in the magnitude of the interaction between runs, the data points for this retraction have been shifted vertically by -0.16 mJ m^{-2} to ensure alignment in this feature.

Table 6.3: Parameters obtained from the DLVO fit to the measured interaction free energy across the 0.6 m urea solution shown in Figure 6.4. The fitted effective surface potential ψ_{eff}, Debye screening length κ_{D}^{-1}, charge regulation parameter p and offset to the zero surface separation D_0 are shown.

c_{TMAO}/ m	c_{urea}/ m	c_{KCl}/ m	ψ_{eff} / mV	κ_{D}^{-1} / nm	p	D_0 / nm
-	0.6	0.003	60 ± 8	13.5 ± 2.1	0.86 ± 0.03	0.2 ± 0.1

This measurement shows a monotonic repulsion upon approach down to surface separations of around 2 nm. However, in contrast to the single jump of distance of several nanometres observed for the TMAO measurement, we observe a series of three repulsive walls separated by jumps of $\sim$ 0.3 nm. These features are characteristic of a structural, non-DLVO contribution to the overall measured potential.

Repulsive minima (*i.e.* when $W^{||}$ is positive) were revealed upon retraction from the two hard walls at smallest surface separations, with subsequent jumps to larger separations into the monotonic, repulsive regime. Consistent with these repulsive minima is the fact that the close surface separations are not reached during this measurement, contrasting with the previous TMAO solution. Implicit with this is the presence of a strongly adhered film between the two surfaces which cannot be expelled across the range of $W^{||}$ measurable in this experiment.

An analogous measurement obtained for a higher concentration of urea (0.9 m) is shown in Figure 6.5, and the parameters associated with the DLVO fit for this measurement are displayed in Table 6.4.

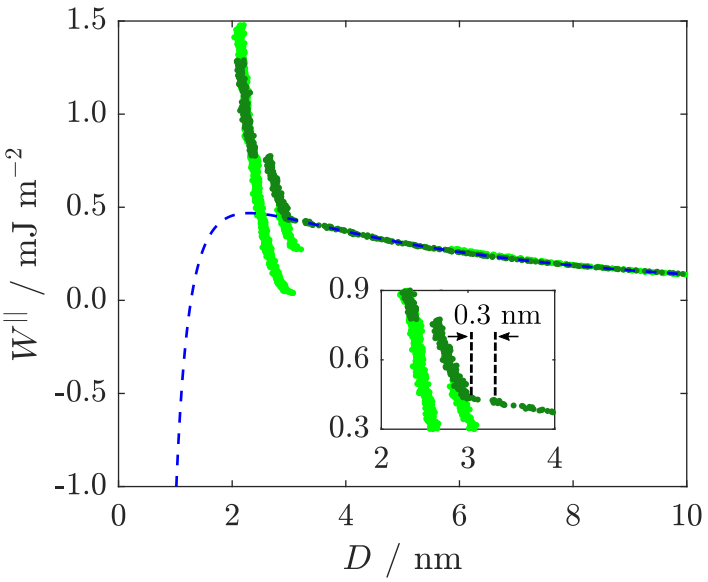

Figure 6.5: Measured interaction free energy as a function of surface separation across a solution containing 0.9 m urea in a 0.003 m KCl background electrolyte. The measurement upon approach of the surfaces is shown in dark green and that upon retraction is shown in light green. The DLVO fit is shown by the blue dashed curve, parameters for which are displayed in Table 6.4.

Table 6.4: Parameters obtained from the DLVO fit to the measured interaction free energy across the 0.9 m urea solution shown in Figure 6.5. The fitted effective surface potential ψ_{eff}, Debye screening length κ_{D}^{-1}, charge regulation parameter p and offset to the zero surface separation D_0 are shown.

c_{TMAO}/ m	c_{urea}/ m	c_{KCl}/ m	ψ_{eff} / mV	κ_{D}^{-1} / nm	p	D_0 / nm
-	0.9	0.003	51 ± 7	8.8 ± 0.9	0.83 ± 0.03	0.7 ± 0.4

The measurement across this elevated concentration is qualitatively similar to that obtained for across the lower concentration. This is most notable for the non-DLVO, structural contribution, where a similar series of jumps of width ~ 0.3 nm can again be seen. Slight differences are also observable between the two measurements including the smallest surface separation which can be reached during a measurement: ~ 1 nm for the 0.6 m urea solution and ~ 2 nm for the 0.6 m solution. This observation suggests that there is a thicker film that is not expelled from between the surfaces in the case of the higher concentration solution.

6.3.3 | Discussion

Turning initially to the TMAO solution, significant differences can be seen between the osmolyte-containing and osmolyte-free measurements both displayed in Figures 6.3. In the TMAO-containing solution, we observe a long-range electrostatic repulsion followed by a jump over several nanometres. This is in stark contrast to the measurement across the osmolyte-free, background KCl electrolyte which displays structural, hydration forces rather than the jump to small separations. The absence of these structural contributions in the TMAO-containing solution must arise from TMAO-induced perturbations to the hydration layers that are otherwise observed. It is also interesting to note that a similar disruption of the hydration structure was observed in Chapter 4 for TMG in a dilute KCl electrolyte (Figure 4.9 (a)).

Like other prominent protein-stabilising osmolytes, TMAO has a molecular structure which combines a large dipole moment and a hydrophobic group surrounding the positive end of the zwitterionic molecule, and as discussed previously these antagonistic properties provide a mechanism for their stabilising effects.[28] The dipoles allow the molecules to interact strongly with the surrounding water and are significantly hydrated, with TMAO existing effectively as a di- or trihydrate in solution.[174,193,213,228] The hydrophobic groups, on the other hand, prevent significant interaction between dipoles, and no hydrophobic association is observed between

TMAO molecules due to the like-charge repulsion. This frustration between the strongly hydrated dipole and the bulky hydrophobic group potentially and resulting distortion of the water network potentially lies behind the absence of structural features in this measurement, disrupting the near-surface water ordering that would be observed in the absence of the osmolyte. The absence of any structural features at small separations also suggests that there is no significant accumulation of TMAO at the interface.

It is also interesting to note that the DLVO fit to the interaction across the TMAO solution displayed in Figure 6.3 does not accurately capture the jump to small surface separations, particularly when compared to similar Type I DLVO-like measurements discussed in previous chapters. The maximum of the DVLO fit occurs at smaller distances than the separation at which the jump commences upon approach: such discrepancy implies the presence of an additional attractive contribution to the overall interaction that is not captured by the DLVO model. Since it is not possible to determine the exact form of the attractive interaction using this technique, we are limited to hypothesising potential sources of attraction. For instance, if TMAO is indeed expelled from the surface, one source of attractive may arise from a depletion-like interaction particularly if, as we have previously suggested, the TMAO strongly coordinates several water molecules at its oxygen atom, effectively enhancing the size of the TMAO molecule.

The urea solution is more qualitatively similar to that obtained across the background KCl electrolyte, with measurable hydration forces at small surface separations as we previously discussed. The presence of urea must therefore be compatible with the water network for which hydration forces are measurable in the SFB, contrary to the frustrating effects of a TMAO molecule. It appears that these observations are consistent with previously determined influence of urea on the structure of aqueous solutions, as determined by a variety of methods. For example, Soper *et al.* investigated the structure of urea-water solutions using neutron diffraction,

where it was found that urea molecules were able to readily substitute themselves into the hydrogen bonding network of water without a significant impact on the nature of the bulk water structure.[175] This is also consistent with the conclusions of an NMR spectroscopy study used to determine the dynamics of water molecules and thus the role of urea and TMAO solutes in modulating the strength of the water hydrogen bonding network. This study found that the water diffusion coefficient was much less sensitive to the addition of urea than for TMAO, which decreases more substantially upon addition. This was taken to suggest that urea plays little role in altering the strength of the hydrogen bond network, in contrast to TMAO which results in significant strengthening.[225]

Whilst it is possible to draw a similarity between the measurements across the urea solution and the background electrolyte in terms of the presence of hydration forces, it is difficult to discern any significant information concerning the arrangement of urea molecules at the interface. It is possible that urea forms part of the film of fluid that cannot be expelled from between the surfaces across the range of accessible forces, implying a propensity of urea to the charged interface. Studies have suggested that urea can orient itself with its dipole moment perpendicular to a charged surface, with the specific orientation dependent on the charge of the surface.[229] Therefore, it is feasible that urea could be adsorbed at the negatively charged mica surface, most likely with the carbonyl oxygen pointing away from the surface, *i.e.* with its dipole moment aligning with the electric field generated by the interface. Adsorption of urea at the interface may also be consistent with the difference in the thickness of the film that cannot be expelled from between the surfaces at the different urea concentrations. The thicker film in the case of the more concentrated solution could be due to a more rigidly defined layer of urea molecules, or even multilayers, at the interfaces. However, no direct evidence can be seen for the adsorption or orientation of urea from these measurements, and it would be interesting to elucidate the nature of the surface structure in future investigations,

such as molecular simulations.

It is also worth briefly returning to the measured ~ 0.3 nm structural features observed in the urea measurements which, up until now, we have attributed to water layering. Another possibility arises from a consideration of the molecular dimensions of urea, known to be approximately 0.5 nm across its two long axes and 0.3 nm perpendicular to the plane of the molecule, as shown in Figure 6.6.[230] Therefore, it is possible that these features could arise from urea molecules aligning with their plane parallel to the interface, as this would be compatible with the size of the observed features, though again no direct evidence can be seen for this.

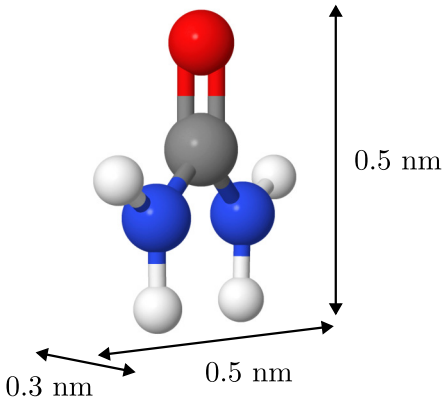

Figure 6.6: The molecular dimensions of urea, which are ~ 0.5 nm along its two long axes in the plane of the molecule, and a short axis of size ~ 0.3 nm perpendicular to the plane.[231]

Overall, it is likely that our observations for the presence of hydration forces in urea solutions and absence in TMAO solutions are best interpreted through the lens of previous findings pertaining to the effects of these osmolytes on the structure of water. The absence of the ~ 0.3 nm structural features at small surfaces separations in the presence of TMAO can be attributed to its antagonistic dipolar/hydrophobic properties, which results in the frustration of the hydrogen bonding network and the disruption of the near-surface hydration structure that is observed in the background electrolyte without any TMAO. The presence of the structural features dominated by water layering in the urea solution is indicative of the ability for urea to substitute itself readily into water's hydrogen bonding network, thus allowing for a

water-urea mixture to solvate the mica surface in a similar fashion to an aqueous KCl solution resulting in a qualitatively similar structural features at small separations. Schematic cartoons for the surface molecular arrangement and structural lengthscales observed in the surface forces measurements are displayed in Figure 6.7.

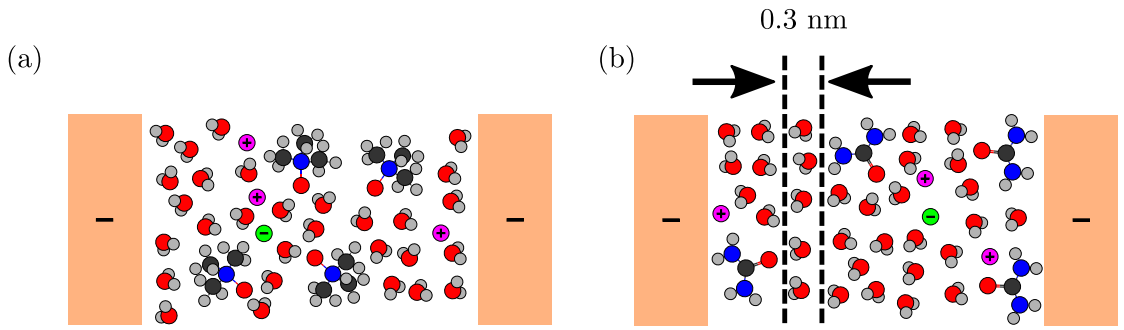

Figure 6.7: Cartoons illustrating the interfacial structures inferred from the surface forces measurements across (a) TMAO and (b) urea electrolyte solutions.

6.4 | Surface Forces Measurements Across TMAO-Urea Mixtures

In this next section, we present a measurement across a mixture containing equimolal amounts of both TMAO and urea (0.6 m) in a dilute KCl electrolyte (0.003 m); the measured interaction potential is shown in Figure 6.8. In a similar manner to those across the individual TMAO and urea electrolytes, the measured interaction potential displays a monotonic repulsion down to around 1 nm. At this point a jump of size $\sim$ 0.3 nm to a repulsive wall is observed, followed by a second jump of size $\sim$ 0.6 nm to a repulsive wall, the closest point of surface approach. The initial, smaller jump is of similar size to those seen for the urea system (Figure 6.4); however, the second, larger jump was not previously seen. Retraction of the surfaces reveals a slightly adhesive minimum, consistent with close surface contact, but not as deep as the minimum measured for the TMAO case.

The measurement across the TMAO-urea mixture (Figure 6.8) clearly displays a compromise between the two single osmolyte scenarios. Upon approach of the surfaces, the initial measured step of size $\sim$ 0.3 nm is consistent with hydration layers measured in the urea (Figure 6.4) and KCl-only (Figure 6.3) scenarios. The

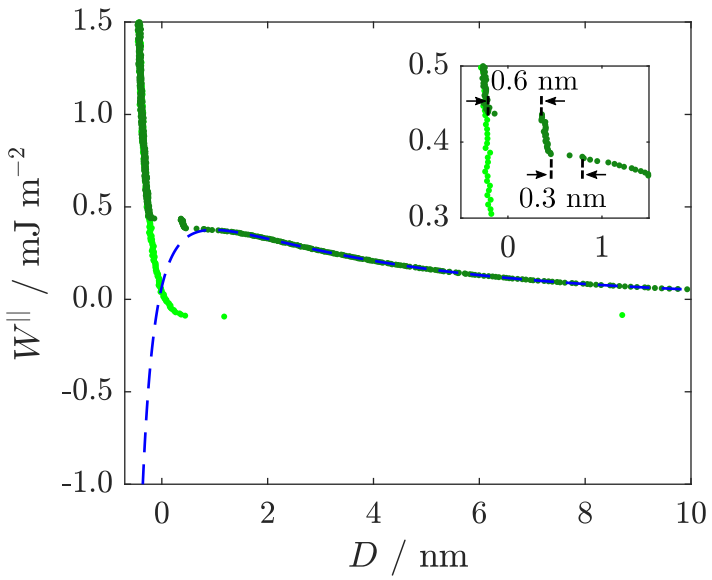

Figure 6.8: Measured interaction free energy as a function of surface separation across a solution containing equimolal 0.6 m TMAO and urea in a 0.003 m KCl background electrolyte. The measurement upon approach of the surfaces is shown in dark green and that upon retraction is shown in light green. The DLVO fit is shown by the blue dashed curve, parameters for which are displayed in Table 6.5. The displayed surface separations less than zero are due to errors introduced in small alterations to the setup between the calibration and measurements, such as to the optical path.

Table 6.5: Parameters obtained from the DLVO fit to the measured interaction free energy across the TMAO-urea mixture shown in Figure 6.8. The fitted effective surface potential ψ_{eff}, Debye screening length κ_{D}^{-1}, charge regulation parameter p and offset to the zero surface separation D_0 are shown.

c_{TMAO}/ m	c_{Urea}/ m	c_{KCl}/ m	ψ_{eff} / mV	κ_{D}^{-1} / nm	p	D_0 / nm
0.6	0.6	0.003	41 ± 1	4.9 ± 0.2	0.75 ± 0.03	-0.7 ± 0.2

subsequent step of ∼ 0.6 nm, rather than further steps of size ∼ 0.3 nm, is unique to this mixture. A potential origin of this structural feature can be found by considering that this distance loosely corresponds with the size of a urea molecule along the direction parallel to its dipole moment (one of the long axes in Figure 6.6).[210] This structural feature may therefore arise due to an adsorbed layer of urea molecules, with their dipole moments aligned perpendicular to the interface as we previously hypothesised in relation to measurements across the urea solutions. A schematic cartoon for the surface molecular arrangement with the relevant structural lengthscales observed in the surface forces measurements is displayed in Figure 6.9.

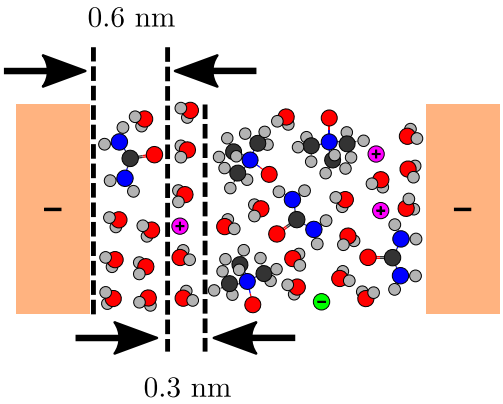

Figure 6.9: Cartoon illustrating the interfacial structure inferred from the surface forces measurements across a mixed TMAO-urea electrolyte solutions.

In addition to our previous suggestion that TMAO can frustrate the near-surface hydration structure, which may also account for some of the observable differences between the urea solution (Figure 6.4) and the TMAO-urea mixture (Figure 6.8), it is also worth considering the potential role of interactions or synergies between the two osmolytes. As described previously, there is an increasing body of evidence suggesting that there is indeed a non-negligible, favourable interaction between TMAO and urea, though as discussed, there is little consensus on the strength and nature of such an interaction. There is also some evidence to suggest that, due to this preferential interaction, TMAO can deplete urea from the surface of a protein, potentially providing mechanistic rationale for the protein-stabilising ability of TMAO.[214,232] This preferential interaction between the two osmolytes, and resulting depletion of urea from a hydrophilic biomolecule surface in the presence of TMAO, could be used to explain some of the described observations from our measurements. If TMAO can act to deplete the urea present in the hydration layer, the near-surface layer may be disrupted relative to the urea case, thus reducing the magnitude of $W^{||}$ required to completely squeeze out such layers and access small surface separations. As suggested in the previous section, it would be of interest to use complimentary techniques such as simulations to further elucidate molecular arrangements in these surface structures.

In the context of two proteins or other biomolecules interacting, the interaction

landscape observed across this mixture situation may actually be more beneficial than those previously described for the individual osmolytes. Where a protein is interacting with another, nearby protein, it must be able to reach a small enough separation in order to interact through short-range, protein-specific interactions. Moreover, it is beneficial not to be trapped in a deep energy minimum such that the two biomolecules are not irreversibly bound and can detach under reasonable timescales.[162] The energy profile that is most conducive to such an interaction is that of the osmolyte mixture discussed in this section, where there is only a small energy barrier to close contact, without a deep minimum inhibiting particle separation. Such a conclusion is reminiscent of the counteracting-osmolyte hypothesis introduced by Yancey *et al.*, which suggests that utilising a mixture of stabilising and destabilising osmolytes in the cytosolic fluid can indeed be more beneficial to organism growth than the sole accumulation of stabilising osmolytes. This is since, on their own without any perturbant present, they can over-stabilise biomolecules by reducing protein flexibility and favouring non-functional aggregates.[204,233,234] Such damaging effects observed due to the accumulation of TMAO include amyloid formation, linked to the onset of various diseases such as Alzheimer's,[235] and more recently, the aggregation of the intrinsically disordered α-casein protein.[236,237]

6.5 | Summary

In this chapter, we have presented direct surface force measurements across electrolytes containing the stabilising and destabilising osmolytes, TMAO and urea. This model cytosol fluid confined between negatively charged, mica surfaces provides an opportunity to investigate how these osmolytes, both individually and in synergy, modulate the interactions between hydrophilic surfaces, reminiscent of the exposed surface of biomolecules in solution. These results contribute to understanding the colloidal contribution to stability, or instability, of charged biomolecules in the cellular environment.

We observe that at comparable concentrations, TMAO, unlike urea, disrupts the hydration forces that are otherwise measured in the osmolyte-free background electrolyte, linking these observations to the differing molecular properties of the two osmolytes. Subsequently, we show measurements across a mixture of both osmolytes and observe a compromise between the two individual cases with the partial disruption of the near-surface structure, reducing the energy barrier for close-surface contact relative to the urea case. However, the close contact is reached without the large jump together of the surfaces during approach and deep energy minimum observed upon retraction in the TMAO case, and we form an analogy between these observations and the counteracting-osmolyte hypothesis of Yancey *et al.* which suggests that a mixture of stabilising and destabilising osmolytes can be beneficial for biological function, potentially revealing molecular, mechanistic detail for such a hypothesis.

7 | Glycine Oligopeptides at Charged Surfaces

7.1 | Background

So far we have considered the role of small molecules on the properties of cytosol solutions and the implications of these results for biochemical processes. However, as we discussed in Chapter 1, the makeup of the cellular environment is much more complex than just small molecules and ions, and contains chemical and biochemical species ranging widely in size. In this chapter, we will consider the role of some oligopeptides, short-chain polymers comprising amino acid repeat units.

Oligopeptides can arise in a wide range of biochemical contexts. Proteolysis, for example, is a process that involves the breakdown of proteins, resulting in the generation of short chain oligopeptides.[238] This process is essential for regulating physiological processes such as preventing the accumulation of unwanted or misfolded proteins, or digesting protein absorbed from food intake into amino acids to use as biochemical building blocks. Without a catalyst, proteolysis occurs with a half-life of hundreds of years due to the durability of the peptide bond, but this process can be sped up rapidly by enzymes called proteases.[239] These are complexes which break down proteins tagged with ubiquitin, a molecule which is used by biochemical regulatory processes to signal proteins that are to be degraded. This ubiquitin-protease system (UPS) is well studied and a vital part of the biochemical machinery used to regulate the cytosolic composition, and can break down proteins into short peptides, from around 3 to 25 amino acids in length.[240] These small oligopeptides can be broken down further by cytosolic peptidases, while others remain to serve regulatory or signalling functions.[241]

Short peptides can also accumulate due to ribosomal stalling, which can oc-

cur during protein synthesis where errors or premature termination of the protein synthesis process occur. This can result in the release of short peptides or longer, truncated proteins into the cytoplasm.[242] Alternatively, some oligopeptides are actively transported into the cell or organelle membranes; for example, mitochondrial peptides involved in stress response.[243]

In this chapter, we will be specifically be considering the role of short, oligoglycine units; peptides comprised of repeat glycine units. On their own, oligoglycine molecules are not likely to be accumulated to significant concentrations in the cytosol, as they do not serve any widespread biological function. As such, if present in a biochemical environment, any oligoglycine strands will likely be short lived and rapidly degraded by the peptidases. Nevertheless, the study of glycine peptides remains of wider interest since these short units can serve a purpose as constituent sequences of certain larger peptides. In particular, glycine-rich regions can be employed in protein sequences to gain certain functional benefit, most notably the flexibility imparted due to the small size of glycine and its lack of steric hindrance. As such, glycine-rich regions can be useful in parts of the protein peptide backbone that require ease of conformational change or structural adaptability, such as hinges or loops, facilitating interactions with other molecules, and these small peptide units are a good model for investigating the role of these units present in larger structures.

Glycine-rich sequences can also be found in intrinsically disordered proteins (IDPs) or regions of proteins (IDRs).[242] These proteins or protein regions are ubiquitous across the biosphere, making up an estimated 30% of the eukaryotic proteome, and have been found to be employed in various, dynamic biochemical processes, including regulation of signalling.[244] The peptide backbone of the glycine-rich regions have been hypothesised to be useful as a free energy reservoir in which energy may be stored as conformation entropy through structural transitions.[245,246] Additionally, many proteins utilise a combination of ordered and disordered regions to fine tune the binding affinity to certain targets. The discovery of this class of protein chal-

lenged the sequence-structure-function paradigm of molecular biology, where a fixed three-dimensional structure was deemed necessary for a protein to achieve biological function.[247] An alternative framework - the protein trinity hypothesis - has since been proposed, which suggests that proteins can exist in a dynamic equilibrium between three states: solid-like ordered; liquid-like collapsed-disordered; and gas-like extended-disordered.[248] The hypothesis suggests that proteins can exist functionally in any of these three states, and that function can even arise from transitions between the different states.

As we have alluded to, disordered protein structures arising from high glycine content can be functional; for example, in amyloid fibres such as the Curli protein which are produced by certain strains of bacteria. These proteins can help the organisms form biofilms, providing a protective barrier for the organism against harsh environments. However, protein aggregates can also be pathological; the presence of certain amyloid fibres is linked to the onset of various human diseases, including Alzheimer's and Parkinson's.[249]

Oligoglycines have also found interest in nanotechnology applications, including molecular electronics and biomimetic materials.[250,251] This class of peptides have been shown to form nanotubes and self-assembled nanostructures at surfaces, including mica.[252–254]

Fundamental to all of these applications, both natural and technological, are the underlying interactions between the various constituent units which govern the structure and function. Studying these interactions is necessary to better understand, at the molecular level, the processes that govern the structure and function of these biochemical constituents, and such knowledge can inform the development of novel nanotechnologies.

7.1.1 | Interactions Between Glycine Oligomers

Various physical properties of oligoglycine peptides have been previously investigated, owing to their use as a protein backbone model, and relevance in understanding the structure and function of glycine-rich, intrinsically disordered proteins, as we have outlined. Experimentally, these glycine units become increasingly difficult to study at longer chain lengths owing to their rapidly diminishing solubility: triglycine is only soluble to concentrations of several hundred millimolar;[255] and pentaglycine has a solubility limit as low as 1 mM.[256] Solubility is an interesting viewpoint through which to begin our discussion of the solution thermodynamics, as it is intrinsically related to the balance between solute-solute, solute-solvent and solvent-solvent interactions and their associated free energies.[257] A brief overview of previous findings relating to the solution thermodynamics will be discussed in the following sections, which will underpin our study of oligoglycine-containing aqueous solutions throughout this chapter.

Despite what the solubility trend might suggest, simulations of oligoglycines Gly_n at infinite dilution - or, in other words, individual molecules - have found that the solvation free energy ΔG_{sol} becomes increasingly negative as a function of n, driven by favourable enthalpic interactions between water molecules and the peptide backbone.[258] Since the solvation of an oligoglycine becomes more favourable with the lengthening of the peptide, the solubility trend must instead be accounted for by an even more substantial increase in the strength of attractive interactions between peptides - either intermolecular interactions in the case of short oligomers, or additional intramolecular interactions in the case of longer ones[259] - which outcompete the enhanced solvation interactions. In other words, the dissolved state of the oligoglycine does not possess the minimum Gibbs free energy at that concentration. This conclusion is perhaps contrary to what may be assumed by invoking more general ideas from protein folding, that it is the hydrophobic interaction that drives folding and aggregation processes.[260]

The next question, therefore, is to determine which specific interactions contribute most strongly to the enhanced, overall interaction between the backbones. Hydrogen-bonding interactions clearly play an important role in the wider context of protein physics; however, it is an additional peptide-peptide interaction that has been found to play an even more significant role in contributing to these backbone interactions. Dipolar interactions between carbonyl motifs on amide functional groups present in the peptide backbone have been shown to significantly contribute to the stabilisation of structures.[261,262] Such stabilisation arises from $n \rightarrow \pi^*$ interactions: the delocalisation of a lone pair of electrons from the oxygen atom of one carbonyl (n) to the antibonding orbital of the adjacent carbonyl group (π^*).[263] Whilst the CO dipolar interactions have been shown to be similar in energy to hydrogen bonds, they are found in more appreciable quantities of short glycine peptides into clusters of short glycine peptides, or the collapse of longer oligomers. The two types of interactions that can act between oligoglycine strands - hydrogen bonding and carbonyl dipolar interactions - are illustrated in Figure 7.1.

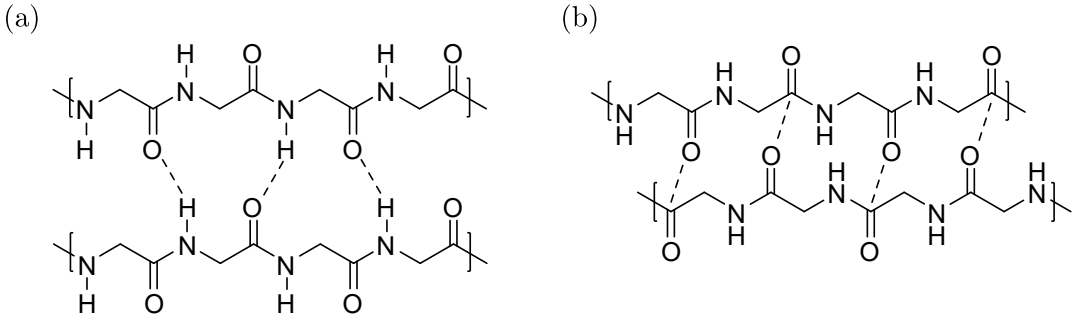

Figure 7.1: Schematic illustrating the two possible types of interactions between oligoglycine strands: (a) hydrogen bonds and (b) carbonyl dipole-dipole interactions. In each case, the interaction is shown by a dashed line.

7.1.2 | Surface Interactions Across Glycine Oligopeptide Solutions

These molecules were of interest in the context of this work in their use as a model peptide. These peptides are zwitterionic at ambient pH and of tunable length, with no side groups to impart additional complexity in intermolecular, and surface, interactions. As we have shown in this thesis so far, surface forces measurements

allow for the interrogation of interactions between surfaces and molecules with sub-nanometre precision.

In this chapter, we present surface forces measurements across aqueous solutions containing oligoglycine strands, between one and three units, at varying concentrations. Through the lens of these measurements, we are able to interrogate the influence of these molecules on interactions between charged surfaces. This, in turn, will yield valuable information about the behaviour of these molecules at such interfaces, and in particular, the balance between solute-solute and solute-surface interactions. IDPs and IDRs have been shown to exhibit binding with other proteins, nucleic acids and lipid membranes, and such interactions are vital for various aspects of their biochemical function.[264] The model experiments presented in this chapter will aim to shed light on the underlying interactions that govern such processes.

7.2 | Experimental Details

7.2.1 | Materials and Solution Preparation

Surface forces measurements were performed on aqueous solutions of oligoglycines Gly_n, where the peptide length n was varied between 1 and 3: glycine, diglycine and triglycine. Glycine (Sigma-Aldrich®, BioUltra, $\geq$ 99.0%), diglycine (Sigma-Aldrich®, BioUltra, $\geq$ 99.5%) and triglycine (Bachem, $>$ 99%) were used as received and stored under dry conditions until use. Three approximate concentrations were investigated for each oligomer ($\sim$ 0.1 m, 0.3 m and 0.5 m); except for triglycine, where only the lower two concentrations were accessible due to the solubility limit.

The molecular structures of the three oligoglycine peptides investigated in this chapter are displayed in Figure 7.2.

7.2.2 | Refractive Indices and Hamaker Constants

The refractive indices for the electrolytes were measured using the method outlined in Chapter 2. The Hamaker constants for all electrolytes reported in this chapter

(a) (b) (c)

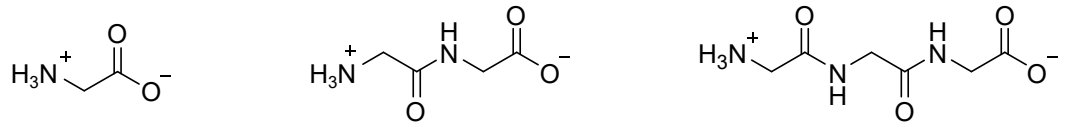

Figure 7.2: Molecular structures of the oligoglycine peptides investigated in this chapter: (a) glycine, (b) diglycine, (c) triglycine.

are shown in Table 7.1, and the displayed relative permittivity of the electrolytes were estimated using Equation 7.1:

$$\epsilon_{\mathrm{e}} = \epsilon_{\mathrm{r}}^{0} + \delta_{\mathrm{Gly}_n} c_{\mathrm{Gly}_n} \tag{7.1}$$

where $\epsilon_{\mathrm{r}}^{0}$ is the relative permittivity of water (78.4), δ_{Gly_n} is the dielectric increment of the oligoglycine and c is the oligoglycine concentration. The dielectric increments were obtained from literature, and we have taken δ_{Gly_1} to be 22.6 / m, δ_{Gly_2} to be 70.6 / m and δ_{Gly_3} to be 113.3 / m.[265]

Table 7.1: Parameters used for Hamaker constant calculations. Concentrations of oligoglycine c_{Gly_n}, refractive index n_{e}, relative permittivity ϵ_{e} and Hamaker constant A are shown.

Gly_n	c_{Gly_n} / m	n_{e}	ϵ_{e}	A / 10^{-20} J
Gly_1	0.10	1.3337	80.7	2.06
Gly_1	0.30	1.3363	85.2	2.02
Gly_1	0.44	1.3382	88.3	2.00
Gly_2	0.10	1.3350	85.5	2.04
Gly_2	0.30	1.3394	99.6	1.98
Gly_2	0.50	1.3440	113.7	1.93
Gly_3	0.10	1.3357	89.7	2.03
Gly_3	0.30	1.3422	112.4	1.95

7.3 | Surface Forces Measurements and Discussion

7.3.1 | Glycine Solutions

Initially, we begin with the measurement of the interaction free energy across solutions containing the single glycine unit. Results from measurements across three glycine concentrations are discussed in this chapter: 0.10 m, 0.30 m and 0.44 m. All three concentrations resulted in qualitatively similar, DLVO-like behaviour, and only the resulting measurement from the highest of these (0.44 m) is displayed here in Figure 7.3, along with its associated DLVO fit. Measurements across higher glycine concentrations were also performed, up to $\sim$ 1 m, and displayed similar DLVO-like behaviour.

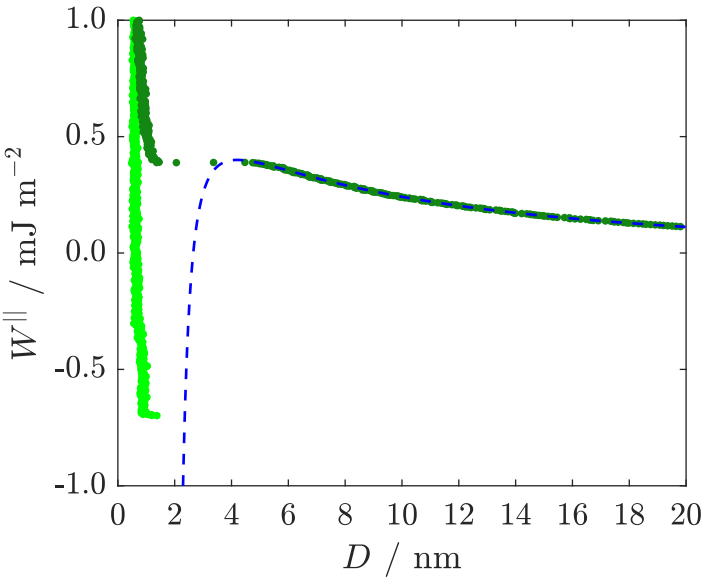

Figure 7.3: Measured interaction free energy as a function of surface separation across a solution containing 0.44 m glycine. The measurement upon approach of the surfaces is shown in dark green and that upon retraction is shown in light green. The DLVO fit is shown by the blue dashed curve, parameters for which are displayed in Table 7.2. This displayed measurement is qualitatively similar to the other glycine concentrations for which measurements were performed (up to $\sim$ 1 m).

Upon approach of the surfaces, they exhibit repulsion down to separations of $\sim$ 5 nm, at which point an attractive force results in spring instability and a jump to close surface separation. From this close surface separation, an attractive minimum was revealed upon retraction of the surfaces. As shown by the fit in Figure 7.3

all measured features are captured by the DLVO interaction, and no additional structural term is required. The resulting parameters from this DLVO fit, along with those for the two lower concentration, are displayed in Table 7.2.

Table 7.2: Parameters obtained from the DLVO fit to the measured interaction free energy across the glycine solutions, including the one shown in Figure 7.3. The fitted effective surface potential ψ_{eff}, Debye screening length κ_{D}^{-1}, charge regulation parameter p and offset to the zero surface separation D_0 are shown.

Gly_n	c_{Gly_1} / m	ψ_{eff} / mV	κ_{D}^{-1} / nm	p	D_0 / nm
Gly_1	0.10	62 ± 3	40 ± 13	0.92 ± 0.03	-1.4 ± 0.4
Gly_1	0.30	68 ± 2	37 ± 16	0.90 ± 0.00	-0.5 ± 0.1
Gly_1	0.44	48 ± 2	19 ± 3	0.86 ± 0.03	1.7 ± 0.3

7.3.2 | Diglycine Solutions

Next, we perform measurements across diglycine-containing solutions. These measurements are performed across solutions of similar concentration to those used to investigate glycine: 0.1 m, 0.3 m and 0.5 m. Interestingly, and in contrast to (mono)glycine, for this series of measurements there were notable differences in the structural features at small surface separations between the three concentrations. Owing to these differences, the measurements from all three concentrations are displayed in Figure 7.4; the parameters associated with the DLVO fits for each are shown in Table 7.3.

Table 7.3: Parameters obtained from the DLVO fit to the measured interaction free energy across the diglycine solutions shown in Figure 7.4. The fitted effective surface potential ψ_{eff}, Debye screening length κ_{D}^{-1}, charge regulation parameter p and offset to the zero surface separation D_0 are shown.

Gly_n	c_{Gly_2} / m	ψ_{eff} / mV	κ_{D}^{-1} / nm	p	D_0 / nm
Gly_2	0.10	65 ± 2	18 ± 4	0.90 ± 0.03	1.3 ± 0.5
Gly_2	0.29	64 ± 1	10 ± 1	0.86 ± 0.01	1.7 ± 0.3
Gly_2	0.50	57 ± 2	9.8 ± 0.9	0.89 ± 0.02	1.7 ± 0.2

At the lowest concentration (0.1 m, Figure 7.4 (a)), the interaction free energy profile is again 'DLVO-like' and no significant structural contributions are observed.

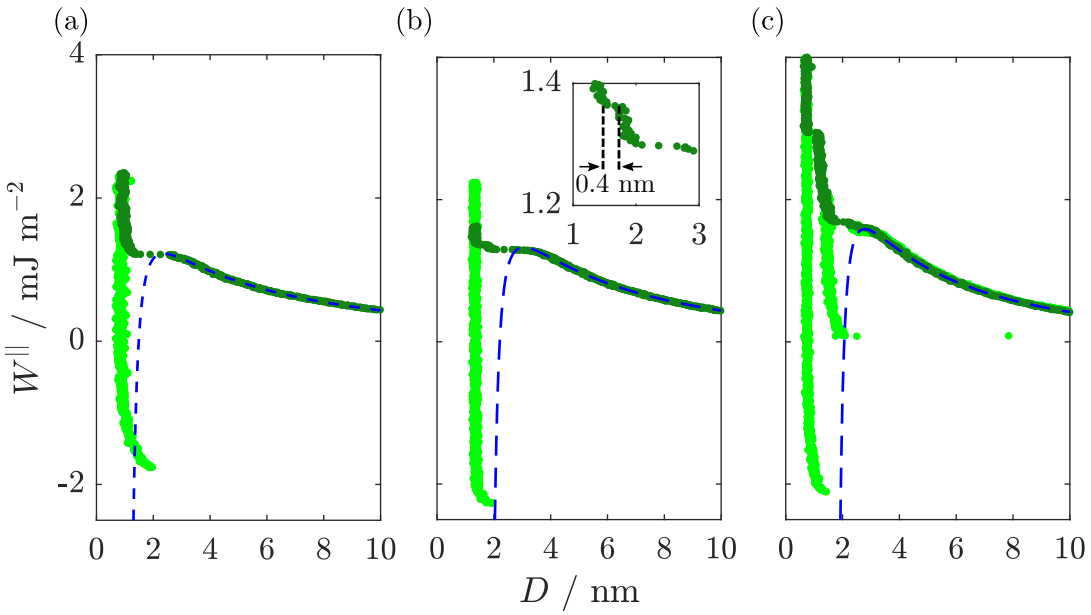

Figure 7.4: Measured interaction free energy as a function of surface separation across a diglycine-containing electrolytes: (a) 0.1 m, (b) 0.3 m and (c) 0.5 m. The measurement upon approach of the surfaces is shown in dark green and that upon retraction is shown in light green. The DLVO fit is shown by the blue dashed curve, parameters for which are displayed in Table 7.3.

Additional measurement runs (not presented here) were performed to confirm that no further structural features appeared at larger, positive interaction energies.

At the intermediate concentration (0.3 m, Figure 7.4 (b)), the double layer interaction is similarly seen along with an eventual van der Waals jump at smaller separations. However, at this slightly elevated concentration, an additional repulsive wall appears upon approach of the surfaces, before it gives way to an attractive force and the smallest surface separation is obtained. This step in the interaction profile measured upon approach of the surfaces is approximately 0.4 nm wide, and the inset displayed in the top right of the figure shows an expanded view of this feature. Owing to experimental constraints, it was not possible to measure a retraction from this layer due to the small force required to 'squeeze out' this layer. In a similar manner to the lowest concentration solution, additional measurement runs were performed to larger, positive interaction energies in order to ensure that additional features were not appearing at such energies (not presented here).

Finally, at the highest concentration (0.5 m, Figure 7.4 (c)), further structural

features appear in the full interaction profile. For clarity, an expanded view of Figure 7.4 (c) is shown in Figure 7.5. Approaching from large surface separations, a small step of size ~ 0.3 nm is seen directly after the double layer repulsion, rather than a van der Waals jump. Only a small force is required to squeeze through the layers, and therefore a fine resolution in $W^{||}$ is required to observe such features. Shallow minima are revealed upon retraction from both, as can be seen more clearly in the expanded view shown in the inset Figure 7.5. After the small step, two larger steps are revealed at larger values of $W^{||}$, of approximate size $\sim$ 0.5-0.6 nm. A minimum at $W^{||} \sim 0$ is revealed upon retraction from the first layer. A deeper minimum is revealed upon retraction from the smallest surface separation, at a similar value (~ -2 mJ m^{-2}) to the minima measured at the two lower concentrations.

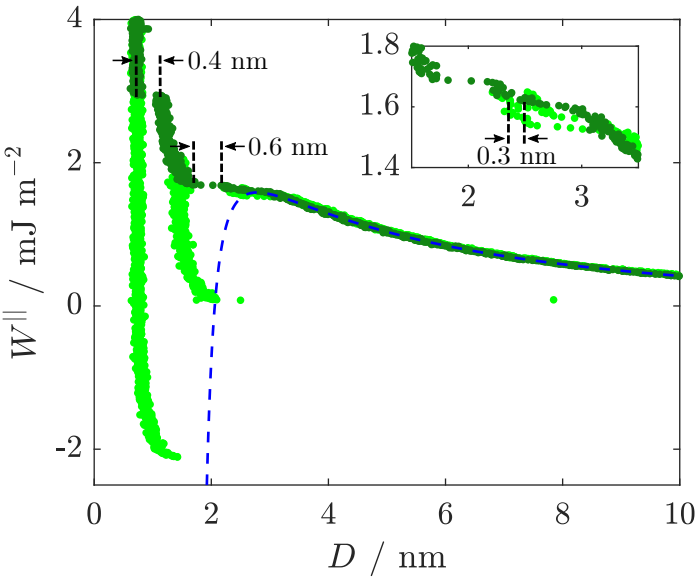

Figure 7.5: Expanded view of the measured interaction free energy across the 0.5 m diglycine electrolyte shown in Figure 7.4 (c). The structural features of interest are highlighted, including the 0.3 nm features which are shown in the inset.

7.3.3 | Triglycine Solutions

Finally, a measurement across a 0.1 m triglycine-containing solution is shown in Figure 7.6. This measurement was qualitatively similar to that recorded across a 0.3 m solution; therefore only the 0.1 m measurement is displayed. The parameters

for the DLVO fits for the two triglycine concentrations are shown in Table 7.4. No measurements across solutions at higher concentrations were possible due to the solubility limit of this oligopeptide.

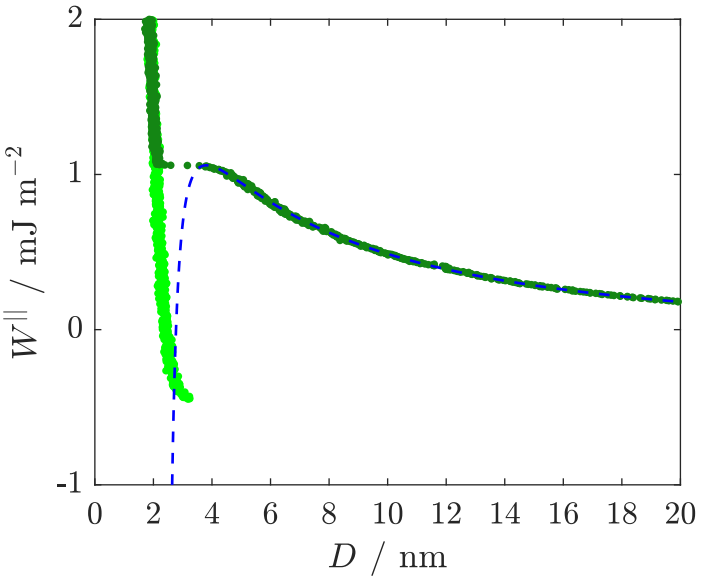

Figure 7.6: Measured interaction free energy as a function of surface separation across a triglycine-containing electrolyte (0.1 m). The measurement of interaction potential measured upon approach of the surfaces is shown in dark green, and that measured upon retraction is shown in light green. The DLVO fit is shown by the blue dashed curve. This displayed measurement is qualitatively similar to the other triglycine concentrations for which measurements were performed (0.3 m).

Table 7.4: Parameters obtained from the DLVO fit to the measured interaction free energy across the triglycine solutions, including the one shown in Figure 7.6. The fitted effective surface potential ψ_{eff}, Debye screening length κ_{D}^{-1}, charge regulation parameter p and offset to the zero surface separation D_0 are shown.

Gly_n	c_{Gly_3} / m	ψ_{eff} / mV	κ_{D}^{-1} / nm	p	D_0 / nm
Gly_3	0.10	65 ± 4	16 ± 2	0.89 ± 0.02	2.2 ± 0.3
Gly_3	0.29	60 ± 2	11 ± 3	0.88 ± 0.02	1.5 ± 0.1

The measurements across triglycine-containing solutions initially appear to be similar to those performed across solutions containing the single glycine monomer discussed in Section 7.3.1, as there are no obvious structural features in addition to the DLVO interactions. However, there are a few differences that should be explored further. Firstly, the attractive jump occurs over a smaller change in surface separation: $\Delta D = 1.6$ nm, compared to $\Delta D = 3.3$ nm in Figure 7.3. Further-

more, the separation at the closest approach of the surfaces is larger than that for the triglycine-containing solution, and additionally, the minimum in the interaction profile upon retraction of the surfaces is not as deep ($\sim$ -0.5 mJ m^{-2} compared to $\sim$ -2 mJ m^{-2}). This suggests a difference to the DLVO-like behaviour observed for glycine, which will be explored further in the following section.

7.3.4 | Oligoglycine Surface Structure

Considering the variation in the structural contribution to the interaction free energy at close surface separations, we see that: for $n = 1$, the measurement is DLVO-like; for $n = 2$, there is a concentration-dependent structural contribution at small surface separation; and for $n = 3$, the measurement appears to be DLVO-like, but there are some differences in the form of the interaction at small surface separations relative to $n = 1$ which are worth exploring further. The surface separation at the closest point of approach in the $n = 3$ measurement is at larger distances than for $n = 1$. This observation, in addition to the smaller jump distance and the reduced magnitude of the retraction minimum previously identified, suggests that for the measurement across triglycine solutions there exists a larger, more rigid film of fluid that cannot be expelled over the range of accessible forces in this measurement.

Assimilating these observations across the glycine series, it appears there is a trend towards structure features of increased rigidity at the interface. This trend can appear to be rationalised by invoking some of the ideas we introduced in Section 7.1.1, relating to the intermolecular interactions between oligoglycine units. However, before interrogating this trend any further, deeper analysis of molecular arrangement in these structures at the interfaces is required.

Since it is only for diglycine solutions that individual layers can be measured, it is this set of measurements we shall use initially in order to interpret the arrangement of molecules between the surfaces. At the intermediate concentration (0.3 m), the structural feature of $\sim$ 0.4 nm emerges at small surface separations. This lengthscale

is consistent with the width of the diglycine unit ($\sim$ 0.4 to 0.5 nm), rather than its end-to-end distance ($\sim$ 0.8 nm),[266] implying that this structural feature is due to a layer of diglycine units being expelled from between the surfaces, aligned such that their long axis is parallel to the flat surface.

This structural feature at small surface separations is also present at the higher concentration (0.5 m), but the jump occurs at higher repulsive energy, after a larger repulsive barrier. Such a change correlated with increasing concentration suggests that this difference is due to the extent of self-assembly of these molecules at the interface, and the layered structure is more favourably assembled at the higher concentrations, with greater accumulation of the molecules at the interface. Consistent with this is the additional step in the interaction profile that occurs at lower energies, at slightly larger surface separations. This step is of size $\sim$ 0.6 nm, a slightly larger value than that at smaller separations, but still not as large as the diglycine end-to-end distance. This suggests that the expulsion is still of predominately horizontally-aligned diglycine molecules, but the slight elongation of the step can be attributed to some disorder in the expelled film, or perhaps some hydrating water molecules.

At the higher concentration, there are an additional two layers that appear at even larger surface separations relative to the lower concentrations, and thus obscuring any observable impact of a van der Waals interaction relative to the lower concentrations. These structural features, shown most clearly in the inset to Figure 7.4, have a size of $\sim$ 0.3 nm. Akin to when these features have appeared in previous chapters, there presence are likely due to ordered water layers being expelled from between the surfaces. Such a conclusion seems feasible, as along a horizontally-aligned peptide backbone there are a number of sites to which water molecules can bind, and be templated across the horizontal surface. These subtle hydration layers could play a role in keeping the peptide layers separated and preventing the collapse of such units.

Finally, considering the measurement across a triglycine solution, we can explain the film of fluid at small surface separations which cannot be expelled by extrapolating from our discussion surrounding the mono- and diglycine results. As the number of glycine units increases along the series, there appears to be a greater driving force to assemble into ordered structures between the interfaces. For glycine, there are no observable multilayers; for diglycine, there are assembled layers that can be individually expelled. In the case of triglycine, it appears that there is a film comprising multiple layers of triglycine units, which are strongly adhered together, and tightly bound to the mica surface. This results in a measurement where no individual layers of molecules can be expelled, and close surface contact is not reached.

Summarising our findings and interpretations from this section, Figure 7.7 shows schematic cartoons illustrating the interfacial structures inferred from our surface forces measurements for the three glycine units. The observations from this series of measurements has provided a new insight into the behaviour of oligoglycine units in solution. As discussed in Section 7.1, previous works studying similar systems have concentrated on the balance between monomeric, solvated units, and aggregated, non-solvated units. In our work, we have perturbed this balance with the presence of a surface, with surface adsorption providing an additional layer of complexity to the overall equilibrium.

In light of the concentration-dependent behaviour observed most clearly for the measurements across diglycine solutions, an analogy can be drawn between the balance outlined for these oligoglycine systems and the behaviour of surfactant solutions which again displays concentration-dependent behaviour. In these systems, there exists an equilibrium between solution monomers, solution self-assembled structures (or aggregates) and surface-adsorbed species. In equilibrium, the chemical potential of each of the three surfactant phases must be equal resulting in different concentrations of each of the phase, where the ratio between the amounts of these phases varies as a function of the total concentration.

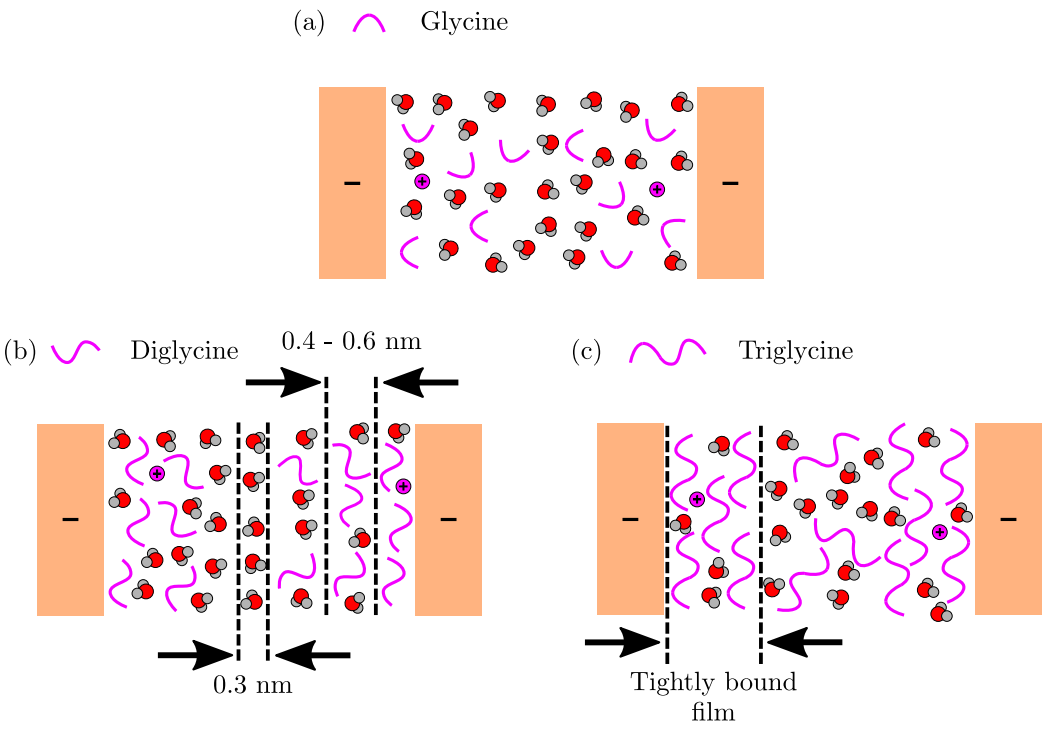

Figure 7.7: Cartoons illustrating the interfacial structures inferred from the surface forces measurements presented in this chapter.

In the case of the oligoglycines in solution, without a surface present, all units will be present in monomeric form at the lowest concentrations; as the concentration is increased, at a certain value aggregated structures will begin to form where this critical value increases with the length of the oligomer. In the presence of a surface where adsorption can take place, depending on the precise relative energetics of the different phases, there also exists a concentration where surface adsorption occurs, and self-assembled structures form at the interface. This critical concentration is again dependent on the length of the oligomer: in the case of $n = 1$, all concentrations studied in this work were lower than that at which surface features would be seen. For $n = 2$, the critical concentration is observed within those studied in this work, whereas for $n = 3$ the concentration is even lower, and surface adsorption is greatly favoured.

Where surface adsorption occurs, it is notable that it takes place with the oligoglycine units aligning parallel to the surface. This observation suggests that the favourable interactions are dominated by those along the peptide backbone, rather

than by the end groups of the oligoglycine units. Whilst this is inferred most clearly from the diglycine measurements, these interactions can be thought to dominate those between triglycine units, especially since the peptide backbone is longer. The backbone-dominated rather than end group-dominated interactions is also evidence that the conclusions drawn in this chapter in relation to oligoglycine interactions are relevant for longer units, and have implications for inter- or intra-peptide interactions in larger biomolecular structures.

7.4 | Summary

In this chapter, we have performed surface forces measurements across aqueous solutions containing glycine oligopeptides, a model peptide backbone and a common constituent of intrinsically disordered proteins or protein regions. We investigated three chain lengths of these glycine-containing units - glycine, diglycine, and triglycine - each at varying concentrations, up to 0.5 m, or 0.3 m for triglycine owing to limited solubility. This model system has been previously studied in order to investigate the interactions between these units computationally, but limited experimental results exist in the literature. Furthermore, surface forces measurements allows for the interrogation resulting from the perturbation to the balance of interactions due to the presence of a surface.

The measurements allowed for investigation of the peptide length and concentration dependence on the near-surface structures observed at small surface separations. We observed a clear oligomer size effect, and the concentration at which surface adsorption occurred was found to increase as a function of the chain length. This resulted in no observable surface structure when $n = 1$, structure appearing at an intermediate concentration when $n = 2$ and a thicker bound film of adsorbent at the interface when $n = 3$ which could not be expelled across the range of applied forces. The molecular arrangements of the assembled structures was resolved most clearly in the measurements across diglycine solutions, where diglycine units were

observed to adsorb with their long axis - along the peptide backbone - parallel with the surface. The highest concentration measurements across diglycine also revealed the presence of hydration layers, which could play a role in mediating the interaction between peptide layers, preventing the collapse of such units.

These results yield valuable information relating to the behaviour of peptide strands at surfaces, with relevance for the various natural processes and technological applications detailed at the beginning of the chapter which are underpinned by peptide-surface interactions, including those between IDPs or IDRs and other protein or membrane surfaces. Future work could build on these findings by increasing the complexity of the peptides or by modifying the surfaces to better mimic biological situations, such as the functionalising the mica surfaces with lipid membranes.

8 | Conclusions and Outlook

The cytosolic fluid is of fundamental importance to a variety of biochemical processes, and the makeup of this liquid is carefully tuned to balance osmotic stresses and maintain the structure and function of macromolecules in the cellular environment. However, the role of many of the individual osmolytes is in mediating cellular structures, and the interactions through which this is achieved, is still not fully understood. This thesis has investigated surface forces across, and structures within, a number of aqueous solutions containing a wide range of osmolytic constituents found in such fluids across the natural world. The surface force balance (SFB) has been used to gain an insight into the role played by these chemical species in modulating interactions between charged surfaces, with broad implications for understanding the colloidal contribution to stability between cellular particles. The sub-nanometre distance resolution of the SFB has also provided an insight to the surface interactions beyond mean-field predictions, revealing the behaviour of osmolytes at the charged surfaces and the influence on the molecular packing between the interfaces. Neutron and X-ray total scattering techniques were also used to study the bulk structure in such a model cytosol solution. In this final chapter, we provide a summary of the conclusions made in this thesis and present an outlook from this work.

Chapter 3 presented reference measurements of the interaction free energy across two simple electrolytes: pure water and a dilute KCl solution. These measurements were used to introduce the framework with which the mean field contributions to the interaction - the DLVO theory, comprising the electric double layer repulsion and the van der Waals attraction - can be interrogated. The significance of non-DVLO, structural contributions to the overall interaction at small surface separations was also emphasised, discussed in the context of the oscillatory hydration forces observed in the measurement across the KCl electrolyte.

Further surface forces measurements were presented in Chapter 4 in order to

interrogate the role played by two zwitterionic osmolytes, proline and trimethylglycine, in modulating interactions between charged surfaces. We showed that both osmolytes can act to enhance and maintain the electric double layer repulsion relative to pure water across a range of concentrations. Additionally, we illustrated that there exists an interplay between zwitterions and ions in mixtures of the two, most notably manifested in differing near-surface structural features. Across a range of concentrations in zwitterion-ion mixtures, for both proline and TMG, we demonstrated that structural features could be water-, zwitterion- or ion-dominated, or alternatively a DLVO-like profile could be observed, without any measurable surface structure. Finally, we interrogated the differences in the proline and TMG measurements, noting that proline more effectively enhanced the electric double layer repulsion and that the switch to zwitterion-layering occurred at a lower concentration for proline, linking both to a greater surface coverage per proline molecule.

The bulk structure of two aqueous electrolytes using neutron and X-ray total scattering was investigated in Chapter 5. The solutions contained TMG and either of the monovalent salts, KCl or NaCl, and various properties of the solution structure were interrogated, including the bulk water structure, solute hydration structures and, notably, the nature of TMG-cation interactions. We observed that the carboxylate group exhibited clear binding to the cations in solution, promoting head-to-head TMG-TMG interactions and TMG clustering. Study of the differences between the local structures in the potassium and sodium ion-containing solutions revealed that sodium ions were more localised at the carboxylate oxygen atoms, enabling more structurally ordered TMG associates.

A pair of protein stabilising and destabilising osmolytes, TMAO and urea, was investigated in Chapter 6 in order to determine their individual and combined effects on particle interactions. The results illustrated that TMAO, unlike urea, acted to disrupt the hydration forces that are otherwise present in the osmolyte-free background electrolyte, and such differences was linked to the differing molecular prop-

erties of the two osmolytes. A compromise between the two individual cases was seen in the mixture, with partial disruption of the near-surface structure, and an analogy is drawn between these results and the counteracting-osmolyte hypothesis.

Finally, a series of surfaces forces measurements across glycine oligopeptides were presented in Chapter 7, revealing the concentration and peptide length dependence on the observed interfacial structures. An analogous trend to that of oligoglycine solubility - which decreases with increasing chain length - was seen for the critical concentration at which surface adsorption and therefore the formation of self-assembled interfacial structures took place. The measurements on diglycine solutions revealed that the adsorbed molecules aligned with their peptide axis parallel to surfaces, and the measurement at the highest concentration revealed the presence of hydration layers which could act to prevent the aggregation of peptide layers.

Overall, the observations presented in this thesis reveal a wide suite of phenomena that can be exhibited by subtly tuning the composition of aqueous solutions. The discussions throughout this thesis have also revealed that a combination of frameworks and perspectives are required to fully appreciate the complexity of these systems. Sometimes, phenomena are best thought about and rationalised using ideas from physics: for example, we have shown various occasions where continuum theories can be used and mean-field effects dominate, such as the electric double layer repulsive and van der Waals attractive forces between charged surfaces. Other times, however, the specific chemistry and chemical interactions must be considered, such as for understanding the interactions that can dominate at small surface separations in our surface forces measurements. Biology, however, does not discriminate between scientific disciplines and all of the effects discussed in this thesis contribute to a toolbox which can be utilised to delicately tune interactions and build evolutionary strategies by living organisms, allowing survival across a wide range of ambient and extreme environments.

Appendices

A | The Role of Zwitterions in Model Cytosol Solutions - Supporting Data

In addition to the surface forces measurements performed on aqueous electrolytes containing proline that we presented in Chapter 4, either as the sole solute or with additional KCl, further measurements at different concentrations are presented here. The parameters associated with the calculation of the Hamaker constant for each of these measurements were displayed in Table 4.1, along with those displayed within the chapter.

0.35 m Pro

A measurement across a 0.35 m proline solution is displayed in Figure A.1. This measurement is qualitatively similar to measurement across the 0.90 m proline electrolyte displayed in Chapter 4 (Figure 4.4): we again observe a step in the interaction profile of size 0.5 nm at small surface separation, corresponding with the size of the proline molecule. The DLVO fit to the long-range interaction is also quantitatively similar to proline-only measurements, with similar values for the effective surface potential ($\psi_{\text{eff}} = 55 \pm 2$ mV), Debye screening length ($\kappa_{\text{D}}^{-1} = 34 \pm 7$ nm) and charge regulation ($p = 0.92 \pm 0.02$) parameters.

Table A.1: Parameters used for DLVO fits to the measured interaction free energy for the measurement in Figure A.1. The fitted effective surface potential ψ_{eff}, Debye screening length κ_{D}^{-1}, charge regulation parameter p, and offset to the zero surface separation D_0 are shown.

c_{Pro}/ m	ψ_{eff} / mV	κ_{D}^{-1} / nm	p	D_0 / nm
0.35	55 ± 2	34 ± 7	0.92 ± 0.02	0.0 ± 0.0

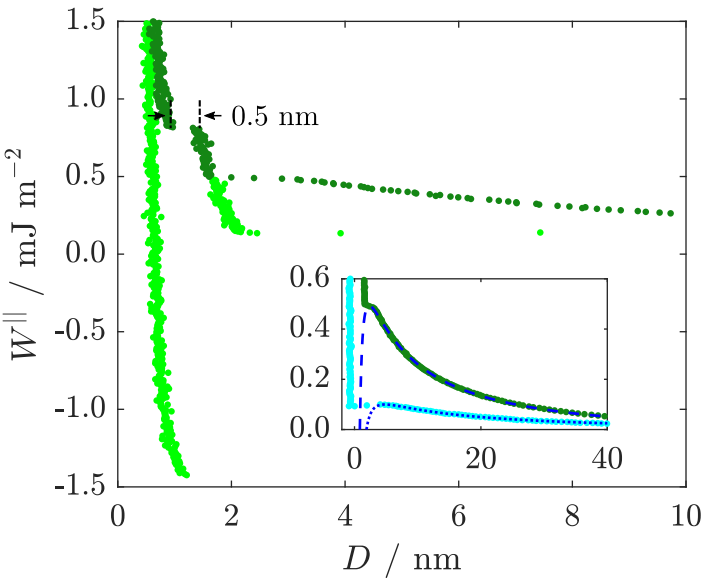

Figure A.1: Measured interaction free energy as a function of surface separation across a solution containing 0.35 m proline. The measurement upon approach of the surfaces is shown in dark green and that upon retraction is shown in light green. The DLVO fit is shown in the inset by the blue dashed curve, parameters for which are shown in Table A.1. The interaction across pure water is also shown in light blue in the inset for comparison, along with the associated DLVO fit shown by the dark blue dotted line.

0.33 m Pro + 0.001 m KCl

A measurement across a solution containing 0.33 m proline and 0.001 m KCl is displayed in Figure A.2. This measurement appears qualitatively similar to the high concentration proline measurements with a long-range repulsion, van der Waals attractive jump and structural feature in the approach interaction profile. However, the structural jump is of size 0.3 nm, and thus likely dominated by the packing of water molecules at the interface, akin to the structural feature observed in the measurement at the 0.01 m KCl concentration (Figure 4.5). The effective surface potential of the long-range attraction is similarly enhanced relative to the pure water case ($\psi_{\text{eff}} = 49 \pm 2$ mV); the Debye screening length is consistent with that for a 1:1 electrolyte containing 0.001 m KCl ($\kappa_{\text{D}}^{-1} = 11 \pm 1$ nm); and the charge regulation parameter is an intermediate value between the proline-only measurements and the 0.01 m KCl measurement, as discussed in the chapter ($p = 0.84 \pm 0.03$) .

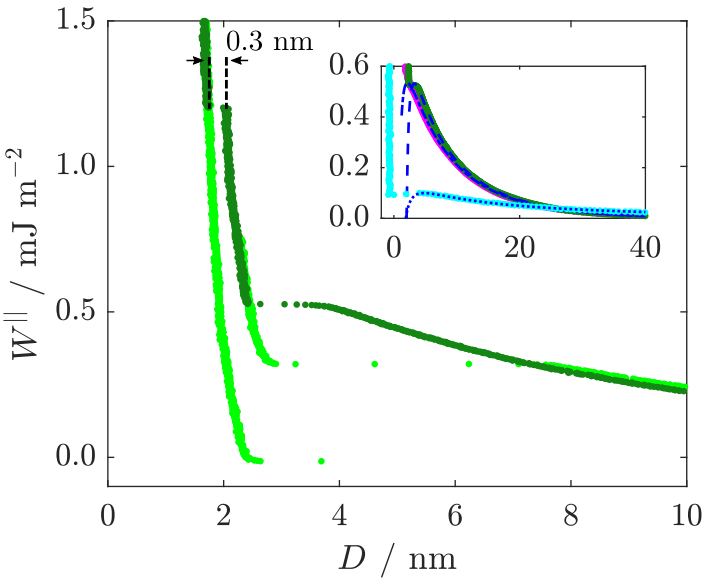

Figure A.2: Measured interaction free energy as a function of surface separation across a solution containing 0.33 m proline and 0.001 m KCl. The measurement upon approach of the surfaces is shown in dark green and that upon retraction is shown in light green. The DLVO fit is shown in the inset by the blue dashed curve. In the inset, the interaction across pure water is shown in light blue, along with its DLVO fit shown by the dark blue dotted line. The inset also shows the interaction profile for 0.001 m KCl displayed in magenta and the associated DLVO fit shown by the dark blue dash-dotted line. Parameters for the DLVO fits are displayed in Table A.2.

Table A.2: Parameters used for DLVO fits to the measured interaction free energy for the measurement in Figure A.2. The fitted effective surface potential ψ_{eff}, Debye screening length κ_{D}^{-1}, charge regulation parameter p, and offset to the zero surface separation D_0 are shown. The predicted Debye screening length $\kappa_{\text{D, pred}}^{-1}$ is also shown.

c_{Pro}/ m	c_{KCl}/ m	ψ_{eff} / mV	κ_{D}^{-1} / nm	p	D_0 / nm	$\kappa_{\text{D, pred}}^{-1}$ / nm
0.33	0.001	49 ± 2	11 ± 1	0.84 ± 0.03	1.4 ± 0.1	10

B | Bulk Structure and Ion Effects in Zwitterion Solutions - Supporting Data

To complement the structure factors displayed in Chapter 5, the experimentally measured (solid line) and simulated (dotted line) total radial distribution functions $G(r)$ factors for all of the seven neutron isotopic contrasts, in addition to that determined by X-ray diffraction, are shown in Figure B.1. Additionally, Figure B.2 shows the structure factor difference function $F_{\mathrm{exp}}(Q) - F_{\mathrm{sim}}(Q)$, illustrating the discrepancy between the simulated and experimentally-determined structure factor for each of the neutron and X-ray contrasts, for both of the investigated solutions.

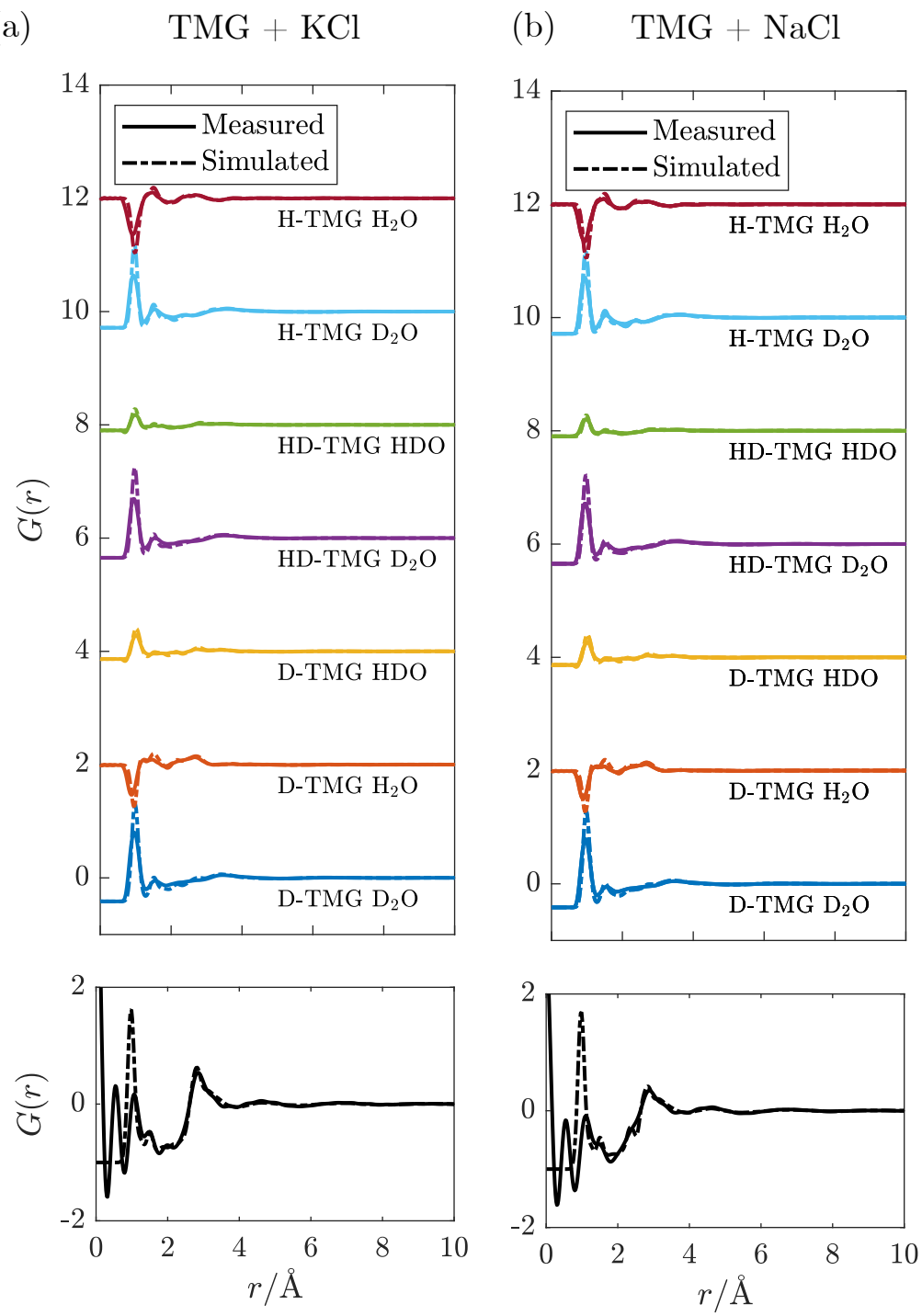

Figure B.1: Measured (solid lines) and simulated (dash-dotted lines) total radial distribution functions $G(r)$ for aqueous solutions containing (a) TMG + KCl (left) and (b) TMG + NaCl (right). Top: Total radial distribution functions obtained from neutron diffraction in seven isotopic contrasts; each dataset is vertically shifted for clarity. Bottom: Total radial distribution function $G(r)$ obtained from X-ray diffraction.

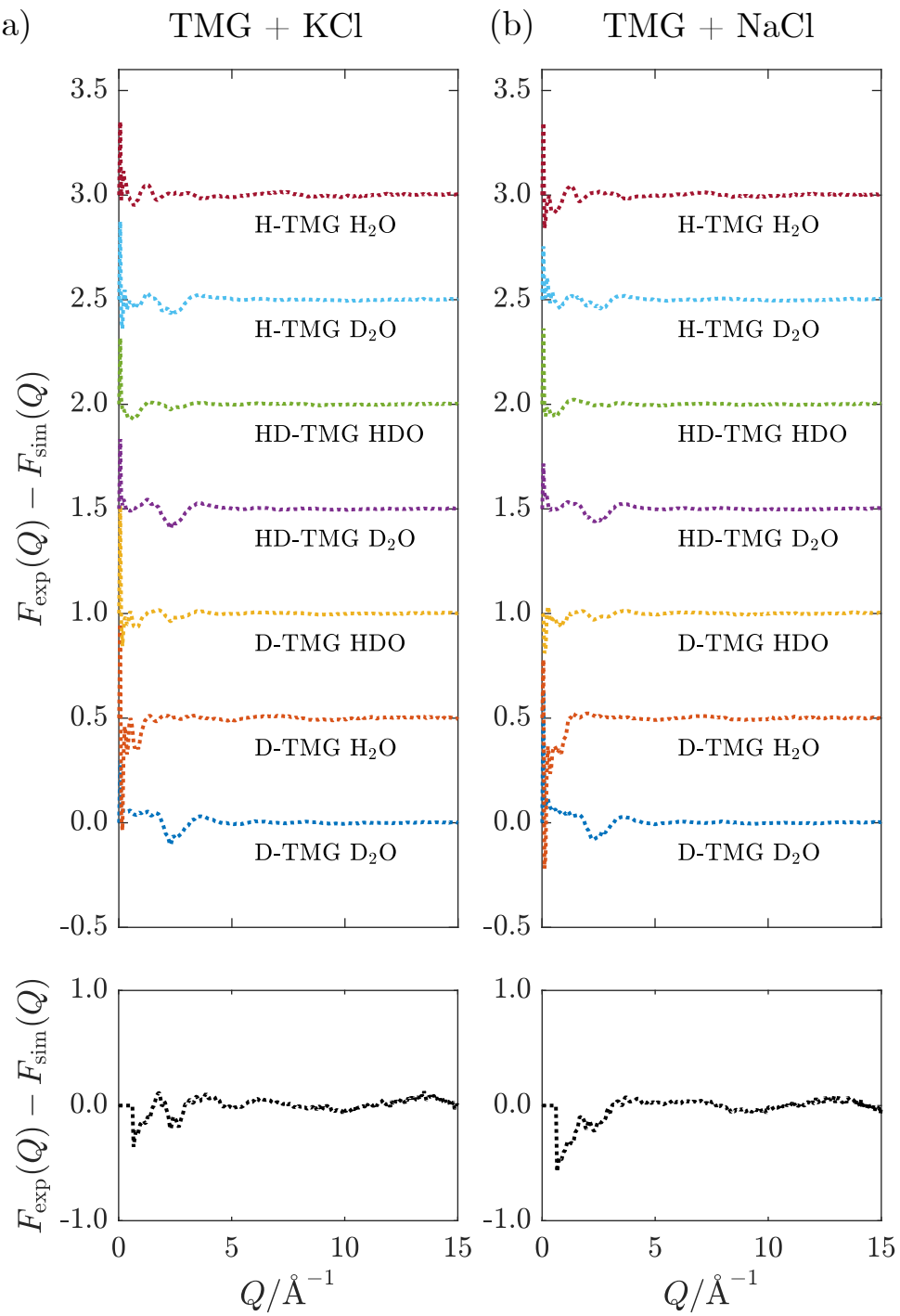

Figure B.2: Difference function illustrating the discrepancy between the simulated and experimentally-determined structure factors, $F_{\mathrm{exp}}(Q) - F_{\mathrm{sim}}(Q)$ for each of the neutron (top) and X-ray (bottom) contrasts. Data for both the TMG + KCl (left) and TMG + NaCl (right) solutions are shown. The neutron datasets are shifted for clarity.

C | Interactions Across Protein Stabilising and Destabilising Osmolyte Solutions - Supporting Data

Background KCl electrolyte

To support the surface forces measurements across TMAO-urea solutions presented in Chapter 6, a reference measurement across a solution containing 0.003 m KCl only - the background electrolyte used for all studied solutions in this chapter - is displayed in Figure C.1. The parameters associated for the DLVO fit are reported in Table C.1. The interaction potential is qualitatively similar to the measurement containing urea-only, displaying, on approach of the surfaces, a monotonic repulsion of a decay length dictated by the salt concentration within Debye-Hückel theory, and a series of repulsive walls separated by jumps of ~ 0.3 nm.

The resolution quality of this measurement is not as high as for that across the dilute KCl electrolyte discussed in Chapter 3. Therefore, the structural features of size ~ 0.3 nm cannot be very clearly resolved from the measured data obtained upon approach of the surfaces, shown in dark green in the figure. The structural features can instead be more clearly observed in the two retraction minima displayed in light green.

Table C.1: Parameters used for DLVO fits to the measured interaction free energy shown in Figure C.1. The fitted effective surface potential ψ_{eff}, Debye screening length κ_{D}^{-1}, charge regulation parameter p, and offset to the zero surface separation D_0 are shown.

c_{TMAO}/ m	c_{urea}/ m	c_{KCl}/ m	ψ_{eff} / mV	κ_{D}^{-1} / nm	p	D_0 / nm
-	-	0.003	57 ± 8	6.1 ± 1.1	0.67 ± 0.14	1.3 ± 0.9

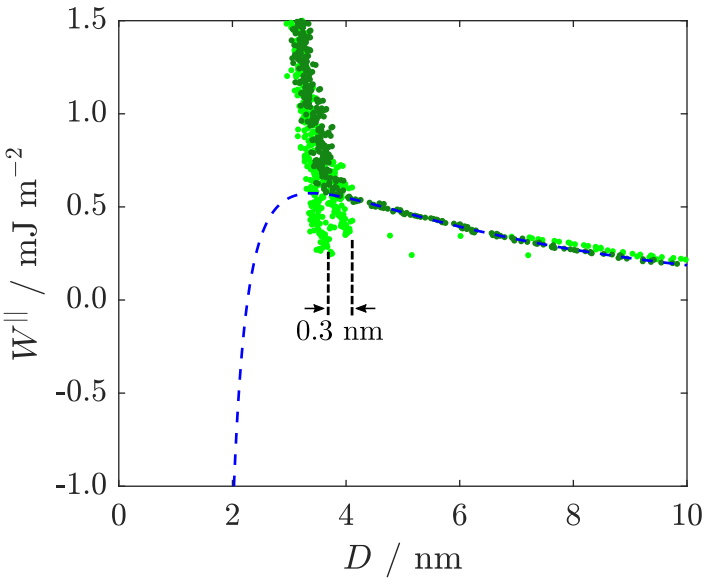

Figure C.1: Measured interaction free energy as a function of surface separation across a 0.003 m KCl background electrolyte. The measurement upon approach of the surfaces is shown in dark green, and that upon retraction is shown in light green. The DLVO fit is shown by the blue dashed curve, parameters for which are displayed in Table C.1.

Variations in measurements across the TMAO solution

As explained in Chapter 6, for a series of measurements across the TMAO-containing solution, there are significant fluctuations in both the magnitude of the repulsive barrier and the depth of the primary minimum. In contrast, the change in surface separation upon the jump to small separations is highly consistent between runs. A series of measurement runs illustrating these features is displayed in Figure C.2.

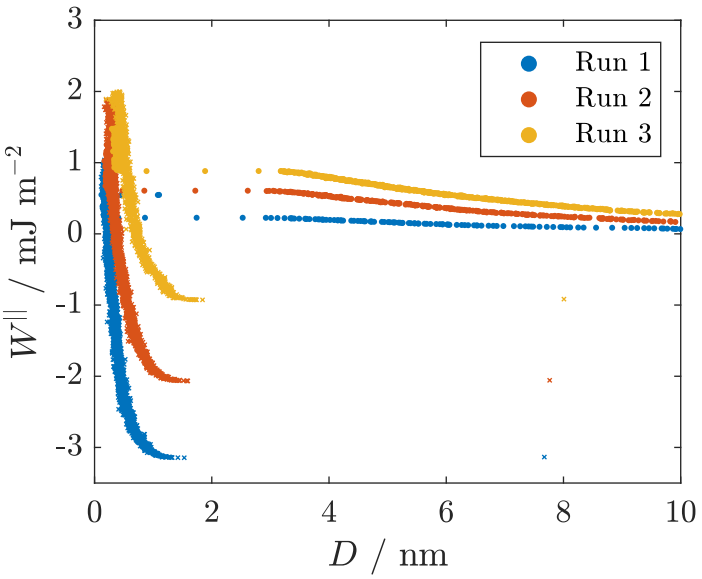

Figure C.2: Series of measurements of the interaction free energy as a function of surface separation across a solution containing 0.6 m TMAO and 0.003 m KCl. Repeat measurements are shown in different colours. Data obtained from approaching the surfaces is shown as filled circles, and from retracting the surfaces as crosses.

Bibliography

[1] Hallett, J. E.; Agg, K. J.; Perkin, S. *Proceedings of the National Academy of Sciences of the United States of America* **2023**, *120*, e2215585120.

[2] Agg, K. J.; Hallett, J. E.; Perkin, S. *Biophysical Journal* **2025**, *In Press*.

[3] Agg, K. J.; Groves, T. S.; Miao, S.; Fung, Y. K.; Alderman, O. L.; Headen, T. F.; Hughes, T. L.; Smith, G. N.; Youngs, T. G.; Tellam, J. P.; Chen, Y.; Perkin, S.; Hallett, J. E. *Chemical Science* **2025**, *16*, 6770–6779.

[4] Rothschild, L. J.; Mancinelli, R. L. *Nature* **2001**, *409*, 1092–1101.

[5] Banani, S. F.; Lee, H. O.; Hyman, A. A.; Rosen, M. K. *Nature Reviews Molecular Cell Biology 2017 18:5* **2017**, *18*, 285–298.

[6] Hyman, A. A.; Weber, C. A.; Jülicher, F. *Annual Review of Cell and Developmental Biology* **2014**, *30*, 39–58.

[7] Shin, Y.; Brangwynne, C. P. *Science* **2017**, *357*.

[8] Wennerström, H.; Oliveberg, M. *QRB Discovery* **2022**, *3*, e12.

[9] Beck, F. X.; Dörge, A.; Thurau, K. *Kidney and Blood Pressure Research* **1988**, *11*, 174–186.

[10] Nakanishi, T.; Turner, R. J.; Burg, M. B. *American Journal of Physiology-Renal Physiology* **1990**, *258*, F1061–F1067.

[11] Cayley, S.; Lewis, B. A.; Guttman, H. J.; Record, M. T. *Journal of Molecular Biology* **1991**, *222*, 281–300.

[12] Ollivier, B.; Caumette, P.; Garcia, J. L.; Mah, R. A. *Microbiological Reviews* **1994**, *58*, 27–38.

[13] Oren, A. *Journal of Industrial Microbiology and Biotechnology* **2002**, *28*, 56–63.

[14] Oren, A. *Canadian Journal of Microbiology* **1986**, *32*, 4–9.

[15] Martin, D. D.; Ciulla, R. A.; Roberts, M. F. *Applied and Environmental Microbiology* **1999**, *65*, 1815–1825.

[16] Cayley, S.; Record, M. T. *Biochemistry* **2003**, *42*, 12596–12609.

[17] Yancey, P. H.; Clark, M. E.; Hand, S. C.; Bowlus, R. D.; Somero, G. N. *Science*

1982, *217*, 1214–1222.

[18] Roberts, M. F. *Saline Systems* **2005**, *1*, 1–30.

[19] Santos, H.; Costa, M. S. D. *Environmental Microbiology* **2002**, *4*, 501–509.

[20] Deole, R.; Hoff, W. D. *Scientific Reports* **2020**, *10*, 1–10.

[21] Oren, A.; Heldal, M.; Norland, S.; Galinski, E. A. *Extremophiles* **2002**, *6*, 491–498.

[22] Oren, A.; Heldal, M.; Norland, S. *Canadian Journal of Microbiology* **1997**, *43*, 588–592.

[23] Yancey, P. H. *Journal of Experimental Biology* **2005**, *208*, 2819–2830.

[24] Hofmeister, F. *Archiv für experimentelle Pathologie und Pharmakologie* **1888**, *24*, 247–260.

[25] Gurau, M. C.; Lim, S. M.; Castellana, E. T.; Albertorio, F.; Kataoka, S.; Cremer, P. S. *Journal of the American Chemical Society* **2004**, *126*, 10522–10523.

[26] Gregory, K. P.; Wanless, E. J.; Webber, G. B.; Craig, V. S.; Page, A. J. *Chemical Science* **2021**, *12*, 15007–15015.

[27] Senske, M.; Constantinescu-Aruxandei, D.; Havenith, M.; Herrmann, C.; Weingärtner, H.; Ebbinghaus, S. *Physical Chemistry Chemical Physics* **2016**, *18*, 29698–29708.

[28] Schneck, E.; Horinek, D.; Netz, R. R. *Journal of Physical Chemistry B* **2013**, *117*, 8310–8321.

[29] Israelachvili, J. N. *Intermolecular and Surface Forces*, 3rd ed.; Academic Press, 2011.

[30] Smith, A. M.; Lee, A. A.; Perkin, S. *Journal of Physical Chemistry Letters* **2016**, *7*, 2157–2163.

[31] Gebbie, M. A.; Smith, A. M.; Dobbs, H. A.; Lee, A. A.; Warr, G. G.; Banquy, X.; Valtiner, M.; Rutland, M. W.; Israelachvili, J. N.; Perkin, S.; Atkin, R. *Chemical Communications* **2017**, *53*, 1214–1224.

[32] Fung, Y. K.; Perkin, S. *Faraday Discussions* **2023**, *246*, 370–386.

[33] Groves, T. S.; Perkin, S. *Faraday Discussions* **2024**, *253*, 193–211.

[34] Björneholm, O.; Hansen, M. H.; Hodgson, A.; Liu, L. M.; Limmer, D. T.; Michaelides, A.; Pedevilla, P.; Rossmeisl, J.; Shen, H.; Tocci, G.; Tyrode, E.; Walz, M. M.; Werner, J.; Bluhm, H. *Chemical Reviews* **2016**, *116*, 7698–7726.

[35] Putnis, C. V.; Ruiz-Agudo, E. *Elements* **2013**, *9*, 177–182.

[36] Sposito, G. *The Chemistry of Soils*; Oxford University Press, 2016.

[37] Tarbuck, T. L.; Richmond, G. L. *Journal of the American Chemical Society* **2006**, *128*, 3256–3267.

[38] Bartels-Rausch, T. et al. *Atmospheric Chemistry and Physics* **2014**, *14*, 1587–1633.

[39] Zhou, H. X.; Pang, X. *Chemical Reviews* **2018**, *118*, 1691–1741.

[40] Nguyen, T. H.; Zhang, C.; Weichselbaum, E.; Knyazev, D. G.; Pohl, P.; Carloni, P. *PLOS ONE* **2018**, *13*, e0193454.

[41] Aurbach, D.; Markovsky, B.; Salitra, G.; Markevich, E.; Talyossef, Y.; Koltypin, M.; Nazar, L.; Ellis, B.; Kovacheva, D. *Journal of Power Sources* **2007**, *165*, 491–499.

[42] Varcoe, J. R.; Atanassov, P.; Dekel, D. R.; Herring, A. M.; Hickner, M. A.; Kohl, P. A.; Kucernak, A. R.; Mustain, W. E.; Nijmeijer, K.; Scott, K.; Xu, T.; Zhuang, L. *Energy & Environmental Science* **2014**, *7*, 3135–3191.

[43] Nishida, K.; Anada, T.; Tanaka, M. *Advanced Drug Delivery Reviews* **2022**, *186*, 114310.

[44] Helmholtz, H. *Annalen der Physik* **1853**, *165*, 211–233.

[45] Gouy, M. *Journal de Physique Théorique et Appliquée* **1910**, *9*, 457–468.

[46] Chapman, D. L.

[47] Stern, O. *Zeitschrift für Elektrochemie und angewandte physikalische Chemie* **1924**, *30*, 508–516.

[48] Grahame, D. C. *Chemical Reviews* **1947**, *41*, 441–501.

[49] Conway, B. E.; Bockris, J. O.; Ammar, I. A. *Transactions of the Faraday Society* **1951**, *47*, 756–766.

[50] Bockris, J. O.; Devanathan, M. A. V.; Müller, K. *Proceedings of the Royal Society of London. Series A. Mathematical and Physical Sciences* **1963**, *274*, 55–79.

[51] Derjaguin, B.; Landau, L. *Progress in Surface Science* **1993**, *43*, 30–59.

[52] Verwey, E. J. *Journal of Physical and Colloid Chemistry* **1947**, *51*, 631–636.

[53] Gonella, G.; Backus, E. H.; Nagata, Y.; Bonthuis, D. J.; Loche, P.; Schlaich, A.; Netz, R. R.; Kühnle, A.; McCrum, I. T.; Koper, M. T.; Wolf, M.; Winter, B.; Meijer, G.; Campen, R. K.; Bonn, M. *Nature Reviews Chemistry* **2021**, *5*, 466–485.

[54] Fisher, M. E.; Wiodm, B. *The Journal of Chemical Physics* **1969**, *50*, 3756–3772.

[55] Attard, P. *Physical Review E* **1993**, *48*.

[56] Hayler, H. J.; Groves, T. S.; Guerrini, A.; Southam, A.; Zheng, W.; Perkin, S. *Reports on Progress in Physics* **2024**, *87*, 046601.

[57] Bailey, A. I.; Courtney-Pratt, J. *Proceedings of the Royal Society of London. Series A. Mathematical and Physical Sciences* **1955**, *227*, 500–515.

[58] Tabor, D.; Winterton, R. H. *Nature* **1968**, *219*, 1120–1121.

[59] Israelachvili, J. N.; Tabor, D. *Proceedings of the Royal Society of London. A. Mathematical and Physical Sciences* **1972**, *331*, 19–38.

[60] Israelachvili, J. N.; Adams, G. E. *Nature* **1976**, *262*, 774–776.

[61] Klein, J.; Kumacheva, E. *The Journal of Chemical Physics* **1998**, *108*, 6996.

[62] Christenson, H. K.; Phys, J. C. *The Journal of Chemical Physics* **1983**, *78*, 6906–6913.

[63] Horn, R. G.; Israelachvili, J. N. *The Journal of Chemical Physics* **1981**, *75*, 1400–1411.

[64] Israelachvili, J. N.; Adams, G. E. *Journal of the Chemical Society, Faraday Transactions 1: Physical Chemistry in Condensed Phases* **1978**, *74*, 975–1001.

[65] Perkin, S.; Albrecht, T.; Klein, J. *Physical Chemistry Chemical Physics* **2010**, *12*, 1243–1247.

[66] Luckham, P. F.; Klein, J. *Macromolecules* **1985**, *18*, 721–728.

[67] Horn, R. G.; Israelachvili, J. N.; Perez, E. *Journal de Physique* **1981**, *42*, 39–52.

[68] Briscoe, W. H.; Titmuss, S.; Tiberg, F.; Thomas, R. K.; McGillivray, D. J.; Klein, J. *Nature* **2006**, *444*, 191–194.

[69] Engers, C. D. V.; Balabajew, M.; Southam, A.; Perkin, S. *Review of Scientific Instruments* **2018**, *89*, 123901.

[70] Southam, A. The behaviour and charging dynamics of concentrated electrolytes in confinement under potential control. 2022.

[71] Britton, J.; Cousens, N. E.; Coles, S. W.; Engers, C. D. V.; Babenko, V.; Murdock, A. T.; Koós, A.; Perkin, S.; Grobert, N. *Langmuir* **2014**, *30*, 11485–11492.

[72] van Engers, C. The graphene surface force balance. 2018.

[73] Connor, J. N.; Horn, R. G. *Langmuir* **2001**, *17*, 7194–7197.

[74] Israelachvili, J.; Pashley, R. *Nature* **1982**, *300*, 341–342.

[75] Raviv, U.; Giasson, S.; Kampf, N.; Gohy, J. F.; Jéröme, R.; Klein, J. *Nature* **2003**, *425*, 163–165.

[76] Weiss, H.; Cheng, H. W.; Mars, J.; Li, H.; Merola, C.; Renner, F. U.; Honkimäki, V.; Valtiner, M.; Mezger, M. *Langmuir* **2019**, *35*, 16679–16692.

[77] Metropolis, N.; Rosenbluth, A. W.; Rosenbluth, M. N.; Teller, A. H.; Teller, E. *The Journal of Chemical Physics* **1953**, *21*, 1087–1092.

[78] Allen, M. P.; Tildesley, D. J. *Computer Simulation of Liquids*, 2nd ed.; Oxford University Press, 2017.

[79] Metropolis, N.; Ulam, S. *Journal of the American Statistical Association* **1949**, *44*, 335–341.

[80] Youngs, T. *Molecular Physics* **2019**, *117*, 3464–3477.

[81] Perkin, S.; Chai, L.; Kampf, N.; v, U.; Briscoe, W.; Dunlop, I.; Titmuss, S.; Seo, M.; Kumacheva, E.; Klein, J. *Langmuir* **2006**, *22*, 6142–6152.

[82] Tolansky, S. S. *An introduction to interferometry*; Longmans, Green, 1955.

[83] Israelachvili, J. N. *Journal of Colloid and Interface Science* **1973**, *44*, 259–272.

[84] Meggers, W. F.; Corliss, C. H.; Scribner, B. F. *Tables of spectral-line intensities*; National Bureau of Standards, 1961.

[85] Clarkson, M. T. *Journal of Physics D: Applied Physics* **1989**, *22*, 475.

[86] Derjaguin, B. *Kolloid-Zeitschrift* **1934**, *69*, 155–164.

[87] Chan, D. Y. C.; Horn, R. G. *The Journal of Chemical Physics* **1985**, *83*, 5311–5324.

[88] Young, T. *Philosophical Transactions of the Royal Society of London* **1802**, *92*, 12–48.

[89] Sivia, D. *Elementary Scattering Theory*, 1st ed.; Oxford University Press, 2011.

[90] Chadwick, J. *Nature* **1932**, *129*, 312–312.

[91] Chadwick, J. *Proceedings of the Royal Society of London. Series A, Containing Papers of a Mathematical and Physical Character* **1932**, *136*, 692–708.

[92] De Broglie, L. *Nature* **1923**, *112*, 540–540.

[93] De Broglie, L. *Annales de Physique* **1925**, *10*, 22–128.

[94] Shull, C. G. *Physical Review* **1969**, *179*, 752.

[95] Findlay, D.; Thomason, J.; Fletcher, S.; de Laune, R.; Cooper, E. A Practical Guide to the ISIS Neutron and Muon Source. 2021.

[96] Bowron, D. T.; Soper, A. K.; Jones, K.; Ansell, S.; Birch, S.; Norris, J.; Perrott, L.; Riedel, D.; Rhodes, N. J.; Wakefield, S. R.; Botti, A.; Ricci, M. A.; Grazzi, F.; Zoppi, M. *Review of Scientific Instruments* **2010**, *81*, 33905.

[97] Sears, V. F. *Neutron News* **1992**, *3*, 26–37.

[98] Knoll, G. F. *Radiation Detection and Measurement*, 3rd ed.; 2000.

[99] Soper, A. K. GudrunN and GudrunX: Programs for correcting raw neutron and x-ray total scattering data to differential cross section. 2012.

[100] Mayers, J. *Nuclear Instruments and Methods In Physics Research* **1984**, *221*.

[101] Compton, A. H. *Physical Review* **1923**, *21*, 483–502.

[102] Hahn, M.; Savin, D. W.; Tang, B.; Zank, G. P.; Kolobov, V. I.; Mccall, G. H. *Journal of Physics D: Applied Physics* **1982**, *15*, 823.

[103] Soper, A. K. *Physical Review B - Condensed Matter and Materials Physics* **2005**, *72*, 104204.

[104] McGregor, J.; Li, R.; Zeitler, J. A.; D'Agostino, C.; Collins, J. H.; Mantle, M. D.; Manyar, H.; Holbrey, J. D.; Falkowska, M.; Youngs, T. G.; Hardacre, C.; Stitt, E. H.; Gladden, L. F. *Physical Chemistry Chemical Physics* **2015**, *17*, 30481–30491.

[105] Hammond, O. S.; Bowron, D. T.; Edler, K. J.; Hammond, S.; Edler, K. J.; owron, D. T. B. *Angewandte Chemie International Edition* **2017**, *56*, 9782–9785.

[106] Miao, S.; Imberti, S.; Atkin, R.; Warr, G. *Journal of Molecular Liquids* **2022**, *351*, 118599.

[107] Alderman, O. L.; Hannon, A. C.; Holland, D.; Feller, S.; Lehr, G.; Vitale, A. J.; Hoppe, U.; Zimmerman, M. V.; Watenphul, A. *Physical Chemistry Chemical Physics* **2013**, *15*, 8506–8519.

[108] Trefalt, G.; Behrens, S. H.; Borkovec, M. *Langmuir* **2016**, *32*, 380–400.

[109] Smith, A. M.; Borkovec, M.; Trefalt, G. *Advances in Colloid and Interface Science* **2020**, *275*, 102078.

[110] Carnie, S. L.; Chan, D. Y. *Journal of Colloid and Interface Science* **1993**, *161*,

260–264.

[111] Pericet-Camara, R.; Papastavrou, G.; Behrens, S. H.; Borkovec, M. *Journal of Physical Chemistry B* **2004**, *108*, 19467–19475.

[112] Hamaker, H. C. *Physica* **1937**, *4*, 1058–1072.

[113] Lifshitz, E. M. *Journal of Experimental and Theoretical Physics* **1956**, *2*, 73–83.

[114] Fernández, D. P.; Mulev, . Y.; Goodwin, . A. R. H.; Sengers, . J. M. H. L.; Ferncindez, D. P.; Mulev, Y.; Goodwine, A. R. H.; Sengers, J. M. H. L. *Journal of Physical and Chemical Reference Data* **1995**, *24*, 33–70.

[115] Poppa, H.; Elliot, A. G. *Surface Science* **1971**, *24*, 149–163.

[116] Dowsett, M. G.; King, R. M.; Parker, E. H. *Journal of Vacuum Science and Technology* **1977**, *14*, 711–717.

[117] Christenson, H. K.; Thomson, N. H. *Surface Science Reports* **2016**, *71*, 367–390.

[118] Pashley, R. M. *Advances in Colloid and Interface Science* **1982**, *16*, 57–62.

[119] Raviv, U.; Laurat, P.; Klein, J. *Nature* **2001**, *413*, 51–54.

[120] Raviv, U.; Laurat, P.; Klein, J. *The Journal of Chemical Physics* **2002**, *116*, 5167.

[121] Klein, J.; Raviv, U.; Perkin, S.; Kampf, N.; Chai, L.; Giasson, S. *Journal of Physics: Condensed Matter* **2004**, *16*, S5437.

[122] Raviv, U.; Perking, S.; Laurat, P.; Klein, J. *Langmuir* **2004**, *20*, 5322–5332.

[123] Pashley, R. M. *Journal of Colloid and Interface Science* **1981**, *83*, 531–546.

[124] Israelachvili, J. N.; Pashley, R. M. *Nature* **1983**, *306*, 249–250.

[125] Pashley, R. M.; Israelachvili, J. N. *Journal of Colloid and Interface Science* **1984**, *101*, 511–523.

[126] Derjaguin, B. V.; Churaev, N. V. *Journal of Colloid And Interface Science* **1974**, *49*.

[127] Viani, B. E.; Low, P. F.; Roth, C. B. *Journal of Colloid and Interface Science* **1983**, *96*, 229–244.

[128] LeNeveu, D. M.; Rand, R. P. *Biophysical Journal* **1977**, *18*, 209–230.

[129] Lis, L. J.; McAlister, M.; Fuller, N.; Rand, R. P.; Parsegian, V. A. *Biophysical Journal* **1982**, *37*, 657–665.

[130] Siretanu, I.; van Lin, S. R.; Mugele, F. *Faraday Discussions* **2023**, *246*, 274–295.

[131] Smith, A. M.; Lee, A. A.; Perkin, S. *Physical Review Letters* **2017**, *118*, 096002.

[132] Israelachvili, J.; Wennerström, H. *Nature* **1996**, *379*, 219–225.

[133] Govrin, R.; Schlesinger, I.; Tcherner, S.; Sivan, U. *Journal of the American Chemical Society* **2017**, *139*, 15013–15021.

[134] Govrin, R.; Tcherner, S.; Obstbaum, T.; Sivan, U. *Journal of the American Chemical Society* **2018**, *140*, 14206–14210.

[135] Govrin, R.; Obstbaum, T.; Sivan, U. *Journal of the American Chemical Society* **2019**, *141*, 13311–13314.

[136] Ridwan, M. G.; Shrestha, B. R.; Maharjan, N.; Mishra, H. *Journal of Physical Chemistry B* **2022**, *126*, 1852–1860.

[137] Slama, I.; Abdelly, C.; Bouchereau, A.; Flowers, T.; Savouré, A. *Annals of Botany* **2015**, *115*, 433–447.

[138] Szabados, L.; Savouré, A. *Trends in Plant Science* **2010**, *15*, 89–97.

[139] Hayat, S.; Hayat, Q.; Alyemeni, M. N.; Wani, A. S.; Pichtel, J.; Ahmad, A. *Plant Signaling & Behavior* **2012**, *7*, 1456–1466.

[140] Shafi, A.; Zahoor, I.; Mushtaq, U. *Salt Stress, Microbes, and Plant Interactions: Mechanisms and Molecular Approaches: Volume 2* **2019**, 269–300.

[141] Grgac, R.; Rozsypal, J.; Marteaux, L. D.; Stětina, T.; Kośtal, V. *Proceedings of the National Academy of Sciences of the United States of America* **2022**, *119*, e2211744119.

[142] Stewart, G. R.; Lee, J. A. *Planta* **1974**, *120*, 279–289.

[143] Liang, X.; Zhang, L.; Natarajan, S. K.; Becker, D. F. *Antioxidants and Redox Signaling* **2013**, *19*, 998–1011.

[144] Moukhtari, A. E.; Cabassa-Hourton, C.; Farissi, M.; Savouré, A. *Frontiers in Plant Science* **2020**, *11*, 1127.

[145] Yoshiba, Y.; Kiyosue, T.; Nakashima, K.; Yamaguchi-Shinozaki, K.; Shinozaki, K. *Plant and Cell Physiology* **1997**, *38*, 1095–1102.

[146] Mekonnen, M. M.; Hoekstra, A. Y. *Science Advances* **2016**, *2*.

[147] Ladeiro, B. *Journal of Botany* **2012**, *2012*.

[148] Zhang, H.-X.; Blumwald, E. *Nature Biotechnology* **2001**, *19*, 765–768.

[149] Winkler, P. M.; Siri, C.; Buczkowski, J.; Silva, J. V.; Bovetto, L.; Schmitt, C.; Stellacci, F. *Journal of Physical Chemistry B* **2024**, *128*, 7199–7207.

[150] Xu, X.; Stellacci, F. *Journal of Physical Chemistry Letters* **2024**, *15*, 7154–7160.

[151] Xu, X.; Rebane, A. A.; Julia, L. R.; Rosowski, K. A.; Dufresne, E. R.; Stellacci, F. *Proceedings of the National Academy of Sciences of the United States of America* **2024**, *121*, e2407633121.

[152] Yancey, P. H. *Science Progress* **2004**, *87*, 1–4.

[153] Imhoff, J. F.; Rodriguez-Valera, F. *Journal of Bacteriology* **1984**, *160*, 478–479.

[154] Lawson-Yuen, A.; Levy, H. L. *Molecular Genetics and Metabolism* **2006**, *88*, 201–207.

[155] Ticak, T.; Kountz, D. J.; Girosky, K. E.; Krzycki, J. A.; Ferguson, D. J. *Proceedings of the National Academy of Sciences of the United States of America* **2014**, *111*, E4668–E4676.

[156] Obeid, R. *Nutrients* **2013**, *5*, 3481–3495.

[157] The influence of proline on surface interactions in aqueous solutions (data) - Oxford University Research Archive. `https://doi.org/10.5287/ora-00xxnmb7z`.

[158] Zwitterions fine-tune interactions in electrolyte solutions (data) - Oxford University Research Archive. `https://doi.org/10.5287/bodleian:BROE4obpd`.

[159] Chen, T.; Hefter, G.; Buchner, R. *Journal of Physical Chemistry A* **2003**, *107*, 4025–4031.

[160] Edsall, J. T.; Wyman, J. *Journal of the American Chemical Society* **1935**, *57*, 1964–1975.

[161] Kirchnerova, J.; Parrel, P. G.; Edward, J. T.; Shida, T.; Hamill, W. H.; Phys, J. C.; Franklin, J. L.; Dillard, J. G.; Rosenstock, M.; Herron, J. T.; Draxl, K.; Field, F. H.; Farrell, P. G. *Journal of Physical Chemistry* **1976**, *80*, 1974–1980.

[162] Wennerström, H.; Estrada, E. V.; Danielsson, J.; Oliveberg, M. *Proceedings of the National Academy of Sciences of the United States of America* **2020**, *117*, 10113–10121.

[163] Koenig, J. J.; Neudörfl, J. M.; Hansen, A.; Breugst, M. *Acta Crystallographica Section E: Crystallographic Communications* **2018**, *74*, 1067–1070.

[164] Coles, S. W.; Smith, A. M.; Fedorov, M. V.; Hausen, F.; Perkin, S. *Faraday Discussions* **2017**, *206*, 427–442.

[165] Sirdeshmukh, D.; Sirdeshmukh, L.; Subhadra, K. *Alkali Halides: A Handbook of Physical Properties*, 1st ed.; Springer Berlin, Heidelberg, 2001.

[166] Kapustin, E. A.; Minkov, V. S.; Boldyreva, E. V. *Physical Chemistry Chemical Physics* **2015**, *17*, 3534–3543.

[167] Soper, A. K. *Experimental Methods in the Physical Sciences* **2017**, *49*, 135–211.

[168] Soper, A. K. *Pure and Applied Chemistry* **2010**, *82*, 1855–1867.

[169] Soper, A. K. *Journal of Physical Chemistry B* **2011**, *115*, 14014–14022.

[170] Soper, A. K.; Weckström, K. *Biophysical Chemistry* **2006**, *124*, 180–191.

[171] Mancinelli, R.; Botti, A.; Bruni, F.; Ricci, M. A.; Soper, A. K. *Journal of Physical Chemistry B* **2007**, *111*, 13570–13577.

[172] Mancinelli, R.; Botti, A.; Bruni, F.; Ricci, M. A.; Soper, A. K. *Physical Chemistry Chemical Physics* **2007**, *9*, 2959–2967.

[173] McLain, S. E.; Soper, A. K.; Terry, A. E.; Watts, A. *Journal of Physical Chemistry B* **2007**, *111*, 4568–4580.

[174] Meersman, F.; Bowron, D.; Soper, A. K.; Koch, M. H. *Biophysical Journal* **2009**, *97*, 2559–2566.

[175] Soper, A. K.; Castner, E. W.; Luzar, A. *Biophysical Chemistry* **2003**, *105*, 649–666.

[176] Soper, A. K.; Ricci, M. A.; Bruni, F.; Rhys, N. H.; McLain, S. E. *Journal of Physical Chemistry B* **2018**, *122*, 7365–7374.

[177] Laurent, H.; Baker, D. L.; Soper, A. K.; Ries, M. E.; Dougan, L. *Journal of Physical Chemistry B* **2020**, *124*, 10983–10993.

[178] Fedotova, M. V.; Kruchinin, S. E. *Journal of Molecular Liquids* **2017**, *244*, 489–498.

[179] Long Range Structure and Zwitterion-Ion Interactions in Osmolyte Solutions - ISIS Data Catalogue. `https://doi.org/10.5286/ISIS.E.RB2220174-1`.

[180] Specific ion effects enhance local structure in zwitterionic osmolyte solutions (data) - Oxford University Research Archive. `https://doi.org/10.5287/ora-deg26axdb`.

[181] Svergun, D. I.; Koch, M. H. J.; Timmins, P. A.; May, R. P. *Small Angle X-Ray and Neutron Scattering from Solutions of Biological Macromolecules*; Oxford University

Press, 2013; pp 13–26.

[182] Youngs, T. G. A. Isotopic Substitution Techniques in Disordered Materials Experiments. 2018.

[183] Finney, J. L.; Soper, A. K. *Chemical Society Reviews* **1994**, *23*, 1–10.

[184] Wu, Y.; Tepper, H. L.; Voth, G. A. *Journal of Chemical Physics* **2006**, *124*, 24503.

[185] Jorgensen, W. L.; Tirado-Rives, J. *Proceedings of the National Academy of Sciences of the United States of America* **2005**, *102*, 6665–6670.

[186] Dodda, L. S.; Vilseck, J. Z.; Tirado-Rives, J.; Jorgensen, W. L. *Journal of Physical Chemistry B* **2017**, *121*, 3864–3870.

[187] Dodda, L. S.; Vaca, I. C. D.; Tirado-Rives, J.; Jorgensen, W. L. *Nucleic Acids Research* **2017**, *45*, W331–W336.

[188] Soper, A. K. *Molecular Physics* **2009**, *107*, 1667–1684.

[189] Soper, A. K. *ISRN Physical Chemistry* **2013**, *2013*, 67.

[190] Soper, A. K. *Chemical Physics* **2000**, *258*, 121–137.

[191] Okhulkov, A. V.; Demianets, Y. N.; Gorbaty, Y. E. *The Journal of Chemical Physics* **1994**, *100*, 1578–1588.

[192] Gioacchino, M. D.; Bruni, F.; Ricci, M. A. *Journal of Molecular Liquids* **2020**, *318*, 114253.

[193] Laurent, H.; Youngs, T. G. A.; Headen, T. F.; Soper, A. K.; Dougan, L. *Communications Chemistry* **2022**, *5*, 1–10.

[194] Bowron, D. T.; Moreno, S. D. *The Journal of Chemical Physics* **2002**, *117*, 3753–3762.

[195] Sironi, M.; Fornilia, A.; Fornili, S. L. *Physical Chemistry Chemical Physics* **2001**, *3*, 1081–1085.

[196] Meersman, F.; Bowron, D.; Soper, A. K.; Koch, M. H. *Physical Chemistry Chemical Physics* **2011**, *13*, 13765–13771.

[197] Civera, M.; Fornili, A.; Sironi, M.; Fornili, S. L. *Chemical Physics Letters* **2003**, *367*, 238–244.

[198] Mason, P. E.; Ansell, S.; Neilson, G. W.; Rempe, S. B. *Journal of Physical Chemistry A* **2015**, *119*, 2003–2009.

[199] Miao, S.; Jiang, H. J.; Imberti, S.; Atkin, R.; Warr, G. *The Journal of Chemical Physics* **2021**, *154*, 214504.

[200] Jan, N. *Physica A: Statistical Mechanics and its Applications* **1999**, *266*, 72–75.

[201] Lorenz, C. D.; Ziff, R. M. *Physical Review E* **1998**, *57*, 230.

[202] Guinn, E. J.; Pegram, L. M.; Capp, M. W.; Pollock, M. N.; Record, M. T. *Proceedings of the National Academy of Sciences of the United States of America* **2011**, *108*, 16932–16937.

[203] Lin, T. Y.; Timasheff, S. N. *Biochemistry* **2002**, *33*, 12695–12701.

[204] Yancey, P. H. *Paracelsus Proceedings of Experimental Medicine* **2023**, *2*, 67–91.

[205] Godara, G.; Smith, C.; Bosse, J.; Zeidel, M.; Mathai, J. *American Journal of Physiology - Regulatory Integrative and Comparative Physiology* **2009**, *296*, 1268–1273.

[206] Sebbane, F.; Bury-Moné, S.; Cailliau, K.; Browaeys-Poly, E.; Reuse, H. D.; Simonet, M. *Molecular Microbiology* **2002**, *45*, 1165–1174.

[207] Levin, E. J.; Cao, Y.; Enkavi, G.; Quick, M.; Pan, Y.; Tajkhorshid, E.; Zhou, M. *Proceedings of the National Academy of Sciences of the United States of America* **2012**, *109*, 11194–11199.

[208] Gardner, J. V.; Armstrong, A. A.; Calder, B. R.; Beaudoin, J. *Marine Geodesy* **2014**, *37*, 1–13.

[209] Laxson, C. J.; Condon, N. E.; Drazen, J. C.; Yancey, P. H. *Physiological and Biochemical Zoology* **2011**, *84*, 494–505.

[210] Palmer, H. R.; Bedford, J. J.; Leader, J. P.; Smith, R. A. *Journal of Biological Chemistry* **2000**, *275*, 27708–27711.

[211] *S. pombe* Pop2p Protein Structure. `https://commons.wikimedia.org/wiki/File:Spombe_Pop2p_protein_structure_rainbow.png`.

[212] Zetterholm, S. G.; Verville, G. A.; Boutwell, L.; Boland, C.; Prather, J. C.; Bethea, J.; Cauley, J.; Warren, K. E.; Smith, S. A.; Magers, D. H.; Hammer, N. I. *Journal of Physical Chemistry B* **2018**, *122*, 8805–8811.

[213] Ohto, T.; Hunger, J.; Backus, E. H.; Mizukami, W.; Bonn, M.; Nagata, Y. *Physical Chemistry Chemical Physics* **2017**, *19*, 6909–6920.

[214] Ganguly, P.; Boserman, P.; Vegt, N. F. V. D.; Shea, J. E. *Journal of the American*

Chemical Society **2018**, *140*, 483–492.

[215] Ganguly, P.; Polák, J.; Vegt, N. F. V. D.; Heyda, J.; Shea, J. E. *Journal of Physical Chemistry B* **2020**, *124*, 6181–6197.

[216] Paul, S.; Patey, G. N. *Journal of the American Chemical Society* **2007**, *129*, 4476–4482.

[217] Sukenik, S.; Sapir, L.; Gilman-Politi, R.; Harries, D. *Faraday Discussions* **2013**, *160*, 225–237.

[218] Hua, L.; Zhou, R.; C, D. T.; Berne, B. J. *Proceedings of the National Academy of Sciences of the United States of America* **2008**, *105*, 16928–16933.

[219] Cho, S. S.; Reddy, G.; Straub, J. E.; Thirumalai, D. *Journal of Physical Chemistry B* **2011**, *115*, 13401–13407.

[220] Rösgen, J.; Jackson-Atogi, R. *Journal of the American Chemical Society* **2012**, *134*, 3590–3597.

[221] Kadtsyn, E. D.; Anikeenko, A. V.; Medvedev, N. N. *Journal of Structural Chemistry* **2018**, *59*, 347–354.

[222] Jackson-Atogi, R.; Sinha, P. K.; Rösgen, J. *Biophysical Journal* **2013**, *105*, 2166–2174.

[223] Candotti, M.; Esteban-Martín, S.; Salvatella, X.; Orozco, M. *Proceedings of the National Academy of Sciences of the United States of America* **2013**, *110*, 5933–5938.

[224] Xie, W. J.; Cha, S.; Ohto, T.; Mizukami, W.; Mao, Y.; Wagner, M.; Bonn, M.; Hunger, J.; Nagata, Y. *Chem* **2018**, *4*, 2615–2627.

[225] Nasralla, M.; Laurent, H.; Baker, D. L.; Ries, M. E.; Dougan, L. *Physical Chemistry Chemical Physics* **2022**, *24*, 21216–21222.

[226] Julius, K.; Weine, J.; Berghaus, M.; König, N.; Gao, M.; Latarius, J.; Paulus, M.; Schroer, M. A.; Tolan, M.; Winter, R. *Physical Review Letters* **2018**, *121*, 038101.

[227] Cohn, E. J. *Proteins, amino acids and peptides as ions and dipolar ions*; Reinhold Publishing Corporation, 1943.

[228] Sasaki, Y.; Horikawa, Y.; Tokushima, T.; Okada, K.; Oura, M.; Aida, M. *Physical Chemistry Chemical Physics* **2016**, *18*, 27648–27653.

[229] Chen, X.; Sagle, L. B.; Cremer, P. S. *Journal of the American Chemical Society* **2007**, *129*, 15104–15105.

[230] Stein, W. D. *Transport and Diffusion Across Cell Membranes*, 1st ed.; Academic Press, 1986.

[231] National Center for Biotechnology Information. PubChem Compound Summary for CID 1176, Urea. `https://pubchem.ncbi.nlm.nih.gov/compound/Urea`.

[232] Nasralla, M.; Laurent, H.; Alderman, O. L.; Headen, T. F.; Dougan, L. *Proceedings of the National Academy of Sciences of the United States of America* **2024**, *121*, e2317825121.

[233] Yancey, P. H.; Burg, M. B. *American Journal of Physiology-Regulatory, Integrative and Comparative Physiology* **1990**, *258*, R198–R204.

[234] Yancey, P. H. *Integrative and Comparative Biology* **2001**, *41*, 699–709.

[235] Nandi, P. K.; Bera, A.; Sizaret, P. Y. *Journal of Molecular Biology* **2006**, *362*, 810–820.

[236] Bhat, M. Y.; Singh, L. R.; Dar, T. A. *Scientific Reports 2017 7:1* **2017**, *7*, 1–8.

[237] Bhat, M. Y.; Mir, I. A.; Hussain, M. U.; Singh, L. R.; Dar, T. A. *Journal of Biomolecular Structure and Dynamics* **2023**, *41*, 3659–3666.

[238] Rock, K. L.; Goldberg, A. L. *Annual Review of Immunology* **1999**, *17*, 739–779.

[239] Radzicka, A.; Wolfenden, R. *Journal of the American Chemical Society* **1996**, *118*, 6105–6109.

[240] Ciechanover, A.; Schwartz, A. L. *Proceedings of the National Academy of Sciences of the United States of America* **1998**, *95*, 2727–2730.

[241] Prajapati, S. C.; Chauhan, S. S. *The FEBS Journal* **2011**, *278*, 3256–3276.

[242] Morris, O. M.; Torpey, J. H.; Isaacson, R. L. *Open Biology* **2021**, *11*.

[243] Lubkowitz, M. *Molecular Plant* **2011**, *4*, 407–415.

[244] Lotthammer, J. M.; Ginell, G. M.; Griffith, D.; Emenecker, R. J.; Holehouse, A. S. *Nature Methods* **2024**, *21*, 465–476.

[245] Drake, J. A.; Pettitt, B. M. *Biophysical Journal* **2018**, *114*, 2799–2810.

[246] Drake, J. A.; Pettitt, B. M. *Journal of Physical Chemistry B* **2020**, *124*, 4379–4390.

[247] Wright, P. E.; Dyson, H. J. *Journal of Molecular Biology* **1999**, *293*, 321–331.

[248] Dunker, A. K.; Obradovic, Z. *Nature Biotechnology* **2001**, *19*, 805–806.

[249] Barnhart, M. M.; Chapman, M. R. *Annual Review of Microbiology* **2006**, *60*, 131–147.

[250] Sek, S.; Moszynski, R.; Sepiol, A.; Misicka, A.; Bilewicz, R. *Journal of Electroanalytical Chemistry* **2003**, *550-551*, 359–364.

[251] Baghbanzadeh, M.; Bowers, C. M.; Rappoport, D.; Zaba, T.; Gonidec, M.; Al-Sayah, M. H.; Cyganik, P.; Aspuru-Guzik, A.; Whitesides, G. M. *Angewandte Chemie International Edition* **2015**, *54*, 14743–14747.

[252] Bovin, N. V.; Tuzikov, A. B.; Chinarev, A. A. *Nanotechnologies in Russia* **2008**, *3*, 291–302.

[253] Gus'kova, O. A.; Khalatur, P. G.; Khokhlov, A. R.; Chinarev, A. A.; Tsygankova, S. V.; Bovin, N. V. *Russian Journal of Bioorganic Chemistry* **2010**, *36*, 574–580.

[254] Tsygankova, S. V. et al. *Journal of Biomaterials and Nanobiotechnology* **2011**, *2*, 91–97.

[255] Auton, M.; Bolen, D. W. *Biochemistry* **2004**, *43*, 1329–1342.

[256] Karandur, D.; Wong, K. Y.; Pettitt, B. M. *Journal of Physical Chemistry B* **2014**, *118*, 9565–9572.

[257] Sarma, R.; Wong, K. Y.; Lynch, G. C.; Pettitt, B. M. *Journal of Physical Chemistry B* **2018**, *122*, 3528–3539.

[258] Drake, J. A.; Harris, R. C.; Pettitt, B. M. *Biophysical Journal* **2016**, *111*, 756–767.

[259] Asthagiri, D.; Karandur, D.; Tomar, D. S.; Pettitt, B. M. *Journal of Physical Chemistry B* **2017**, *121*, 8078–8084.

[260] Harris, R. C.; Pettitt, B. M. *Journal of Physics: Condensed Matter* **2016**, *28*, 083003.

[261] Karandur, D.; Harris, R. C.; Pettitt, B. M. *Protein Science* **2016**, *25*, 103–110.

[262] Karandur, D.; Pettitt, B. M. *Condensed matter physics* **2016**, *19*, 23802.

[263] Bartlett, G. J.; Choudhary, A.; Raines, R. T.; Woolfson, D. N. *Nature Chemical Biology* **2010**, *6*, 615–620.

[264] Das, T.; Eliezer, D. *Biochimica et Biophysica Acta (BBA) - Proteins and Proteomics*

2019, *1867*, 879–889.

[265] Wyman, J.; McMeekin, T. L. *Journal of the American Chemical Society* **1933**, *55*, 908–914.

[266] Pichon-Pesme, V.; Lecomte, C. *Acta Crystallographica* **1998**, *54*, 485–493.